Advances in Industrial Control

Bram de Jager
Thijs van Keulen
John Kessels

Optimal Control of Hybrid Vehicles

AIC

Springer

Advances in Industrial Control

For further volumes:
www.springer.com/series/1412

Bram de Jager • Thijs van Keulen • John Kessels

Optimal Control of Hybrid Vehicles

Springer

Bram de Jager
Department of Mechanical Engineering
Eindhoven University of Technology
Eindhoven, The Netherlands

John Kessels
Department of Electrical Engineering
Eindhoven University of Technology
Eindhoven, The Netherlands

Thijs van Keulen
DAF Trucks N.V.
Eindhoven, The Netherlands

ISSN 1430-9491
ISSN 2193-1577 (electronic)
Advances in Industrial Control
ISBN 978-1-4471-5075-6
ISBN 978-1-4471-5076-3 (eBook)
DOI 10.1007/978-1-4471-5076-3
Springer London Heidelberg New York Dordrecht

Library of Congress Control Number: 2013936944

Printed on acid-free paper

Springer is part of Springer Science+Business Media (www.springer.com)

Series Editors' Foreword

The series *Advances in Industrial Control* aims to report and encourage technology transfer in control engineering. The rapid development of control technology has an impact on all areas of the control discipline. New theory, new controllers, actuators, sensors, new industrial processes, computer methods, new applications, new philosophies, new challenges. Much of this development work resides in industrial reports, feasibility study papers and the reports of advanced collaborative projects. The series offers an opportunity for researchers to present an extended exposition of such new work in all aspects of industrial control for wider and rapid dissemination.

Identifying the drivers of technological change in today's automotive industry and the related fields of motorized transportation systems is not a simple task. One set of factors is simply involved with obtaining commercial advantage; vehicle manufacturers must innovate and provide new features in their products to ensure their vehicles sell, thereby preserving, and preferably increasing their market share. Quite a different set of factors is regulatory concerning such issues as reduced vehicle emissions, enhanced energy use and better driver-passenger safety features. As an example of regulatory pressures, an article on the "Carbon Car" in *IEEE Spectrum* (January 2013 issue, p. 28) reported: "In the United States, President Obama has called for manufacturers of cars and trucks to double their fuel economy by 2025, to a lofty 54.5 miles per gallon (4.3 liters per 100 kilometers). The European Union targets a 40 percent reduction in automotive CO_2 emissions by 2018; the target of 130 grams of CO_2 per kilometer driven equates to 5.6 L/100 km or 42 mpg." These commercial and regulatory motivating pressures are intertwined with what can be achieved by the ingenuity of today's engineers, and the potential advances from using new materials, digital electronics, and new mechanical and electrical technology.

For a number of years now the application of control in the field of automobile design, construction, and operation has been growing ever more confident with new sophisticated and complex control proposals. These developments have been regularly reported at key control conferences through invited sessions, specialist workshops and regular papers. An interesting feature of many automotive control sessions at control conferences has been the valuable and significant presence of

participants from the automotive industry. Consequently control techniques have made real contributions to automotive engine and power-train control, to emission reduction and better fuel utilization, to driver-assistance systems, to driver and passenger comfort and to the management of road transportation systems and vehicle behavior where future developments may even involve increasing vehicular autonomy.

The *Advances in Industrial Control* monograph series has long sought entries reporting new control developments in the automotive and transportation field, but it has taken some time for the monograph literature in this field to develop. Contributions are beginning to appear in the series, for example:

- *Dry Clutch Control for Automotive Applications* by Pietro J. Dolcini, Carlos Canudas de Wit and Hubert Béchart (ISBN 978-1-84996-067-0, 2010);
- *Active Braking Control Systems Design for Vehicles* by Sergio M. Savaresi and Mara Tanelli (ISBN 978-1-84996-349-7, 2010); and
- *Nonlinear Control of Vehicles and Robots* by Béla Lantos and Lőrinc Márton (ISBN 978-1-84996-121-9, 2011);

and in the related field of transportation management:

- *Feedback Control Theory for Dynamic Traffic Assignment* by Pushkin Kachroo and Kaan Özbay (ISBN 978-1-85233-059-0, 1999); and
- *Hybrid Predictive Control for Dynamic Transport Problems* by Alfredo Núñez, Doris A. Sáez and Cristián E. Cortés (ISBN 978-1-4471-4350-5, 2013).

To this group of monographs we can now add a long-sought-after title on hybrid vehicles. The monograph is entitled *Optimal Control of Hybrid Vehicles* and the authors are Bram de Jager, Thijs van Keulen and John Kessels. A very useful introductory chapter that discusses the fuel-economy motivational origins of hybrid vehicles opens the monograph. In this opening chapter a hybrid vehicle is defined as a vehicle constructed with energy recovery options and the monograph itself deals with the hybrid electric drivetrain that combines an internal combustion engine with energy recovery using an electrical machine and battery storage. Chapter 2 presents the modeling framework and Chap. 3 is a short chapter that concisely defines the increasingly constrained performance optimization problems to be solved. The final four chapters of the monograph deal with optimal control analytical solution procedures, numerical solutions, real-time implementation strategies and finally some experimental case-study investigations, respectively. With its focus on the optimized energy management of hybrid electric power-trains, this monograph will be of considerable interest to industrial practitioners in the automotive field and to academics and postgraduate researchers working in control, mechanical, and automotive engineering.

Industrial Control Centre
Glasgow, Scotland, UK

M.J. Grimble
M.A. Johnson

Preface

This book presents recent results in the area of control of hybrid vehicles, with an emphasis on energy management for hybrid electric vehicles. The scope of the book covers both light-duty vehicles as well as heavy-duty ones, but the optimization of gear-shifting, vehicle velocity, or route traveled, although they contribute to energy management in a broader sense, are outside the scope.

The book's main audience consists of persons that are interested in techniques that deliver the best fuel economy, the lowest emissions, or smoothest drivability, taking advantage of advanced control freedom provided by hybridization. Those persons may come from industry, being employed in specifying, developing, or calibrating energy management systems, or that foresee they will be more intensively involved in these areas. They could also come from academia, where they carry out projects aiming to improve the performance of hybrid systems or to design better or more cost effective hardware solutions. Furthermore, the book addresses students who envision a career in control in the automotive industry, be it research, development, production, or support. Lastly, it addresses persons that are involved in emission legislation or in designing test procedures for vehicle homologation, so they are well informed about the intricacies that hybrid systems add to conventional vehicles. The authors have tried to make this book easily accessible to all those people with different backgrounds. Probably the presentation is too rigorous for some persons, and too lax for others, so we would very much appreciate reader comments. A part of the text has been used for teaching purposes, and the comments received from our students have been beneficial.

The increased market acceptance of hybrid vehicles, which are a key ingredient in meeting environmental targets for fuel economy and/or CO_2 emissions while still allowing the usual freedom to travel, has led to accelerated research and development paths to make the necessary technology mature for series production in large numbers. The knowledge gained in a specific area, namely optimal control of the drivetrain focusing on energy management, is shared with this book.

Persons reading this book can expect to receive answers to questions like: How can hybrid vehicles provide any fuel economy or emissions benefits? What is necessary to realize those benefits, what is useful, and what could be omitted? Is it

possible to prove that those benefits are realized with maximum performance? Is the energy management system intricate, or can it be simplified, achieving practically the same benefits? Can hybrid vehicles be made more cost effective?

The text does not provide a blue print for an automated design procedure for energy management systems, although the accompanying software tools allow the reader to reproduce the results presented in this book. Those tools are open and adaptable, so allow the reader to plug in his/her own numbers or characteristics and generate results matching the conditions he/she is designing for.

The book is an excerpt from research activities carried out at Eindhoven University of Technology during the last decade, with the help of several industrial partners and research institutes. Especial beneficial in shaping our thoughts that have been codified in this book have been Michiel Koot, Paul van den Bosch, Maarten Steinbuch and Maurice Heemels. The support and valuable feedback from our research partners is highly appreciated: Daniel Kok, Engbert Spijker, Edo Aneke (Ford Research Center Aachen), Loek van Seeters, Jack Martens (DAF Trucks N.V. Eindhoven) and Olaf op den Camp (TNO Helmond). For the experimental case studies the help of Will Hendrix, Ruud van den Bogaert, Toon van Gils, Erwin Meinders and Dominique van Mullem was invaluable. Barbara Cornelissen-Milner was of great help in fine-tuning the text.

Eindhoven, The Netherlands

Bram de Jager
Thijs van Keulen
John Kessels

Contents

Nomenclature

Acronyms

BL	Baseline
BVP	Boundary value problem
CAN	Controller-area network
DP	Dynamic programming
EAS	Engine aftertreatment system
ECM	Engine control module
ECMS	Equivalent consumption minimization strategy
ECU	Electronic control unit
EMS	Energy management strategy
FE	Fuel economy
FTP	Federal test procedure
HD	Heavy duty
HEV	Hybrid electric vehicle
HJB	Hamilton–Jacobi–Bellman
ICE	Internal combustion engine
IVP	Initial value problem
JC	Japanese cycle
LP	Linear programming
MPC	Model predictive control
MTn	Manual transmission with n gears
NEDC	New European driving cycle
PDM	Power distribution management
PID	Proportional integral derivative
PMP	Pontryagin's Maximum/minimum Principle
PSM	Power supply management
QP	Quadratic programming
SLI	Start, light, ignition
UDDS	Urban dynamometer driving schedule
VRLA	Valve-regulated lead-acid

WHSC	World harmonised stationary cycle
WHTC	World harmonised transient cycle

Roman Uppercase

Symbol	Description	Unit
C_d	Dynamo road load control	–
C_v	Velocity controller	–
E	Energy	J
E_c	Theoretical battery capacity	J
E_d	Dynamo energy consumption	J
E_{eq}	Equivalent fuel energy	J
E_f	Fuel energy	J
E_l	Electric load energy	J
E_s	Energy in storage device	J
E_s^0	Initial energy in storage device	J
E_s^f	Final energy in storage device	J
E_{s_r}	Reference energy in storage device	J
F	Force	N
	Argument cost integral	–
F_a	Inertial force	N
F_w	Road load force	N
H	Hamiltonian	–
	Quadratic weight in QP problem	–
I	Current	A
I_d	Dynamo control current	A
I_s	Battery storage current	A
J	Cost function	–
K	Feedback gain	–
K_E	Kinetic energy recovery feedback gain	–
K_h	Potential energy recovery feedback gain	–
K_i	Integral gain	–
K_p	Proportional gain	–
L	Lagrangian	–
	Cost-to-arrive vector	J
LL	Cost-to-arrive matrix	J
$\mathscr{P}_i$	Optimization problem $i = 0, \ldots, 3$	–
$\mathscr{P}_x$	Optimization problem $x =$ BVP, IVP, EUL, NL	–
P	Power	W
P_b	Battery electrical power	W
P_e	Electric machine electrical power	W

P_f	Fuel power	W
$P_{f,i}$	Fuel power during idle	W
$P_{f,p}$	Fuel power during traction	W
P_k	Service brake power	W
P_l	Electrical load power	W
P_m	Electric machine mechanical power	W
P_{m_r}	Electric machine power request	W
P_p	Prime mover mechanical power	W
P_r	Power request	W
P_s	Storage power	W
P_{s_ch}	Storage power during charging	W
P_{s_dis}	Storage power during discharging	W
P_w	Power at the wheels	W
Q_s	Storage charge	C
R	Resistance	Ohm
	Cost-to-arrive matrix	–
S	Clutch position	–
SOC	State-of-charge	–
SOE	State-of-energy	–
SOE_r	Reference state-of-energy	–
T	Torque	N m
T_c	Torque compensation drum dynamics	N m
T_d	Torque at dynamo drum circumference	N m
T_m	Electric machine torque	N m
T_{m_r}	Electric machine torque request	N m
T_p	Prime mover torque	N m
T_{p_r}	Prime mover torque request	N m
T_r	Torque request	N m
T_{set}	Dynamo torque setpoint	N m
$\mathscr{U}$	Set of admissible controls	–
U	Voltage	V
	Cost vector	–
U_0	Voltage of a depleted battery	V
U_R	Over-potential voltage	V
U_{oc}	Open-circuit voltage	V
U_t	Terminal voltage	V

Roman Lowercase

Symbol	Description	Unit
c_0	Rolling resistance	N
c_1	Velocity dependent drivetrain resistance	$\mathrm{N\,s\,m^{-1}}$
c_2	Aerodynamic resistance	$\mathrm{N\,s^2\,m^{-2}}$
f	General function	–
g	Constraint function	–
g_a	Acceleration due to gravity	$\mathrm{m\,s^{-2}}$
h	Elevation	m
	Lower heating value	J/kg
	Constraint function	–
	Linear term in QP problem	–
i	Segment number	–
	Omit segment	–
j	Number	–
k	Discrete time index	–
m	Mass	kg
	Vehicle mass	kg
	Number of energy level	–
m_e	Effective vehicle mass	kg
n	Number of data points	–
p	Multiplier function vector	–
p^0	Multiplier initial guess	–
r	Radius	m
	Extraneous input	–
r_d	Dynamo drum radius	m
r_g	Gear ratio	–
r_h	Hybridization ratio	–
s	Distance	m
s_{trip}	Trip distance	m
t	Time	s
u	Control variable	–
v	Velocity	$\mathrm{m\,s^{-1}}$
v_d	Circumferential drum velocity	$\mathrm{m\,s^{-1}}$
w	Weight factor	–
x	State variable	–

Greek

Symbol	Description	Unit
α	Road slope	rad
β	Battery characteristic	–
β_1	Battery characteristic	–
β_2	Battery characteristic	1/W
γ	Conversion characteristic	–
$\gamma_{m,0}$	Electric machine conversion characteristic	–
$\gamma_{m,1}$	Electric machine conversion characteristic	–
$\gamma_{m,2}$	Electric machine conversion characteristic	–
$\gamma_{p,0}$	Prime mover conversion characteristic	–
$\gamma_{p,1}$	Prime mover conversion characteristic	–
ϵ	Allowed error of end point constraint	–
ζ	Factor in optimal solution	–
ϑ	Gas pedal position	%
λ	Lagrange multiplier	–
σ	Piecewise constant	–
τ	Time	s
ϕ	Incremental voltage	V/J
φ_i	Derived model parameters $i = 0, \ldots, 2$	–
χ	Factor in optimal solution	–
ψ	End state error	J
ω	Rotational velocity	$\mathrm{rad\,s^{-1}}$
ω_m	Rotational velocity of the electric machine	$\mathrm{rad\,s^{-1}}$
ω_p	Rotational velocity of the prime mover	$\mathrm{rad\,s^{-1}}$

Super/subscripts

Symbol	Description
$+$	Positive, right going
$-$	Negative, left going
$\star$	Optimum
$\hat{\cdot}$	Estimate
0	Initial value
f	Final value

Symbols and Operations

Symbol	Description	Example
$\underline{a}$	Minimum value of set a	$\underline{a} = \min(a)$
$\overline{a}$	Maximum value of set a	$\overline{a} = \max(a)$
$\lvert a \rvert$	Complex modulus (magnitude)	$\sqrt{\Re a^2 + \Im a^2}$
$\bar{a}$	Averaged value	$\frac{1}{N}\sum_1^N a_k$
$\frac{\partial a(x,t)}{\partial x}$	Partial derivative	$\frac{\partial (bx+ct)}{\partial x} = b$
$\dot{a}$	Time derivative	$\frac{\partial (bx+ct)}{\partial t} = c + b\dot{x}$

Chapter 1
Introduction

1.1 Objectives and Motivation

This section presents the motivation for the use of hybrid systems and a road map to achieve the predicted benefits of those systems.

1.1.1 Trends in Vehicle Fuel Economy

Mobility forms one of mankind's basic needs. Ever since people started specializing in one profession, they have relied on the products and knowledge of others, requiring a form of mobility. Transport cost, of people and goods, in time and effort, is, therefore, closely related to economic growth. The search for faster and less costly ways of transport has continued throughout history.

A milestone formed the discovery of petroleum oil, as a cheap and widely available fuel, and the invention of the internal combustion engine propelled vehicle (Benz 1886), as a light and cost effective transporter. Initially, the gasoline powered engine had to compete with steam and electric powered engines, and with hybrid vehicles. However, an on-demand travel with flexibility, average velocity, and range that soon surpassed other means of transportation became possible. Having also a cost advantage, eventually, combustion engines dominated the other technologies, which were reborn only recently (Anderson and Anderson 2010). The enhanced mobility was one of the motors of the enormous increase in prosperity over the last century.

Although petroleum oil is cheap to produce and widely available, it is clear that the fossil fuel reserves are not inexhaustible. Besides, the combustion of fossil fuels results in the emission of carbon dioxide (CO_2), which is a main contributor to global warming. Also, the air quality in large urban areas is becoming a serious issue. To sustain or increase mobility in western countries, and to offer to developing countries a prospect of similar levels of mobility, while oil reserves are dwindling and emission legislation becomes more stringent, research for other energy sources

B. de Jager et al., *Optimal Control of Hybrid Vehicles*, Advances in Industrial Control,
DOI 10.1007/978-1-4471-5076-3_1,

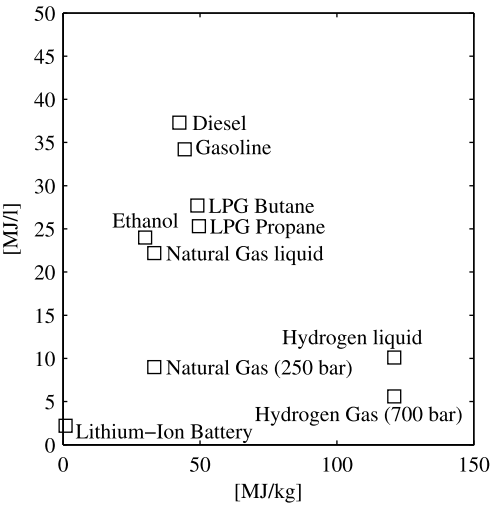

Fig. 1.1 Energy volume density versus lower heating value of several energy carriers

than petroleum oil and cleaner and less wasteful means of fuel use in road transport is necessary (IEA 2009).

Energy carriers other than petroleum oil are, e.g., hydrogen gas, natural gas, bio fuels, and electro-chemical storage in batteries. Figure 1.1 depicts the energy density characteristics of different energy carriers. It can be seen that petroleum related fuels, diesel, gasoline, etc., have excellent energy-volume properties. The high energy density property of petroleum oil related fuels lead to the expectation (IEA 2007) that internal combustion engines will have a dominant role in the next decades. This holds especially for heavy-duty vehicles that require a large range in combination with a low mass. For a detailed comparison of the energy carriers see, e.g., Edwards et al. (2006).

Representative data for *fuel economy*, i.e., the amount of fuel consumed to travel a fixed distance, or, alternatively, the distance traveled for a fixed amount of fuel, of *heavy-duty* vehicles, like trucks or lorries, coming from tests carried out during a series of years are presented in Fig. 1.2. From these data, it appears that there was a steady improvement in fuel economy until the year 1986, and from then on, so for a period of at least 25 years, fuel economy was practically unchanged. One of the explanations is the emphasis on reducing emissions of NO_x and particulate matter in diesel engines, which is not always compatible with reducing CO_2 emissions, which relate strongly to fuel economy.

Similar data are available for *light-duty* vehicles, like cars and vans. An example is shown in Fig. 1.3. These data show that, at least in some regions, type-approval fuel economy improves, but only after regulatory measures.

The graph is based on type-approval data for newly registered light-duty vehicles in Germany. The average age of vehicles in this regional fleet is 8.5 year, the size of the vehicle fleet is growing, the *in-use* (also called real driving or on-road) fuel economy is 20 % (IEA 2009; Mock et al. 2012) to 25 % (Sierra 2011) worse than the type-approval one with an increasing trend (Mock et al. 2012), see Fig. 1.4

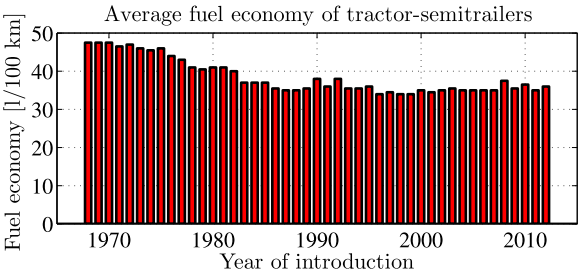

Fig. 1.2 Measured fuel economy of heavy-duty vehicles with a mass of 38–40 $\times$ 10^3 [kg] during a series of years. Data partly derived from ACEA (2010) which cites "Lastauto omnibus test reports 1967–2009." The decrease in the period 1970–1980 was due to the introduction of turbocharging and in the period 1980–1986 it was due to the introduction of inter-cooling. The peaks in 1992 and 2008 coincide with the introduction of more stringent emission legislation

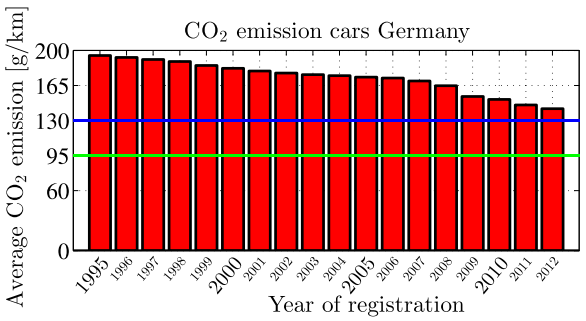

Fig. 1.3 Fleet average type-approval CO_2 emissions of newly registered light-duty vehicles during a series of years in Germany. The 130 level (*blue*) is the target for 2015 (was initially 2012) and the 95 level (*green*) is the target for 2020 for cars, it is 147 for vans. Because full electric and hybrid vehicle registrations are smaller than 1 % of the total number of registrations in 2012, average CO_2 emission is a reliable predictor of average *type-approval* fuel economy

for some examples. The graph in Fig. 1.3 thus gives a rather optimistic view of the trend in yearly CO_2 emissions. The real trend is a much delayed version of the graph, multiplied by another, increasing, function. Therefore, CO_2 emissions are still growing. Further improving the overall fuel economy of petroleum oil powered vehicles is thus a relevant topic. This was recognized in the past, but recommendations for transport policies to bring these improvements have met with a slow rate of implementation (IEA 2010).

Apart from improvements in in-use fuel economy, other ways to reduce fuel consumption and emission of green house gases are reducing distance traveled, e.g., combining trips or pooling cars, avoiding empty running, which happens on 20–38 % of heavy-duty vehicle trips, e.g., with better fleet management and logistics thereby improving vehicle utilization, using better (shorter or smoother) routes, e.g., using a route planner, or shifting transport modalities to more effective modes, e.g.,

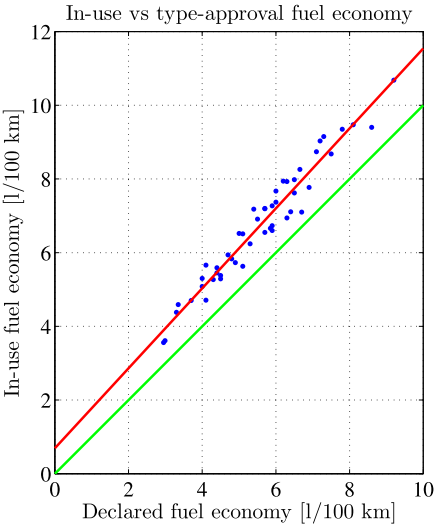

Fig. 1.4 In-use fuel economy versus declared type-approval fuel economy for various recent car models (*blue dots*). The *red line* is a linear regression, the *green* one is the diagonal. All vehicles have a higher in-use than type-approval fuel economy, without any exception. Data were obtained using the methodology of Mock et al. (2012). The main causes for the differences in fuel economy are the use of auxiliary equipment (mobile air conditioning, lighting, entertainment, battery charging, etc.), the prescribed drive cycle (the type-approval cycles are not representative of on-road driving, e.g., the cycles are on level ground and have too moderate decelerations), the test conditions (temperatures during the test are not tightly controlled, the tires used are not the winter tires that are obligatory during part of the year in some regions), and regulatory loop holes (use of weight classes instead of actual weight, freedom in drive cycle velocities, flexibilities in establishing road load parameters, use of prototypes instead of series production vehicles, etc.)

to ship or train, from which fuel economy improvements can be expected. These ways are all about demand containment and demand profiling. Furthermore, the use of energy carriers that have a lower emission of green house gases per unit energy delivered, e.g., bio fuels (IEA 2011a), or a shift to other energy carriers than fuels, e.g., all electric vehicles when the energy mix of the electric grid is twisted to use more renewable sources (IEA 2011b), will reduce production of those gases.

There are several ways to achieve the goal of improved in-use fuel economy. One option is to improve driver behavior, e.g., by teaching so-called eco-driving habits because the driver has a considerable influence on velocity, acceleration, and deceleration, and thus power, levels. A second option is to lower the power needed to follow a certain speed profile, e.g., by using tires with a lower rolling resistance, by taking aerodynamic measures, and by lowering the vehicle inertia. A third option for improving fuel economy is to decrease the losses in the engine and drivetrain, e.g., by design improvements, by downsizing engines, or by better choices for the working points, i.e., by improved shifting strategies. A fourth option is to lower the power consumption of auxiliaries, e.g., by using better air conditioning equipment. A fifth option is to equip the conventional vehicle with the possibility to recover

energy during braking or driving downhill by adding a motor/generator. Vehicles with energy recovery options are commonly referred to as *hybrid* vehicles. A sixth option is to operate the vehicle in a better way than the average human driver would do, e.g., by controlling the hybrid drivetrain components automatically. These six options for improving in-use fuel economy are further detailed in Sect. 1.1.2. Other options are also possible, such as reducing the gap between in-use and type-approval fuel economy to avoid manufacturers aiming at the wrong objective, but these are mainly political, regulatory, or economic, not technological.

1.1.2 Road Map Towards Energy Sustainable Mobility

Fuel economy is determined according to type-approval regulations by testing on a prescribed route, so for a fixed speed profile. For heavy-duty vehicles often only an engine test is mandatory, due to the large number of combinations of vehicles and engines. For each vehicle type, the drive cycle results in a certain power profile that needs to be delivered at the wheels. The fuel power needed to provide the power at the wheels is much higher, typically by a factor of 4, the so-called tank-to-wheel factor, due to losses in the powertrain and engine. When losses in the supply chain of fuels are accounted for, we obtain the well-to-wheel factor, which is typically 5 or larger. We first look at factors that reduce the power at the wheels, and then at factors influencing the input power of the power converters for a given wheel power.

1.1.2.1 Power at the Wheels

To get a feeling for the options possible for improving fuel economy and to understand the benefits of hybrid vehicles let us first describe the power required to propel a vehicle using an elementary model:

$$P_w = \underbrace{m_e v \dot{v}}_{(1)} + \underbrace{m v g_a \sin\alpha}_{(2)} + \underbrace{c_0 m v g_a \cos\alpha}_{(3)} + \underbrace{c_2 v^3}_{(4)}, \tag{1.1}$$

where P_w is the power request at the wheels, m_e the effective vehicle inertia, including rotational inertia, m the vehicle mass, v the vehicle velocity, where we consider only positive values and neglect the influence of the wind velocity, $\dot{v}$ the vehicle acceleration, g_a the gravitational constant, α the road angle, c_0 a coefficient for the rolling resistance, and c_2 a coefficient for the aerodynamic losses. Several components that contribute to the required power can be distinguished:

1. inertial power, the power to overcome the inertia of the vehicle, to acquire or release kinetic energy,
2. gravitational power, the power to overcome elevations in a route, to acquire or release potential energy,
3. rolling losses, the power required to overcome the resistance of the tires,
4. aerodynamic losses, the power required to overcome the aerodynamic resistance of the vehicle.

One way to improve fuel economy is to minimize the cumulative required positive power. Negative power contributions cannot be recuperated by a normal drivetrain, except for supplying auxiliaries. Looking at (1.1) one sees that P_w can be reduced by reducing v, $\dot{v}$, m, g_a, α, c_0, and c_2. All those variables and parameters can be changed, except for g_a.

By lowering the maximum speed, by avoiding hard braking, or by following the flow of the other traffic participants to avoid abrupt changes in v, a different velocity profile is created which will reduce P_w. These changes in v could follow from eco-driving techniques or from optimized velocity trajectories, see, e.g., Van Keulen et al. (2010). They could also be the result of driving assistance systems such as predictive or adaptive *cruise control*, see, e.g., Van Keulen et al. (2009), cooperative adaptive cruise control, see, e.g., Naus et al. (2010), or intelligent speed adaptation, see, e.g., Lahrmann et al. (2012), or be the result of intelligent *traffic control*.

Lowering the inertia represented by m_e is possible by reducing the curb weight, by using fewer loads, or by using lighter loads. This requires changes in the design of the vehicle, reduction of vehicle size and engine size, use of light-weight materials, or requires omitting features such as spare tires that do not contribute to the basic functionality of the vehicle. Lighter payloads could also be the result of using lighter packaging techniques for cargo.

The road angle α can only be changed by road work, e.g., by constructing tunnels or using a different road alignment, but when there are route alternatives, one could prefer a route with less change in elevation, even if it is longer, and get a lower fuel consumption for traveling between the same points. The influence of inertia, road angle, and velocity on fuel economy measured in practical situations is discussed in Franzese and Davidson (2011).

A lower rolling resistance c_0 can be achieved by using better tires, by employing better tire condition and tire pressure monitoring, and by axle and wheel alignment maintenance policies. The tires mounted on new series production vehicles have low rolling resistance, being beneficial in fuel economy tests, but those tires have only a small after-market share. It is also possible to use tires of a different design. For instance, the use of wide-based single (or super single) tires for trucks gives a significant improvement in fuel economy, see Al-Qadi and Elseifi (2007), Franzese et al. (2010). This is one of the few measures that can be easily retro-fitted to a vehicle. Better tires are available on the market, are cost effective, but still have a small market penetration (IEA 2012, Key findings 1 and 2).

A better aerodynamic coefficient c_2 requires changes in shape or cross-sectional area of the vehicle. Changes in shape can be obtained by using skirts, spoilers or spats, under-body panels, or by omitting roof appendices. Some of these devices can be retro fitted, are available on the market, are cost effective, but have a small market penetration (IEA 2012, Key findings 1 and 2). Riding in closely spaced platoons also reduces air drag for the following vehicles, see Alam et al. (2010), but this requires a driving assistance system.

All measures above aim to reduce the value of P_w, but are not able to harness the power that is released if $P_w < 0$. Because $\dot{v}$ and α, and thus the inertial power and gravitational power, could become negative, a negative power request is possible. In

cases where the power request is negative, *energy recovery* is possible. Using a generator in combination with a storage device, energy can be recovered, temporarily stored, and used later to provide tractive power such that less power from the combustion engine is required. This is one of the major benefits of hybrid techniques, especially for heavier vehicles and for velocity profiles with fast changes in speed or for elevation profiles with steeper grades.

Apart from the power at the wheels, P_w, the engine also provides the power for (electric) auxiliaries, P_l. By reducing the power requests for these power sinks, e.g., by employing better air conditioning systems, or by using HID or LED lamps, in-use fuel economy will improve.

1.1.2.2 Engine Power

Let us now look at improvements in fuel economy by providing the power requests, P_w and P_l, in a fuel effective manner. This can be influenced by avoiding or reducing losses in the engine and the drivetrain. Examples are the use of variable speed pumps, low friction lubricants, intelligent maintenance, etc. Most of these technologies are available commercially, are cost effective, but have a low market share.

Because the engine and drivetrain losses depend on the *working point* of these devices, e.g., torque and rotational velocity, and a certain power can be provided by several combinations of these variables, by employing different gear settings, the shifting strategy can be optimized towards better fuel economy. Moreover, the size of the combustion engine has considerable influence on fuel economy. A large engine has a large maximum power output, however, also a large internal drag. An engine can be *downsized*, such that fuel economy is improved. Combining downsizing with a reduction of vehicle inertia is highly profitable, because then the smaller engine still enables a desired level of acceleration, while both the required power to do so and the drag torque are reduced.

A hybrid drivetrain, see Fig. 1.5, has additional options for influencing the working point, and is not limited to a few settings of gear ratios. In hybrid drivetrains, there are three possibilities to meet the power request:

$$P_w = P_p + P_m + P_k, \tag{1.2}$$

in which P_p denotes the prime mover output power, P_m the output power of the secondary power converter(s), and P_k the power delivered by the service brakes. Those options will also generate additional opportunities for setting the optimal gear (Ngo et al. 2012).

The prime mover converts a fuel flow P_f from one of the fuel-based energy carriers of Fig. 1.1 with an irreversible process into output power P_p, therefore, $P_f \geq 0$. The secondary power converter could operate both as a motor and a generator, converting P_m into storage power P_s, or *vice versa*. The service brakes convert useful energy into heat, so $P_k \leq 0$.

The losses of the secondary power converter are in general a nonlinear function of the working points of the device, just as for an engine. The hybrid system has the

freedom to govern the working points of the drivetrain in a way that the combined cost is minimized.

When part of the power requirements for a certain performance of the vehicle is covered with the secondary power converter, the engine can be further downsized, such that fuel economy is improved while driving performance is maintained. The coverage of peak power with the secondary power converter also allows the use of an Atkinson cycle engine, which has lower thermal losses due to a lower gas pressure at the end of the combustion stroke.

Furthermore, the hybrid system allows for *stop–start* of the prime mover. In cases where the secondary power converter has enough tractive power, the prime mover can be stopped such that idle losses of the prime mover are eliminated while the launch time of the vehicle is not compromised. The emission of the vehicle can also be temporarily reduced, e.g., when driving in a city center, by using stop–start features.

In summary, the main advantages of hybrid vehicles are:

- the kinetic and potential energy can be recovered and stored, such that it can be used at a later, more convenient, time to propel the vehicle,
- the working points of the prime mover and the secondary mover can be shifted to points that will yield an improved overall fuel economy,
- the prime mover can be downsized, such that average fuel economy is improved,
- the prime mover can be stopped, so idle losses are eliminated and emissions are locally reduced.

1.1.3 Hybrid Technology

So far, the advantages of hybridizing a vehicle are outlined. Possible disadvantages are the added complexity and the additional cost that the hybrid system brings along. Nevertheless, this technology has the highest potential for improving fuel economy (IEA 2009, p. 155), and although the technology is cost effective (IEA 2009, p. 169) it has a relatively high cost and is not particularly mature. A cost estimate for hybridizing a light-duty vehicle is EUR 2 750 (IEA 2012, p. 19) while for a short-haul, medium freight truck it is USD 30 000–33 000 (IEA 2012, p. 25). Market acceptance would be much better if fuel economy could be further improved, e.g., by optimizing the Atkinson cycle engine over a broad speed range or by using optimal control with reliable preview. It would also be better if the cost would be lower, e.g., by improved battery life, by higher energy density of batteries, or by integrated thermal management. It is, therefore, worthwhile to study this technology because there is still much room for improvement.

Careful design and operation of a hybrid vehicle is required, which involves several choices regarding:

- energy sources,
- topology,
- component size,
- control strategy.

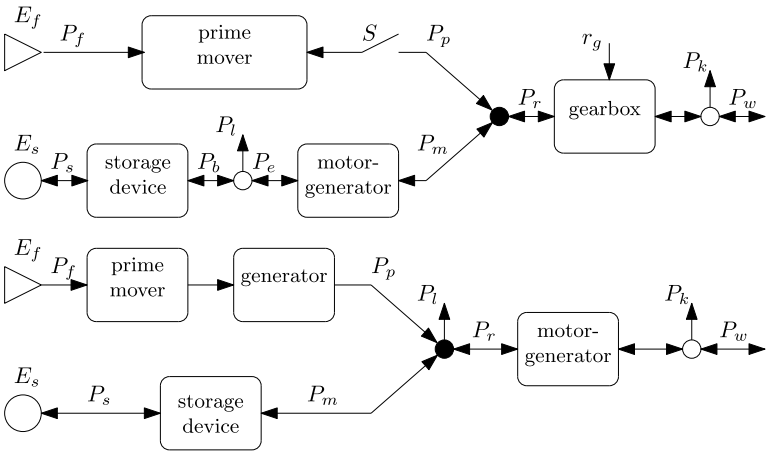

Fig. 1.5 Parallel (*top*) hybrid versus series (*bottom*) hybrid drivetrain topology

First, choices can be made regarding the energy carrier of the prime mover, see Fig. 1.1, and the quantity in which the secondary power converter converts the recovered energy. Possible choices for the hybrid system are electric, hydraulic, mechanic, and pneumatic applications. The theory developed in this book mainly focuses on a (diesel powered) internal combustion engine in combination with an electric machine as secondary power converter. However, the topics treated can also be applied to other choices.

Second, the topology of the drivetrain has to be designed. Two types of hybrid topology that can be found are parallel ones and series ones, see Fig. 1.5. The main difference between a parallel and a series topology is that the parallel one has a mechanical coupling between the prime mover and the wheels while the series one has not. In a series topology, the clutch and gearbox can be omitted, on the other hand, an additional generator is required and the electric machines have to deliver the full power. Advantage of the series topology is that the prime mover can operate in its optimal working point, and transmission losses in the gearbox are omitted. The improvement of the prime mover should out weigh the added losses due to the energy conversion in the two motor-generators.

More involved topologies can also be found, e.g., a combination of parallel and series hybrid topology. These parallel-series topologies have both a mechanical and electrical connection between the prime mover and the wheels. This adds additional control freedom, however, also requires an increased number of components and cost.

For long-haul trucks that drive mostly on highways, the engine has a favorable working point during cruise speed if the engine has a direct connection to the wheels. Here, the parallel topology often offers the best fuel economy potential. If other objectives are imposed, such as noise reduction and comfort, a series hybrid topology could be favored. For light-duty vehicles more variation is found in the topologies employed.

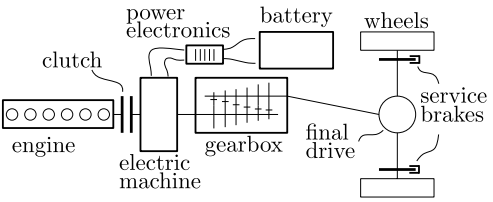

Fig. 1.6 Parallel drivetrain of a hybrid electric vehicle

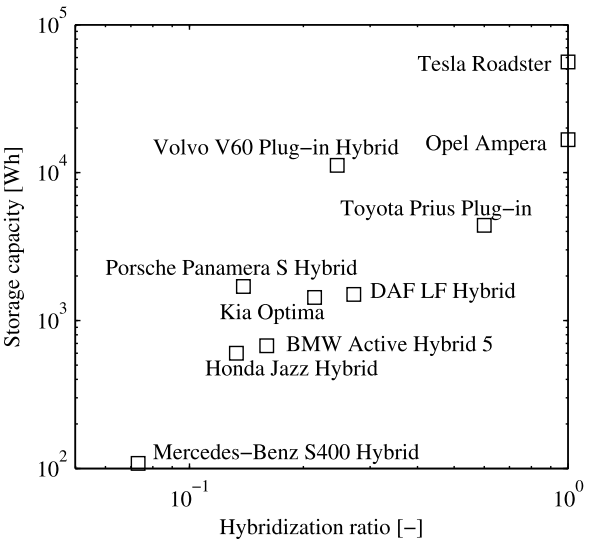

Fig. 1.7 Overview of storage capacity and hybridization ratio for some hybrid/electric vehicles available in 2013. Note the positive correlation: a large hybridization ratio is normally related to a large storage capacity and *vice versa*

A topology often used for heavy-duty vehicles is depicted in Fig. 1.6. It is acknowledged that both Figs. 1.5 and 1.6 depict only some possible layouts. The position of several components can be changed, e.g., the gearbox and clutch can be placed before or behind the secondary power converter. Moreover, the number of secondary power converters is not necessarily limited to one. For a detailed description of hybrid vehicle topology design, the reader is referred to, e.g., Hofman (2007).

The third design choice is the size of the components, i.e., the maximum output power of the prime mover and secondary power converter(s) and the capacity of the storage device. The optimal component size requires a balance between investment cost, operational cost and performance. A key design parameter is the *hybridization ratio*, the ratio of the maximum recovery power to the total available tractive power. The storage capacity is also a design variable. This is illustrated with an overview of these last two variables for vehicles that are currently available on the market, see Fig. 1.7.

Finally, the design of a control algorithm that governs the hybrid drivetrain components is required. The remainder of this book concentrates on control strategies for hybrid drivetrains, detailed in the next section.

1.2 Control Challenges for Hybrid Electric Vehicles

Control of hybrid drivetrains can be seen as hierarchical control with several levels, namely component and supervisory (integrated) level. This section concentrates on control at the supervisory level.

The main *control objective* for this book is to improve fuel economy, i.e., to minimize the cumulative fuel consumption $E_f = \int P_f \, \mathrm{d}t$. Control problems that deal with optimization as objective are often referred to as optimal control (Pontryagin et al. 1962; Clarke 1983; Vinter 2000; Geering 2007).

To achieve an improvement in fuel economy a hybrid vehicle provides several *control inputs*. In case of a parallel hybrid topology this involves, e.g.,

- power of the primary power converter P_p,
- power of the secondary power converter(s) P_m,
- power of the storage device P_s,
- power of the service brakes P_k,
- gear ratio r_g,
- clutch position S,

see again Fig. 1.5.

Section 1.1.2 showed that fuel economy can be improved by reduced cumulative power requirements and an optimal division of the power request over the different power converters. Therefore, it is useful to define the following *control signals* that are directly related to the objectives:

- the combined power output of the power converters, $P_w = P_p + P_m + P_k$,
- the division of the power request over the primary and secondary power converter, P_p and P_m, or any other signal directly related to these.

The control of the tractive power at the wheels, P_w, to achieve a velocity is known as *cruise control*. The supervisory control algorithm using the hybrid control input, dealing with the balanced generation and re-use of stored energy such that fuel consumption is minimized, is called *Energy Management Strategy* (EMS).

The control strategy has limited freedom because the control actions are subject to several *constraints*:

- average velocity (travel time), maximum velocity of the vehicle (speed limits), and distance covered by the vehicle (traveled distance),
- velocity limitations of the power converters, the rotational velocity of prime and secondary power converter is bounded,
- power limitations of the power converters, the power throughput of the power converters is bounded,
- storage device energy level, the level is between empty and full,
- temperature limitations of power converters and storage device, the temperature may not be too low or too high.

Apart from the constraints, a challenge in the control of hybrid drivetrains is the hybrid nature of clutch and gear operation as well as the nonlinear description of

the power converters that result in a non-convex cost function. This complicates the use of optimization methods. Other challenges are that future conditions, influencing power request P_w and velocity v, are not known a priori, because they depend on, e.g., vehicle mass, road angles, and weather conditions. Also, real-time implementation in series production vehicles forces the use of standard hardware with limited computational power and limited memory capacity. A real-time controller has to deal with these issues. Inputs for a real-time controller are the actual vehicle velocity and power requests from the driver (accelerator and brake pedal position).

The fuel optimal control problem is often simplified such that part of the difficulties can be ignored, to deal with the constraints and challenges described earlier. This requires a trade off between the model description complexity and the number of control variables of the problem that is considered. Different approaches can be found in literature, each method with its own objective and dealing with the trade-off in its own way. In practice, often heuristic-based strategies are applied to deal with the computational power limitations. Implementations of optimal control-based strategies are scarce.

Algorithms dealing with the combined optimization of vehicle velocity and operation of the hybrid drivetrain components are relatively new. When traffic situations impose strict velocity limitations, the optimization of the drivetrain operation can be separated from the velocity control.

To find an optimal topology and component size, and so address the potential benefits of hybridizing the drivetrain, it is common practice to use measured velocity and power requests, e.g., obtained with a conventional vehicle on a prescribed duty cycle. This is not a viable solution for real-time control.

It is sometimes possible to estimate the future power and velocity trajectories based on information coming from a geographical information system or from signals available in the vehicle. When this information is available, the techniques treated in this book will enable the computation of the optimal control signal, handling all constraints mentioned, in real-time. This will give the best fuel economy possible, within the technological limitations. When this information is *not* available, a straightforward modification will suffice to compute the optimal control signal again, also in real-time, with only two disadvantages: (i) a single parameter characterizing the route needs to be estimated based on information from the past, (ii) it is more difficult to enforce constraints on the level of the storage device, which may eventually lead to a suboptimal solution. We detail these approaches in the remainder of this book.

1.3 Bibliographical Notes

The concern about future disasters, be it due to overpopulation, loss of energy security, global warming, or any other potential risk scenario, seems to be intimately tied to the human race, because this concern already started eons ago. A suitable starting point could be seen in tales of old, like the widespread stories about a great

Flood. More recently, one can think of the Malthusian catastrophe where growth of the population outpaces agricultural production. It is not a big step to apply the same ideas on energy or other scarce resources, as was done more recently in the reports of the Club of Rome. Disasters have also been a popular subject in old and contemporary art.

A counter argument against these disaster predictions that mostly stem from a "business as usual" extrapolation, was found in the flexibility and adaptability of mankind, who has always provided, in the long run, notwithstanding local disasters such as famines, epidemics and wars. The main mechanism encountered is that necessity accelerates the accumulation of knowledge and its deployment. It is then beneficial to guide the development of technology by predictions of what could happen in the future. This is one of the goals of technology road maps, to give an indication where research and development can be expected to pay off, e.g., to provide feasible paths towards a sustainable society.

Recent overviews and technology road maps in the area of energy conservation, also focused on the transportation sector, are provided by the International Energy Agency, see, e.g., IEA (2011a, 2011b, 2012). These road maps are based on a more generic vision towards the energy use of the transport sector as presented in IEA (2009). Some alternative future projections are available from independent research by universities, see, e.g., Bandivadekar et al. (2008), McKinnon (2008). To get a good grip on current trends or to assess the effect of regulatory measures, reliable data are necessary. It is difficult to obtain this, e.g., for the amount of empty running, see McKinnon (2010) for a discussion on this topic.

References

ACEA (2010) Commercial vehicles and CO_2. http://www.acea.be/images/uploads/files/20101013_Commercial_Vehicles__CO2.pdf

Al-Qadi IL, Elseifi MA (2007) New generation of wide-base tires: impact on trucking operations, environment, and pavements. Transp Res Rec 2008(1):100–109

Alam AA, Gattami A, Johansson KH (2010) An experimental study on the fuel reduction potential of heavy duty vehicle platooning. In: Proc IEEE conf intell transp syst. IEEE, New York, pp 306–311

Anderson CD, Anderson J (2010) Electric and Hybrid Cars: A History, 2nd edn. McFarland & Company, Inc., Jefferson, NC, USA

Bandivadekar A, Bodek K, Cheah L, Evans C, Groode T, Heywood J, Kasseris E, Kromer M, Weiss M (2008) On the road in 2035: reducing transportation's petroleum consumption and GHG emissions. Tech rep LFEE 2008-05, RP, Massachusetts Institute of Technology

Benz KF (1886) Fahrzeug mit Gasmotorenbetrieb. Patent nr 37435

Clarke FH (1983) Optimization and nonsmooth analysis. Wiley, New York

Edwards R, Larivé JF, Mahieu V, Rouveirolles P (2006) Well-to-wheels analysis of future automotive fuels and powertrains in the European context. WELL-TO-TANK report version 2b. European Commission Joint Research, Centre, Institute for Environment and Sustainability

Franzese O, Davidson D (2011) Effect of weight and roadway grade on the fuel economy of class-8 freight trucks. Tech rep ORNL/TM-2011/471, Oak Ridge National Laboratory. http://cta.ornl.gov/cta/Publications/Reports/ORNL_TM_2011_471.pdf

Franzese O, Knee HE, Slezak L (2010) Effect of wide-based single tires on fuel efficiency of class 8 combination trucks. Transp Res Rec 2191(1):1–7

Geering HP (2007) Optimal control with engineering applications. Springer, Berlin

Hofman T (2007) Framework for combined control and design optimization of hybrid vehicle propulsion systems. PhD thesis, Technische Universiteit Eindhoven, Eindhoven, The Netherlands

IEA (2007) World Energy Outlook 2007. Stedi media. Paris, France

IEA (2009) Transport, energy and CO_2: moving towards sustainability. International Energy Agency, Paris. http://www.iea.org/publications/freepublications/publication/transport2009.pdf

IEA (2010) Transport energy efficiency: Implementation of IEA recommendations since 2009 and next steps. Tech rep, International Energy Agency. http://www.iea.org/publications/freepublications/publication/transport_energy_efficiency.pdf

IEA (2011a) Technology roadmap: biofuels for transport. Tech rep, International Energy Agency. http://www.iea.org/publications/freepublications/publication/Biofuels_Roadmap.pdf

IEA (2011b) Technology roadmap: electric and plug-in hybrid electric vehicles. Tech rep, International Energy Agency. http://www.iea.org/publications/freepublications/publication/EV_PHEV_Roadmap.pdf

IEA (2012) Technology roadmap: fuel economy of road vehicles. Tech rep, International Energy Agency. http://www.iea.org/publications/FuelEconomy_2012_final_web.pdf

Van Keulen T, Naus GJL, De Jager B, Molengraft MJG, Steinbuch M, Aneke NPI (2009) Predictive cruise control in hybrid electric vehicles. In: Proc internat battery, hybrid and fuel cell electric veh symp. Stavanger, Norway, 6 pages

Van Keulen T, De Jager B, Foster D, Steinbuch M (2010) Velocity trajectory optimization in hybrid electric trucks. In: Proc American control conf, Baltimore, MD, USA, pp 5074–5079

Lahrmann H, Agerholm N, Tradisauskas N, Berthelsen KK, Harms L (2012) Pay as you speed, ISA with incentives for not speeding: results and interpretation of speed data. Accid Anal Prev 48:17–28

McKinnon A (2008) Advice on CO_2 emissions from the UK freight transport sector. Tech rep, Heriot-Watt University, Edinburgh, UK. http://www.theccc.org.uk/pdfs. Advice to the Shadow Climate Change Committee (revised and corrected version for website).pdf

McKinnon A (2010) European freight transport statistics: limitations, misinterpretations and aspirations. Tech rep, Heriot-Watt University, Edinburgh, UK. http://www.acea.be/images/uploads/files/20101116_SAG_Report.pdf

Mock P, German J, Bandivadekar A, Riemersma I (2012) Discrepancies between type-approval and "real-world" fuel-consumption and CO_2 values: assessment for 2001–2011 European passenger cars. Working paper 2012-2, ICCT, Washington, Berlin, San Francisco. http://www.theicct.org/sites/default/files/publications/ICCT_EU_fuelconsumption2_workingpaper_2012.pdf

Naus GJL, Vugts RPA, Ploeg J, Van de Molengraft MRJG, Steinbuch M (2010) String-stable CACC design and experimental validation: a frequency-domain approach. IEEE Trans Veh Technol 59(9):4268–4279

Ngo V, Hofman T, Steinbuch M, Serrarens A (2012) Optimal control of the gearshift command for hybrid electric vehicles. IEEE Trans Veh Technol 61(8):3531–3543

Pontryagin LS, Boltyanskii VG, Gamkrelidze RV, Mischenko EF (1962) The mathematical theory of optimal processes. Wiley, New York

Sierra (2011) CAFE: the truth behind the testing. http://www.sierraclub.org/transportation/downloads/2011-07-Truth-in-Testing-Report.pdf

Vinter R (2000) Optimal control. Systems & control: foundations & applications. Springer, New York

Chapter 2
Cyber-physical Modeling of Hybrid Vehicles

2.1 Introduction

For model-based control of *hybrid vehicles*, an appropriate model is essential. Here, we explain that "appropriate" needs to be read in the context of the goal of the model. It does not make much sense to derive a model taking all possible physical effects into account, to realize later that the data available to validate the model come from experiments which are not particularly reproducible or do not provide enough or accurate enough information, or that the model does not integrate well with computational processes. We also do not need all possible accuracy for control because feedback is quite robust. Therefore, we need to use, and have the freedom to use, approximate models, which should cover the main characteristics of the physics, allow extensive analysis and be implementable in real-time situations for online control. The last characteristic will shift in time, what is not possible today will be possible in a few years. It allows us to aim for the boundaries of what is technically possible today, knowing it will be easy to achieve in the future. All components of the drivetrain need those models, which means internal combustion engine, electric machine, battery, and their interconnections. We primarily use prescribed or registered drive cycles, so do not consider driving and drivability issues. We focus on system level control, not on component level control. Thus, torque- or current-based models will get limited attention. Power-based models will receive full consideration.

There are several approaches to modeling system components, and the complexity of available models may vary widely. For example, *combustion engine* models may be crank angle resolved, or crank angle averaged, or even quasi-static. The same variety holds for *electric machine* models. Crank angle resolved or averaged models are useful for the design of component controllers, e.g., engine controllers that determine the valve, fuel injection or spark ignition timings, or that select the exhaust gas recirculation or inlet manifold boost pressure. Those models are more complicated than needed and do not allow an extensive analysis of the basic problem. They also model phenomena that are of no interest for the basic problem. This is due to the slow storage dynamics of the storage devices, which normally take on the order of several minutes or hours to be discharged or charged. Some electro-chemical

B. de Jager et al., *Optimal Control of Hybrid Vehicles*, Advances in Industrial Control,
DOI 10.1007/978-1-4471-5076-3_2, © Springer-Verlag London 2013

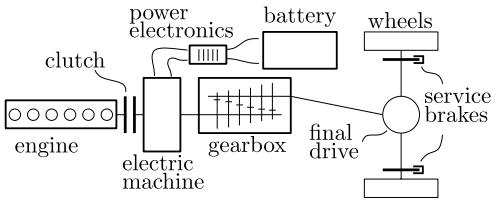

Fig. 2.1 Overview of drivetrain components in a parallel hybrid electric truck. Note the connecting elements clutch, axle, gearbox, final drive, and power electronics besides the power converters (engine and electric machine) and battery

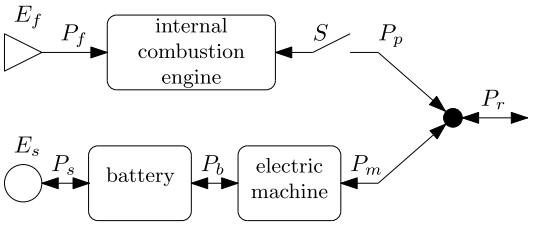

Fig. 2.2 Schematic overview of a hybrid drivetrain including the internal combustion engine (chemical to mechanical power converter), the electric machine (electrical to mechanical power converter), and the battery (electro-chemical to electrical power converter). A switch, S, represents the clutch. Other connecting elements are indicated by arrows representing power transfer over a powernet (e.g., realized with a wiring harness). The *arrows* are one-sided for irreversible processes and two-sided for reversible processes. Energy storage is represented by E_f (fuel tank) and E_s (battery). The *solid circle* represents power compounding. Compared to Fig. 1.5 P_l is omitted

processes in a *battery* may be much faster than that, however, but the dominant time scale is in the order of minutes. It is also due to the slow temporal changes in power flow in the vehicle, based both on data from the drive cycles, which are typically time resolved at 1 [s] intervals, and on real practice, where a human driver will not perpetually change his demands in split seconds because this is not compatible with the normal flow of traffic. This implies that time needs to be resolved in the order of seconds. Because the usual power converters have a cycle time below 0.1 [s], angle resolved or even angle averaged models provide too much detail. We will, therefore, use quasi-static models for the power converters and a low order dynamic model for the storage device. The remainder of this chapter will provide details.

2.2 Hybrid Vehicle Definitions

Figure 2.1 shows an example of a drivetrain layout for a hybrid electric truck. An overview of these components and their interconnections is presented in this section.

Figure 2.2 depicts a schematic overview of a hybrid electric drivetrain. The mechanical output power of the internal combustion engine P_p and electric machine

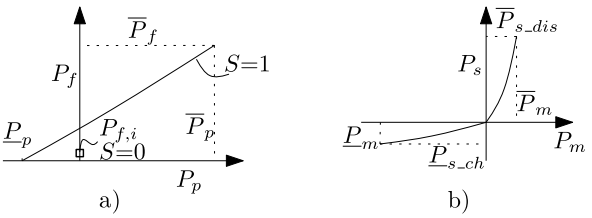

Fig. 2.3 Schematic cost functions of (**a**) internal combustion (Diesel) engine and (**b**) electric machine and battery. Note that with the clutch open the engine may run at idle speed, indicated by the □, but could also be stopped to achieve $P_f = 0$. Furthermore, for $P_p < 0$ the fuel use P_f is interpolated, but for some engines, e.g., Otto engines, this is not possible and the only feasible operating point is then $P_p = \underline{P}_p$ when the fuel flow is cut off

P_m matches the power requested by the driver or cruise controller P_r:

$$P_r = P_p + P_m \tag{2.1}$$

because there is no possibility to store energy in this point. The torque conversion is supposed to be perfect, so power is just added or subtracted, which is most easily achieved if combustion engine and electric machine are put on the same axle.

The conversion of fuel power P_f to the engine output power P_p is modeled as a function of the power throughput:

$$P_f(S, \omega, P_p) = \begin{cases} P_{f,i} & \text{for } S = 0, \\ P_{f,p}(\omega, P_p) & \text{for } S = 1, \end{cases} \tag{2.2}$$

where S is a Boolean variable modeling clutch opening, $P_{f,i} \geq 0$ is the fuel power during idling, $P_{f,p}$ is the fuel power if tractive power is delivered, and ω is the rotational velocity. If $S = 0$ than $P_p = 0$. When stop-start of the engine is possible then $P_{f,i} = 0$ if $S = 0$, see Fig. 2.3a. Section 2.3.1 presents typical relations for P_f.

The fuel power P_f is related to the fuel mass flow rate $\dot{m}_f$ (or fuel rate, for short) by the lower heating value, h

$$P_f = h\dot{m}_f.$$

The characteristics of the hybrid drivetrain components require a non-smooth model in many hybrid vehicle applications, where charging and discharging is modeled with a non-smooth continuous function, see Fig. 2.3b. The combined conversion of storage power P_s to the electric power P_b, and of P_b to the mechanical power P_m is, therefore, modeled as a non-smooth function of the power throughput:

$$P_s(P_m, E_s) = \begin{cases} P_{s\_\mathrm{ch}}(P_m, E_s) & \text{for } P_m < 0, \\ P_{s\_\mathrm{dis}}(P_m, E_s) & \text{for } P_m \geq 0, \end{cases} \tag{2.3}$$

with $P_{s\_\mathrm{ch}}(0, E_s) = P_{s\_\mathrm{dis}}(0, E_s)$, in which P_{s_ch} is the storage power during charging of the battery and P_{s_dis} the storage power during discharging of the battery,

see Fig. 2.3b. The conversion process (2.3) could depend (smoothly) on the stored energy in the battery E_s. It is assumed that the influence of other variables on the conversion losses, e.g., rotational velocity of the electric machine, temperature, and aging are known, and are incorporated in the power conversion function at time t. Note also that the drag power of the electric machine is always present (since decoupling the electric machine from the wheels is not possible in the topology considered) and is incorporated in the power request P_r such that $P_m = 0$ if $P_s = 0$. Typical relations for P_m and P_b are in Sect. 2.3.2 while those for P_b and P_s are in Sect. 2.3.3.

2.3 Models of Hybrid Powertrain Components

Mathematical models will be presented, together with a physical interpretation of models and model assumptions. Those models will describe the system dynamics in a rudimentary form. They will represent, in an approximate way, the power losses incurred by the power converters, and they will stress the physical, technical, and economic limitations on power flows and energy levels.

2.3.1 Combustion Engine

The derived models try to give a sufficiently accurate relation between the mechanical power delivered by an engine and the chemical power (fuel power) needed. Several models are possible that try to represent experimental data but also try to have a (very) simple representation. Different trade-offs are possible, resulting in models of different complexities.

It is beneficial to analyze some experimental results, and extract characteristic properties from these results, before presenting the models.

An example of the fuel use for a naturally aspirated spark-ignition (Otto) engine for a mid-sized passenger car is given in Fig. 2.4. Another example is for a compression-ignition (Diesel) engine used in a delivery truck in Fig. 2.5.

Note that both these figures represent the same type of data, but the data are presented in a totally different way, enabling a different view on the data. A representation like Fig. 2.4 of the data in Fig. 2.5 is given in Fig. 2.6.

The main contributing factors to fuel use are

1. the delivered mechanical power, $P_p = \omega T_p$, as can be seen from the slope of the fuel use curve as a function of power, see Figs. 2.4 and 2.6,
2. the rotational speed, ω, which influences the drag losses as can be seen from the drag torque curve, where $P_f = 0$, in Fig. 2.5.

There are many more factors influencing fuel use, such as air properties like temperature, pressure, and humidity, fuel properties like fuel composition (blend), octane

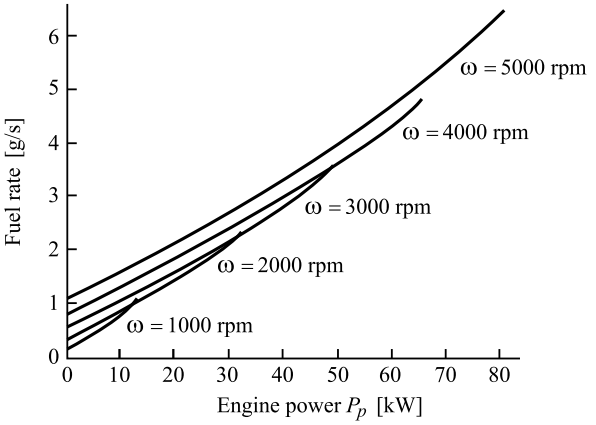

Fig. 2.4 Interpolated line plot of spark-ignition engine fuel rate as a function of mechanical power P_p at the crankshaft and of crankshaft rotational velocity ω under steady-state conditions, for a set of different velocities. Note that these data, especially near maximum torque requests, need to be approximated by at least a quadratic relation. The fuel rate increase near maximum torque is typically related to an enriched fuel mixture commanded by the engine controller and meant to cool the valves

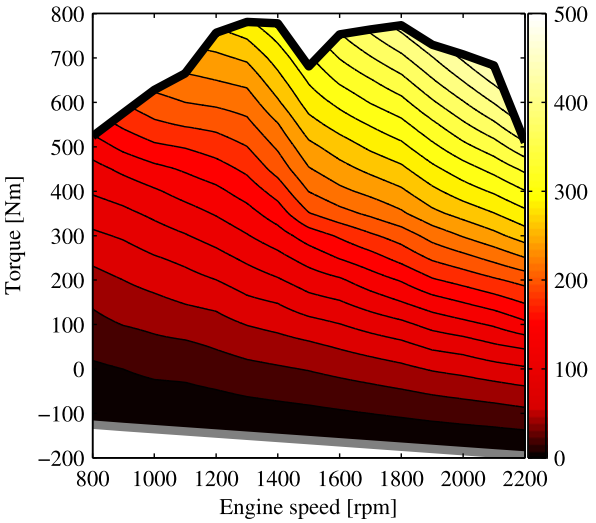

Fig. 2.5 Interpolated and quantized contour plot of measured diesel engine fuel power consumption P_f as a function of reconstructed crankshaft torque T_p and measured crankshaft rotational velocity ω_p under steady-state conditions, for a set of different velocities and gas pedal positions. The *dark line* indicates the maximum engine torque, $\overline{T}_p$, and the *gray line* indicates the engine drag torque, $\underline{T}_p$, while different color shades represent different fuel consumption levels as indicated by the right-hand scale in [kW]. The most efficient operating points are those with a hyperbola (constant mechanical power level) as tangent. The dip in maximum torque at $\omega_p \approx 1500$ [rpm] is due to emission restriction measures in the engine controller

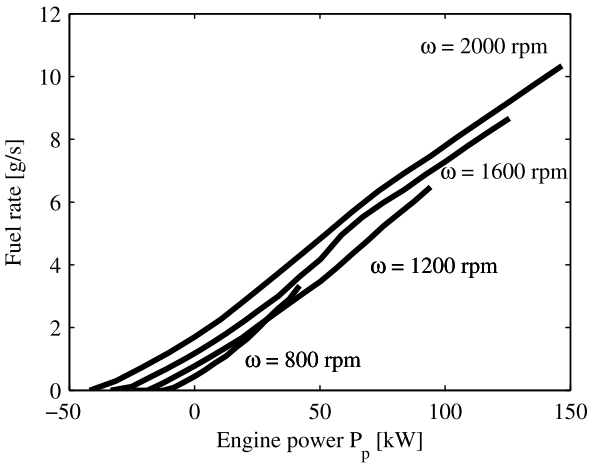

Fig. 2.6 Interpolated line plot of compression-ignition engine fuel rate as a function of mechanical power P_p at the crankshaft and of crankshaft rotational velocity ω under steady-state conditions, for a set of different velocities. Note that a *straight line*, with off-set depending on velocity ω, could be used to approximate these data, but essentially the data do not quite lie on a straight line, in particular at low speeds, and do not even represent a convex relation. On the other hand, some variability in the data is created by the engine controller trying to meet emission standards in certain critical operating points defined in the test procedure, but for a hybrid drivetrain with a lower fuel throughput, so lower emissions, another calibration without this variability can be permitted

number, and volatility, engine properties like age, wear, and maintenance state, etc., but in particular measures built into the engine controller that aim at reducing emissions. It is assumed that most of these effects are averaged out, are sufficiently small to be neglected, or can be included via model parameters.

The main differences between fuel rate results for Otto and Diesel engines or between light and heavy-duty engines are that

1. the fuel rate as a function of delivered power appears to be straighter for a Diesel engine than for an Otto engine, so for a Diesel engine an affine relation may be appropriate, whereas for an Otto engine a strictly convex relation may be better, although more careful analysis shows that this depends for a large part on the engine controller calibration, so that is the distinguishing feature,
2. drag losses are higher for heavy-duty engines than for light-duty engines, leading to higher overall losses for heavy-duty engines compared to light-duty engines for the same power fraction, compare Figs. 2.4 and 2.6, but the dependency on rotational speed looks similar and could be represented by a convex relation,
3. for Otto engines, at part load, throttling losses occur, contrary to Diesel engines, leading to higher intermediate power losses for Otto engines compared to Diesel engines from the same duty category, yielding a higher slope in an affine relation,
4. Diesel engines profit from a higher compression ratio and thus higher combustion temperatures, yielding a shallower slope in an affine relation.

It appears that static engine models do not need to distinguish between Otto and Diesel engines or between light and heavy-duty engines, the same relations with different numerical values could do. For engine models, one could distinguish between calibrations used in the engine controller, and, based on that, choose a different model structure. We therefore present several models that differ in the description of the influence of power output and fuel use to accommodate this. All models separate the influence of P_p and ω, i.e., the approximating functions are separable.

2.3.1.1 Willans Line (Affine) Model

The fuel consumption of an engine, e.g., the Diesel engine presented in the previous section, at rotational velocity ω, can be approximated with a piecewise affine relation, sometimes referred to as a Willans line approximation (Guzzella and Sciarretta 2005, p. 44):

$$\frac{P_f(\omega, P_p)}{\overline{P}_p} = \max\left(0, \gamma_{p,0}(\omega) + \gamma_{p,1}\frac{P_p}{\overline{P}_p}\right), \tag{2.4}$$

where $P_f \geq 0$ is the fuel power, $\gamma_{p,0}(\omega) > 0$ describes the velocity dependent engine drag loss, ω represents the rotational velocity of the drivetrain, $\overline{P}_p$ denotes the maximum power output of the engine, and $\gamma_{p,1} > 1$ is a fuel conversion parameter, see Table 2.1, p. 29, for the values. For component sizing problems, it is convenient to incorporate the maximum power output of the power converters in the cost functions. This also make comparisons between engines, using normalized functions and parameters, easier. At zero fuel consumption, $P_f = 0$, the engine drag power $\underline{P}_p$ is:

$$\frac{\underline{P}_p(\omega)}{\overline{P}_p} = \frac{-\gamma_{p,0}(\omega)}{\gamma_{p,1}} < 0. \tag{2.5}$$

The power of a combustion engine, or any other primary power converter, is limited, where the limit depends on the rotational velocity:

$$\underline{P}_p(\omega) \leq P_p \leq \overline{P}_p(\omega), \tag{2.6}$$

where the admissible range for P_p may be further restricted due to relation (2.1).

2.3.1.2 Strictly Convex Polynomial Equation Model

The fuel use of an engine, e.g., the Otto engine presented in the previous section, at rotational velocity ω, can be described by a strictly convex function, for which we choose a quadratic one with no provision for scaling as we will not use this model for component sizing problems

$$P_f(\omega, P_p) = \max\left(0, \gamma_{p,0}(\omega) + \gamma_{p,1}P_p + \gamma_{p,2}P_p^2\right), \tag{2.7}$$

with $\gamma_{p,1} > 1$ the linear fuel conversion parameter, and $\gamma_{p,2} > 0$ the quadratic fuel conversion parameter. These will be fitted in such a way that an accurate local approximation is achieved towards the measured fuel rate data. The interval of fitted data will be determined by the nominal value of P_p and the range in power achievable by manipulating the electric machine mechanical power, P_m, while still meeting the traction power requested, P_r. Note that this model is only valid in a restricted interval for P_p, because if $P_p \ll 0$ it gives $P_f > 0$, which will not occur in practice. Relations similar to (2.6) also hold.

2.3.2 Electric Machine

Different electric machines are used in HEVs. They may range from up-scaled alternators to powerful direct drive solutions. Here, we present a model for a powerful 44 [kW] motor/generator, but other electric machines could use the same model, albeit with different numerical values.

The motor/generator model, including the power electronics (inverter) used to get the correct DC conditions for the battery, is based on experimental data obtained in equilibrium points. The model aims to present the power losses accurately, but does not aim to represent transient behavior. The power losses could be represented by a (multi-dimensional) table, but are here fitted with simple analytical expressions to allow for deeper analysis.

The conversion of electric machine mechanical power, P_m, to electrical power, P_b, and vice versa, is measured under steady-state conditions, see Fig. 2.7. An analysis of the data shows that a non-smoothness is present and that the relation is not necessarily convex. To indicate this, the gradient $\partial P_b / \partial P_m$, at one rotational velocity, is depicted in Fig. 2.8.

The conversion characteristics of the electric machine are approximated with two piecewise quadratic functions with a non-smooth convex union:

$$\frac{P_b(\omega, P_m)}{\overline{P}_m} = \begin{cases} \gamma_{m,0}(\omega) + \gamma^+_{m,1} \frac{P_m}{\overline{P}_m} + \gamma^+_{m,2} (\frac{P_m}{\overline{P}_m})^2, & \text{for } P_m \geq 0 \text{ (motoring)} \\ \gamma_{m,0}(\omega) + \gamma^-_{m,1} \frac{P_m}{\overline{P}_m} + \gamma^-_{m,2} (\frac{P_m}{\overline{P}_m})^2, & \text{for } P_m < 0 \text{ (generating)} \end{cases} \tag{2.8}$$

with the electric power P_b, electric machine drag function $\gamma_{m,0}(\omega) > 0$, parameters $\gamma^+_{m,1} > 1$, $\gamma^+_{m,2} > 0$, $\gamma^-_{m,1} < 1$, $\gamma^-_{m,2} > 0$, and the maximum motoring power of the electric machine $\overline{P}_m$ to allow for easy scaling of the size of the electric machine.

When the vehicle velocity and gearshift trajectory are prescribed, the rotational velocity ω, and parameters $\gamma_{p,0}$ and $\gamma_{m,0}$, are also known. It is assumed that the electric machine is always connected to the vehicle wheels such that the drag power of the electric machine $\gamma_{m,0}$ is present anyway, and can, therefore, be incorporated in the power request P_r. Furthermore, it is assumed that the relation $P_m \to P_b$ is monotonically increasing in the domain of interest, i.e., $\partial P_b / \partial P_m \geq 0$, see Fig. 2.8.

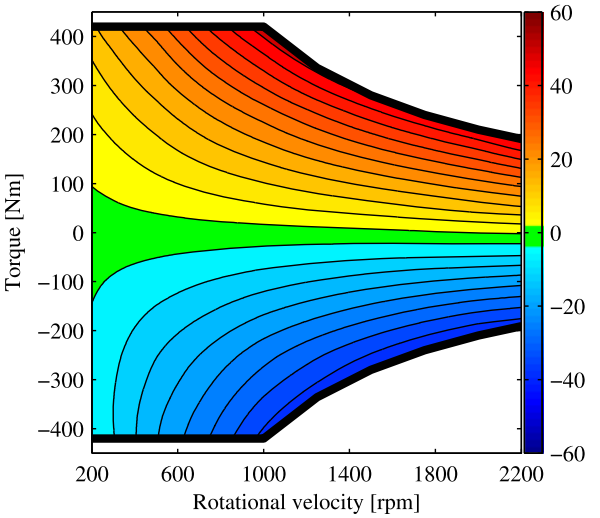

Fig. 2.7 Interpolated and quantized contour plot of electric power P_b as a function of electric machine torque T_m and rotational velocity ω_m. The *upper dark line* indicates the maximum electric machine torque $\overline{T}_m$, the *lower dark line* indicates the maximum generator torque $\underline{T}_m$, while *different color shades* represent different electric power levels as indicated by the right-hand scale in kW. The operating points with the smallest losses on a contour line are those with a hyperbola (constant mechanical power level) as tangent

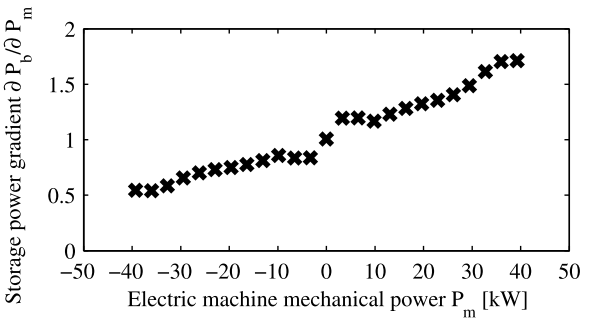

Fig. 2.8 Electric power gradient $\partial P_b / \partial P_m$ as a function of electric machine mechanical power P_m for rotational velocity $\omega = 1000$ [rpm]. The gradient is discontinuous, so the function $P_b(\omega, P_m)$ is non-smooth. Furthermore, since this gradient is evidently not a monotonic increasing relation, the functions $P_b(\omega, P_m)$, one for each interval of P_m, are not necessarily convex in P_m, but could be approximated as convex ones without large errors

Just as for the combustion engine, the electric machine power is limited

$$\underline{P}_m(\omega) \leq P_m \leq \overline{P}_m(\omega). \tag{2.9}$$

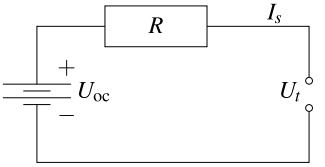

Fig. 2.9 Equivalent circuit for a battery. The open-circuit voltage U_{oc} will be a function of the state-of-energy E_s, but in principle not of P_s, while the terminal voltage U_t will be a function of P_s. The resistance R may be a function of temperature and of state-of-energy, or even of charging history, and may also attain values that differ for charging and discharging

The admissible range for the electric machine power may even be smaller, due to relation (2.1) and the limited power range for the primary power converter (2.6).

2.3.3 Storage Device

The main dynamics of an HEV storage device is rather slow compared to other components in the drivetrain, i.e., the characteristic time in which this device is charged or discharged is quite long. Therefore at least the storage dynamics needs to be accounted for, which can be done by a conservation law

$$E_s(t) = E_s(t_0) + \int_{t_0}^{t} -P_s(\tau)\,\mathrm{d}\tau, \tag{2.10}$$

where E_s is the energy stored in the battery and P_s is the power flow. The minus-sign is due to the convention that P_s is positive for power flowing out of the battery.

Apart from the conservation law, we need some constitutive relations from which the losses of the processes involved follow. These relations for storage devices—here we only consider electro-chemical storage—may differ depending on the electro-chemistry used. We consider two types, a battery model with *Ohmic losses*, based on an equivalent circuit, and a simplified model that could be found by fitting experimental data, but could also be found assuming a constant open-circuit voltage (or constant electro-motive force in electro-chemistry parlance), independent of the charge level. The constant open-circuit voltage assumption may be valid for Li-ion batteries with a flat characteristic or for lead-acid batteries in a restricted range of charge levels, but it will not be valid for, e.g., super capacitors in their full range.

To propose a reasonable model, first some experimental results are presented. They describe the battery voltage as a function of charge state. From that, the battery internal resistance can be reconstructed. The idea is to model the battery based on a circuit with a voltage source (battery open-circuit voltage) and a resistance, while only the battery terminal voltage and current are measurable, see Fig. 2.9. The power losses can then be computed from the current and the Ohmic loss due to the resistance, see Pop et al. (2008).

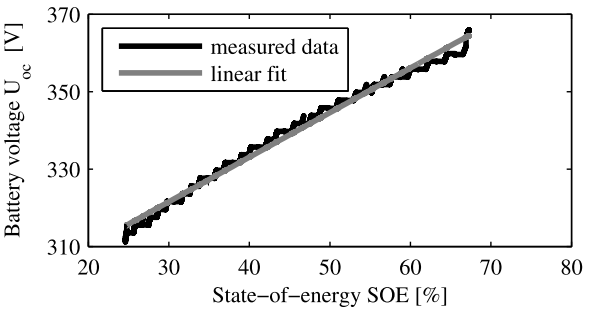

Fig. 2.10 Measured and quantized battery open-circuit voltage U_{oc} as a function of the state-of-energy SOE averaged over a slow charging/discharging cycle. This is a monotonic increasing relation, almost a straight line as indicated by the approximation: an affine relation

2.3.3.1 "Equivalent Circuit"-Based Battery Model

For a certain HEV storage system with Li-ion batteries, the open-circuit voltage U_{oc} is estimated by discharging the battery with the lowest possible current request (where the vehicle drives at a foot pace), see Fig. 2.10. Under the assumption that the internal resistance R is equal for charging and discharging (Pop et al. 2008), the measured terminal voltage U_t during charging and discharging is averaged to estimate U_{oc}. The measured voltage is quantized with a 2 [V] quantization interval. Given these data, obtained at an almost constant temperature, there is no way we can model the influence of temperature on the (dis)charging process, so this influence is neglected. In practice, the battery pack temperature is tightly controlled to avoid chemical process instabilities and is kept low to reduce battery wear, so this assumption seems reasonable.

Figure 2.10 shows that a fully charged battery has a higher voltage than a depleted battery. Therefore, a charged battery requires a lower current to deliver a certain power request, and the internal losses are then also smaller.

Given the estimated open-circuit voltage U_{oc}, the measured terminal voltage U_t and current I_s, the battery internal resistance is estimated with

$$R = \frac{U_{\text{oc}} - U_t}{I_s} = \frac{U_R}{I_s}, \tag{2.11}$$

where U_R is the voltage drop over the resistor. Here, charging and discharging are treated as equal. The computed internal resistance for one charge/discharge cycle is depicted in Fig. 2.11.

The battery open-circuit voltage U_{oc} is approximated with an affine function of the state-of-energy:

$$U_{\text{oc}}(E_s) = U_0 + \phi E_s, \tag{2.12}$$

where U_0 is the voltage of a fully discharged battery, $\phi \geq 0$ is the battery open-circuit voltage increase factor, and E_s is the energy stored in the storage device. This approximation is depicted in Fig. 2.10 and shows satisfactory agreement with the experimental data.

When E_s is expressed in a fraction (or %) of the fully charged E_s, i.e., the battery capacity E_c, it is denoted with SOE. The relation with the often used state-of-charge

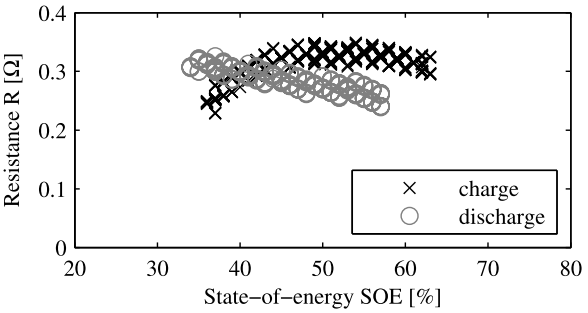

Fig. 2.11 Reconstructed battery resistance R as a function of the state-of-energy SOE for slowly charging and discharging. Both graphs are concave, are almost at the same level, and could be considered equal and constant given the wide spread in the data

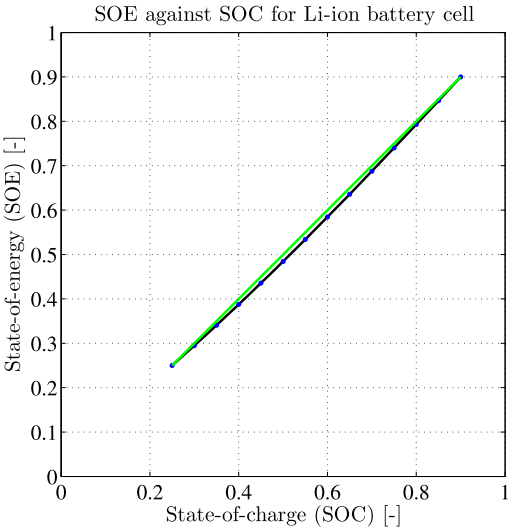

Fig. 2.12 State-of-energy versus state-of-charge for a single Li-ion cell. The figure uses experimental data directly (indicated with *circles*). Note that this graph can be shifted up or down, depending on the initial condition used when solving differential equation (2.13) for E_s, and it can be stretched, depending on the assumed energy capacity E_c. Here, it is re-normalized to match the diagonal (*green*) exactly in 2 points, so SOE and SOC are both equal at the values 0.25 and 0.90, marking the interval for which data are used. The diagonal (*green*) is obtained if a fixed value for U_{oc}, so ϕE_s is constant in (2.13), is used to compute E_s from I_s

$Q_s(t) = Q_s(t_0) + \int_{t_0}^{t} -I_s(\tau)\,\mathrm{d}\tau$, or SOC when expressed as a fraction of the total charge capacity of the battery, is via (2.12) and $P_s = I_s U_{\text{oc}}$, so

$$\dot{E}_s = -I_s(U_0 + \phi E_s). \tag{2.13}$$

An example for the relation between Q_s, or SOC, and E_s, or SOE, is in Fig. 2.12.

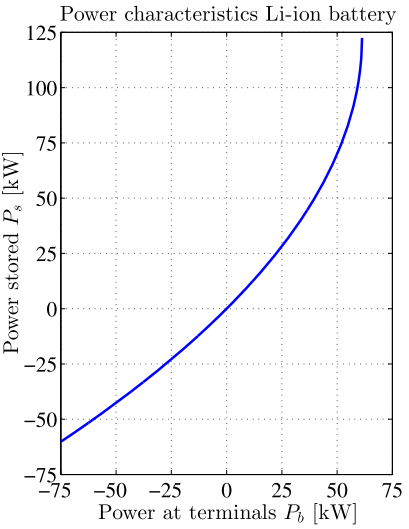

Fig. 2.13 Computed battery power at the terminals versus battery power stored for a Li-ion battery with the lowest possible $U_{\rm oc} = 280$ [V], representing the worst case with the highest losses. Note that for $P_b > 61.25$ [kW], corresponding to 122.5 [kW] for P_s, no solution is possible, i.e., no more than that amount of power can be extracted from the battery given the assumed electrical model for the battery, which becomes dubious for these power levels where U_t approaches $U_{\rm oc}/2$

It is suggested to approximate the battery loss power with an internal resistance model, Pop et al. (2008):

$$P_s(\omega, P_m, E_s) = I_s U_{\rm oc}(E_s) = R I_s^2 + P_b(\omega, P_m), \tag{2.14}$$

or, as polynomial in I_s,

$$R I_s^2 - U_{\rm oc} I_s + P_b(\omega, P_m) = 0, \tag{2.15}$$

where R is the internal resistance which, for simplicity, may be assumed to be constant. Current I_s is solved from the quadratic relation (2.15):

$$I_s = \frac{U_{\rm oc}(E_s) - \sqrt{U_{\rm oc}^2(E_s) - 4R P_b(\omega, P_m)}}{2R}, \tag{2.16}$$

where P_m is limited from above such that $U_{\rm oc}^2 \geq 4R P_b(\omega, P_m)$ or $U_t \geq U_{\rm oc}/2$. This bound is the maximum amount of power that can be extracted from the battery and corresponds to the case where the internal resistance R equals the resistance over the terminals, when $U_t = U_{\rm oc}/2$. If P_m is too large, i.e., $P_b > \frac{U_{\rm oc}^2}{4R}$, there is no (real) solution for (2.14). Relation (2.14) is represented in graphical form in Fig. 2.13. The model for a lead acid battery can be developed in the same way.

To protect the battery from under- or overcharging, the battery energy levels are constrained:

$$E_s(t) - \overline{E}_s \leq 0, \tag{2.17}$$

$$\underline{E}_s - E_s(t) \leq 0, \tag{2.18}$$

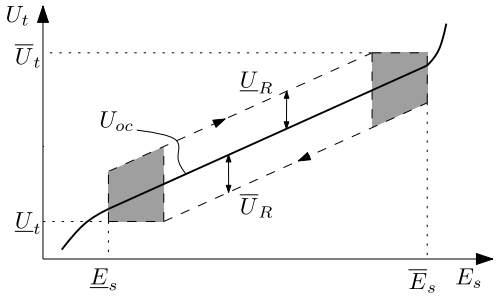

Fig. 2.14 Mixed constraints on battery state-of-energy and voltage. Variables $\underline{U}_R$ and $\overline{U}_R$ are the voltage drops over the resistor due to the maximal and minimal power at the terminals. The voltage bounds on U_t lead to combined input (power) and state (SOE) constraints in the neighborhood of $(\underline{E}_s, \underline{U}_t)$ and $(\overline{E}_s, \overline{U}_t)$

here, $\overline{E}_s < E_c$ is the maximum allowable state-of-energy of the storage device which is lower than the maximum capacity $\underline{E}_s > 0$ is the minimum one. The allowable range for E_s lies strictly inside the physical possible range for E_s, aiming to reduce wear of the battery, which is largest near the boundaries of the physical range. Equations (2.17) and (2.18) are "pure" state constraints meaning that they are a function of the state only. Any of the variables P_s, P_b, or P_m can be used as independent variable such that the state constraints (2.17) and (2.18) are of first order, meaning that the first time derivative of the constraints (2.17) and (2.18) contains the control explicitly. It may also be necessary to use a combination of P_s and E_s to express constraints on the voltage level, so-called mixed state/input constraints. Those mixed constraints are more difficult to handle than isolated input and state constraints. See Fig. 2.14 for an example.

2.3.3.2 "Fitted" Battery Model

One of the most straightforward ways to develop a simplified battery model is to assume a certain loss for charging, proportional to charging power squared. Because the current corresponding to a certain power will depend on voltage, we also need to access voltage. However, Li-ion batteries as well as, but to a lesser degree, lead-acid batteries have a relatively weak relation between charge state and voltage. It may, therefore, suffice to neglect this relation if the parameters of the relation are fitted on a restricted interval of operating conditions.

Looking at battery model (2.14), we can also write this as

$$P_s = P_b + \beta_2 P_s^2, \tag{2.19}$$

with $\beta_2 = R/U_{\text{oc}}^2 > 0$, where β_2 may depend on R and U_{oc} or may be considered as a constant fitted to measured data corresponding to the interval of interest for the

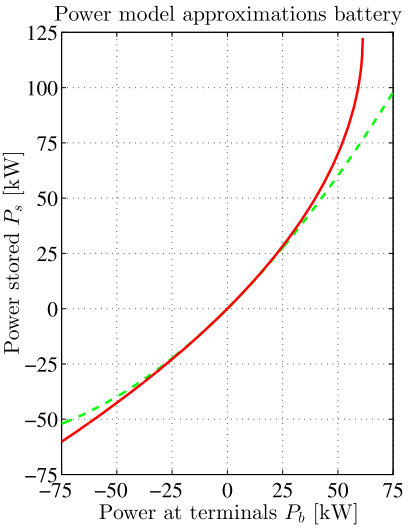

Fig. 2.15 Battery power stored versus battery power at the terminals for two different approximating functions, (2.19) (*red* and *solid*) and (2.21) (*green* and *dashed*). Note that both approximations will only agree in a restricted interval around $P_b = 0$, but given the size of the electric machine (the 44 [kW] one) this is precisely the interval of interest

Table 2.1 Hybrid electric delivery truck model parameters; the electric machine drag power is set to 0, but it may be assumed that the power request P_r absorbs this power

Name	Description	Value	Unit
$\overline{E}_s$	Upper capacity bound	4.08	MJ
$\underline{E}_s$	Lower capacity bound	1.80	MJ
$\max_\omega \overline{P}_p$	Maximum combustion engine power	127.7	kW
$\max_\omega \overline{P}_m$	Maximum electric machine power	44.1	kW
R	Battery internal resistance	0.32	Ω
U_0	Discharged battery voltage	280	V
ϕ	Voltage increase factor	21	V/MJ
$\gamma_{m,0}$	Drag electric machine	0	kW
$\gamma^+_{m,1}$	Electric to mechanical cost	1.1200	–
$\gamma^+_{m,2}$	Electric to mechanical cost	0.1323	–
$\gamma^-_{m,1}$	Mechanical to electric cost	0.8800	–
$\gamma^-_{m,2}$	Mechanical to electric cost	0.2205	–
$\gamma_{p,0}$	Engine drag	0.1181	–
$\gamma_{p,1}$	Incremental fuel cost	3.20	–

retrieved or stored power P_s. Solving for P_s gives

$$P_s = \frac{1 - \sqrt{1 - 4\beta_2 P_b}}{2\beta_2}, \tag{2.20}$$

with again the bound $P_b \leq 1/4\beta_2$ corresponding to $P_s \leq 1/2\beta_2$ for a real solution.

The influence of temperature and state-of-energy of the battery on U_{oc} and R, and of possible differences in R between charging and discharging, are all combined

in the parameter β_2. This parameter could attain different values depending on the specific conditions for the battery. Those effects could be accounted for in the data used to make a parameter fit for β_2.

Relation (2.19) perfectly matches the graph in Fig. 2.13 for the nominal value of β_2 because it is exactly the same relation as (2.14). The only advantages of the "equivalent circuit" based model (2.14) compared to the "fitted" model (2.19) are that the former provides a physical interpretation for β_2, or changes in β_2, while the latter does not, and that there is no interpretation possible of P_s in terms of current and voltage for the latter model.

It is sometimes convenient to write the losses in terms of P_b, so

$$P_s = \beta_1 P_b + \beta_2 P_b^2, \tag{2.21}$$

with $\beta_1 \approx 1$. This is a different approximating function, which will require a different value for β_1 and β_2 to generate an acceptable fit. The relation also does not provide an upper bound for P_b, any value will do.

In a well designed HEV, the interval of P_b of interest normally allows one to use any of the relations (2.14), (2.19), or (2.21), because they are close to each other. Also, the bound on P_b from (2.14) or (2.19) will never be attained, being outside the range that can be covered with the electric machine, see the example in Fig. 2.15.

2.4 Drive Cycles

To validate if engines or complete vehicles meet emission standards several *test procedures* with associated *drive cycles*[1] are available. These cycles are also relevant to address the benefits of hybrid vehicles because they allow to assess CO_2-emissions and fuel economy. The cycles differ with respect to the vehicle type (light or heavy-duty), the main usage of the vehicle (urban, extra-urban, and highway), the regional homologation bodies (Europe, Japan, USA, and others), and distinguish between dynamic (transient) and static (individual operating points), and roller dynamometer (vehicle) and engine dynamometer (engine only) tests.

For passenger or light-duty vehicles the NEDC (New European Driving Cycle) (EEC 1970, pp. 67–73),[2] see Fig. 2.16, the JC 08 (the new Japanese Cycle), see

[1] Most cycles are available in digital form at http://www.epa.gov/nvfel/testing/dynamometer.htm.

[2] The velocity profile during acceleration and deceleration phases for the NEDC is not explicitly given in directive 70/220/EEC (EEC 1970) but is the result of specified acceleration levels and declutch events. Note that there are data sources which do provide a velocity profile, but at least one prominent source does provide a slightly incorrect profile for the urban (ECE) subcycle. In any case, the official specification of the operating cycle contains a handful of obvious errors. Directive 70/220/EEC has been repealed with effect from January 2, 2013 and was replaced by Regulation 83 of the UN/ECE body (UN/ECE 2012). This regulation contains a copy of the same NEDC cycle as in 70/220/EEC, including most of the errors.

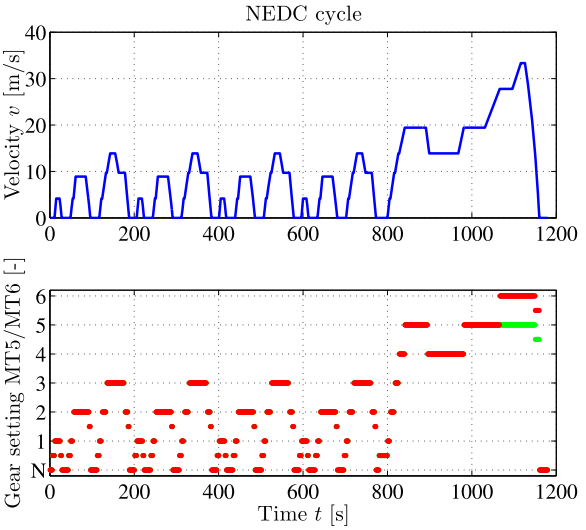

Fig. 2.16 New European Driving Cycle (NEDC) showing velocity and two profiles for manual transmissions with a different number of gears plotted on top of each other. The "N" gear setting means the gearbox is in neutral and the clutch is engaged, the half gear settings indicate that the next higher gear is engaged but the clutch is disengaged. The 11.028 [km] long cycle consists of a four times repeated urban (ECE) subcycle with low velocities taking 195 [s] each and a single extra-urban (EUDC) subcycle with higher velocities starting from $t = 780$ [s] and taking 400 [s] for a complete cycle length of 1180 [s]. The maximum speed is 120 [km/h], the average speed is 33.6 [km/h] including stops and 44.8 [km/h] excluding stops. There is a margin defined around the nominal velocity profile of ± 2 [km/h] and ± 1 [s] which can be exploited to get an up to ≈ 2 % better fuel economy. The declared value for CO_2 emissions may be understated by up to 4 % compared to the measured value (EEC 1980, p. 9). The test cycle is supposed to be started with a cold engine. Because fuel maps of engines are measured at equilibrium conditions, a computation with fuel maps will not exactly reproduce the measured NEDC fuel usage but will give a lower number

Fig. 2.17, and the FTP 75 (Federal Test Procedure) city cycle (CFR40-20 2012b, Appendix I(a) to part 86, pp. 543–546),[3] see Fig. 2.18, are relevant.

For future work, the WLTC (World-wide Light-duty Test Cycle) drive cycle may be relevant. This cycle is currently developed for future use (from 2017 on or later) and should simplify homologation (type-approval) by using a single test procedure and test cycle that is valid world-wide. Already several variants are proposed for the test cycle "to accommodate regional differences", that differ mainly in the maximum speed and acceleration levels.

[3]The cycle specified here is the so-called UDDS (EPA Urban Dynamometer Driving Schedule for Light-Duty Vehicles and Light-Duty Trucks). The FTP schedule is specified in (FR40-19 2012a, 86.135-12) and is composed of the first 1369 [s] of the 1372 [s] long UDDS, followed by the first 505 [s] of the UDDS to get a hot start phase.

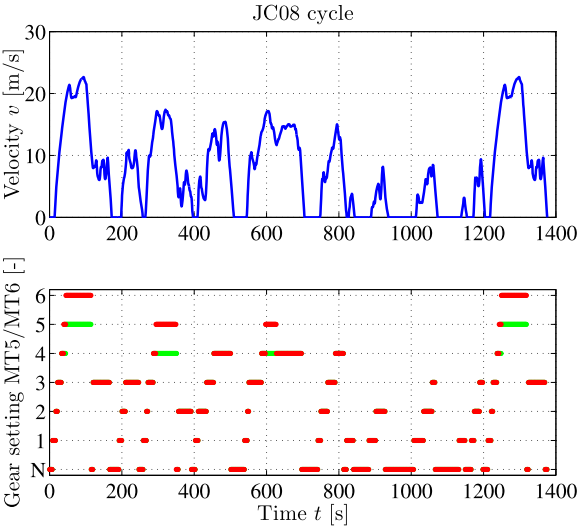

Fig. 2.17 Japanese Cycle (JC 08) showing velocity and two profiles for manual transmissions with a different number of gears plotted on top of each other. The "N" gear setting means the gearbox is in neutral and the clutch is engaged. The cycle represents congested urban traffic. The measurements start after $t = 172$ [s], the part up to $t = 172$ [s] is repeated at the end, while the 8.16 [km] long measurement cycle takes 1204 [s] to complete. The maximum speed is 81.6 [km/h], the average speed is 24.4 [km/h] including stops and 34.7 [km/h] excluding stops. The cycle is performed twice, once with a cold and once with a hot engine

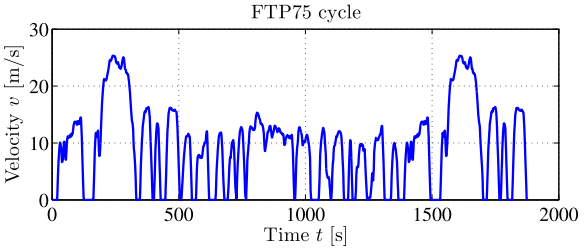

Fig. 2.18 Federal Test Procedure (FTP 75) velocity points. The 17.77 [km] long FTP 75 cycle consists of three phases, where the first and the last one, taking 505 [s], are identical while the middle one takes 864 [s] for a total cycle length of 1874 [s]. The maximum speed is 91.2 [km/h], the average speed is 34.1 [km/h] including stops and 42.2 [km/h] excluding stops. There is a margin defined around the nominal velocity profile of ± 2 [mi/h] and ± 1 [s] (CFR40-20 2012b, p. 546), but the practice of smoothing the speed variations is discouraged. The cycle is started with a cold engine

For heavy-duty vehicles several drive cycles are relevant, e.g., the HD-UDDS (Heavy-Duty Urban Dynamometer Driving Schedule) (CFR40-20 2012b, Appendix I(d) to part 86, pp. 566–573), see Fig. 2.19. Because the characteristics of driving patterns depend on usage, there is a difference between cycles targeted at urban

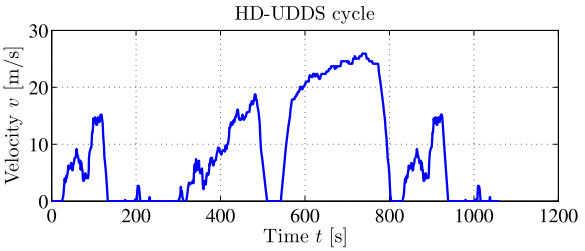

Fig. 2.19 Heavy-duty Urban Dynamometer Driving Schedule (HD-UDDS) speed points. The 8.9 [km] long cycle has two subcycles, one at the beginning and one at the end, that are identical, and that are combined with another subcycle for a total cycle duration of 1060 [s]. The maximum speed is 93.3 [km/h], the average speed is 30.3 [km/h] including stops and 45.4 [km/h] excluding stops, so stops are manifest in the HD-UDDS cycle, approximately one third of the time the vehicle is standing still and the engine is idling

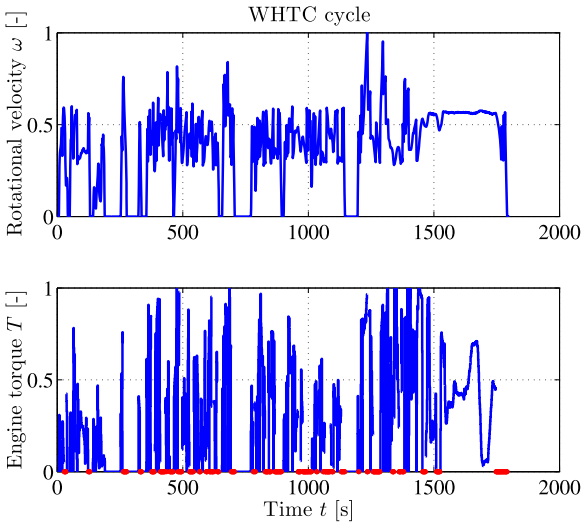

Fig. 2.20 World Harmonised Transient Cycle (WHTC) engine test cycle. Speed and torque are given as a fraction of the working range with the *red torque points* representing closed rack motoring. There are three phases, an urban phase of 900 [s], an extra urban phase of 480 [s], and a highway phase of 420 [s], so the total cycle takes 1800 [s] to complete. The average torque fraction is 0.307 and the average power fraction is 0.201, excluding the closed rack motoring points and assuming idle speed to be 1/3 of maximum speed. This cycle is intended to reduce the homologation effort by engine manufacturers

usage and highway usage for heavy-duty trucks. The vehicle and engine used to perform the cycle need to be characteristic for the class of usage considered.

Some *engine cycles* are available that test only the engine on an engine dynamometer, not the complete vehicle on a roller dynamometer. Engine test cycles are, e.g., the World Harmonised Transient Cycle (WHTC) (UN/ECE 2010,

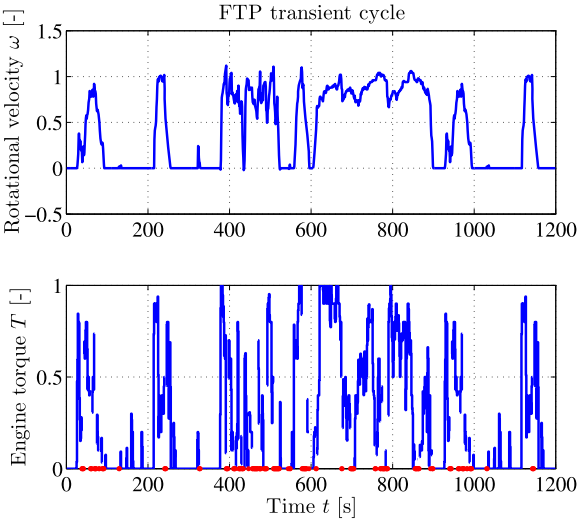

Fig. 2.21 FTP (Federal Test Procedure) Heavy Duty Diesel Transient Cycle (HDDTC). Normalized speed and torque are given as a fraction of the working range, the *red torque points* represent closed rack motoring, the engine torque corresponding to this condition depends on the engine drag torque. Note that speed overrun (speed higher than rated speed, here a fraction >1) and speed underrun (speed lower than curb idle speed, here a fraction <0) are specified in the cycle and need to be unnormalized, see (CFR40-20 2012b, Part 86.1333). The cycle consists of four subcycles, where the first is identical to the last, the cycle takes 1199 [s] to complete and is performed twice, once with a cold and once with a hot engine. The average torque fraction is 0.283 and the average power fraction is 0.229, excluding the closed rack motoring points and assuming idle speed to be $1/3$ of rated speed

pp. L229/78–L229/89), sometimes called the World Heavy-duty Transient Cycle, and the FTP diesel transient cycle (CFR40-20 2012b, Appendix I(f)(2) to part 86, pp. 585–593). These cycles are depicted in Figs. 2.20–2.21. There are also stationary engine cycles, where the engine is run on a set of specific operating points. An example is the World Harmonised Stationary Cycle (WHSC) (UN/ECE 2010, p. L229/22).

Driving cycles are mostly characterized by a prescribed velocity and gear setting profile as a function of time. This is useful for driving the cycles. For simulations without a driver model, power at the wheel, or engine torque and speed are needed. From velocity and gear profiles it is possible to derive the desired torque and engine speed profile when the total gear ratios, mass, and air and tire resistance characteristics are known, see Eq. (1.1). The resistance characteristics, or road load data, are mostly obtained from preliminary roll-out tests also defined in the test procedures, but for this, a specific vehicle type needs to be defined.

For engine cycles the engine torque and speed, so also engine power, are prescribed as a function of time as can be seen from Figs. 2.20–2.21. For these cycles, torque and speed are scaled towards the performance envelope of the engine under

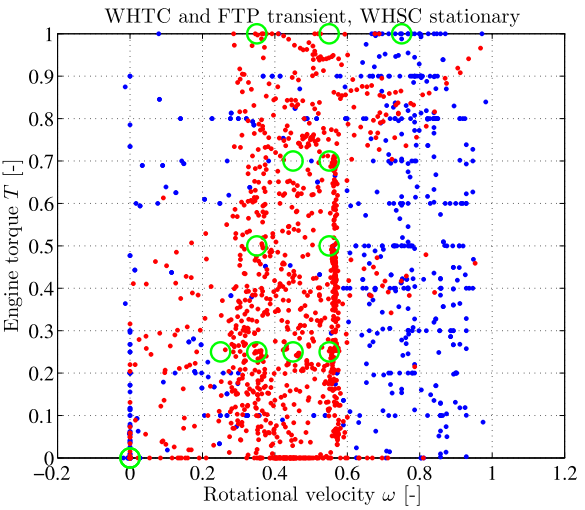

Fig. 2.22 Comparison of the WHTC (*red points*), WHSC (*green circles*), and the FTP transient (*blue points*, speed overrun corrected to match normalized speed—maximum instead of rated—of other cycles) engine cycles. The data illustrate rather marked differences between those cycles, which will be reflected in fuel economy potential for hybrid systems and their control laws

test. Cycles may be rather different as can be seen from a comparison of the WHTC, WHSC, and FTP transient engine cycles in Fig. 2.22.

2.5 Bibliographical Notes

Several books are available on the subject of (hybrid) vehicles and some effort has been made to introduce or develop (component) models, namely Miller (2004), Guzzella and Sciarretta (2005), Ehsani et al. (2010), Pistoia (2010), Husain (2011), German (2011).

One of the earlier papers on the modeling of hybrid vehicles stems from 1995 Bailey and Powell (1995). An overview of modeling methods is given in Chan et al. (2010). A modeling approach rather similar to the one taken here is presented in He and Hodgson (2002) while a more detailed model is found in Syed et al. (2006).

Efforts specifically targeted at model development for batteries are Johnson (2002), Tremblay et al. (2007), Szumanowaski and Chang (2008). Most of those works use experimental data and try to fit a model through their data, sometimes using physically inspired basis functions. The temperature influence for batteries is discussed in Pesaran (2002). For super capacitors, a modeling approach is presented in Buller et al. (2002).

The inverter, the power electronics needed to couple battery pack and electric machine, is analyzed in Mapelli et al. (2010), while the electric machine losses are analyzed in Williamson et al. (2007).

One of the well known tools for modeling (hybrid) drivetrains is the simulation package “ADVISOR”, see Markel et al. (2002), which mainly focused on reliable prediction of behavior using simulation, for which it has been used frequently, see,

e.g., Johnson et al. (2000), Gao et al. (2007). However, there is no emphasis on simplified analytical models for online control purposes. Alternative tools are described in Butler et al. (1999), Lin et al. (2001), Onoda and Emadi (2004). Specialized approaches, like gyrator theory, are used in Routex et al. (2000).

Models are also introduced when a specific control strategy for hybrid systems is discussed. Examples are in Kao and Moskwa (1995), Shimizu et al. (1997), Tate and Boyd (2000), Lin et al. (2003), West et al. (2003), Albert et al. (2004), Sciarretta et al. (2004), Barsali et al. (2004), Lukic and Emadi (2004), Delprat et al. (2004), Tyrus et al. (2004), Plett (2004), Baisden and Emadi (2004). The paper by Tate and Boyd (2000) uses a particularly simple model.

Type-approval drive cycles are determined by regulatory bodies or by committees trying to establish the common denominator between all participants. For an example see the documents of the ECE-GRPE Working Party on Pollution and Energy (ECE/Trans/WP.29/GRPE).[4]

References

Albert IJ, Kahrimanovic E, Emadi A (2004) Diesel sport utility vehicles with hybrid electric drive trains. IEEE Trans Veh Technol 53(4):1247–1256

Bailey KE, Powell BK (1995) A hybrid electric vehicle powertrain dynamic model. In: Proc American control conf, Seattle, WA, USA, pp 1677–1682

Baisden AC, Emadi A (2004) ADVISOR-based model of a battery and an ultra-capacitor energy source for hybrid electric vehicles. IEEE Trans Veh Technol 53(1):199–205

Barsali S, Miulli C, Possenti A (2004) A control strategy to minimize fuel consumption of series hybrid electric vehicles. IEEE Trans Energy Convers 19(1):187–195

Buller S, Karden E, Kok D, De Doncker RW (2002) Modeling the dynamic behavior of supercapacitors using impedance spectroscopy. IEEE Trans Ind Appl 38(6):1622–1626

Butler KL, Ehsani M, Kamath P (1999) A Matlab-based modeling and simulation package for electric and hybrid electric vehicle design. IEEE Trans Veh Technol 48(6):1770–1778

CFR40-19 (2012a) Code of federal regulations title 40—protection of environment. http://www.gpo.gov/fdsys/pkg/CFR-2012-title40-vol19/pdf/CFR-2012-title40-vol19.pdf

CFR40-20 (2012b) Code of federal regulations title 40—protection of environment. http://www.gpo.gov/fdsys/pkg/CFR-2012-title40-vol20/pdf/CFR-2012-title40-vol20.pdf

Chan CC, Bouscayrol A, Chen K (2010) Electric, hybrid, and fuel-cell vehicles: architecture and modelling. IEEE Trans Veh Technol 59(2):589–598

Delprat S, Lauber J, Guerra TM, Rimaux J (2004) Control of a parallel hybrid powertrain: optimal control. IEEE Trans Veh Technol 53(3):872–881

EEC (1970) Councel directive of 20 March 1970 on the approximation of the laws of the member states on measures to be taken against air pollution by emissions from motor vehicles (70/220/EEC) plus amendments. Consolidated text of Jan 1, 2007. http://eur-lex.europa.eu/LexUriServ/LexUriServ.do?uri=CONSLEG:1970L0220:20070101:EN:PDF

EEC (1980) Councel directive of 16 December 1980 relating to the carbon dioxide emissions and the fuel consumption of motor vehicles (80/1268/EEC) plus amendments. Consolidated text of Feb 19, 2004. http://eur-lex.europa.eu/LexUriServ/LexUriServ.do?uri=CONSLEG:1980L1268:20040219:EN:PDF

[4]See http://unece.org/trans/main/wp29/wp29wgs/wp29grpe/grpedoc_2013.html.

Ehsani M, Gao Y, Emadi A (2010) Modern electric, hybrid electric, and fuel cell vehicles: fundamentals, theory and design, 2nd edn. CRC Press, Boca Raton
Gao DW, Mi C, Emadi A (2007) Modeling and simulation of electric and hybrid vehicles. Proc IEEE 95(4):729–745
German JM (2011) Hybrid-powered vehicles, 2nd edn. SAE, Warrendale
Guzzella L, Sciarretta A (2005) Vehicle propulsion systems. Springer, Berlin
He X, Hodgson JW (2002) Modeling and simulation for hybrid electric vehicles—part I. IEEE Trans Intell Transp Syst 3(4):235–243
Husain I (2011) Electric and hybrid vehicles: design fundamentals, 2nd edn. CRC Press, Boca Raton
Johnson VH (2002) Battery performance models in ADVISOR. J Power Sources 110:321–329
Johnson VH, Wipke KB, Rausen DJ (2000) HEV control strategy for real-time optimization of fuel economy and emissions. In: 2000 future car congress proc, Arlington, VA. SAE paper 2000-01-1543
Kao M, Moskwa JJ (1995) Turbocharged diesel engine modeling for nonlinear engine control and state estimation. J Dyn Syst Meas Control 117(1):20–30
Lin CC, Filipi Z, Wang Y, Louca L, Peng H, Assanis D, Stein J (2001) Integrated, feed-forward hybrid electric vehicle simulation in SIMULINK and its use for power management studies. In: Advanced hybrid vehicle powertrains (SP-1607), Detroit, MI. SAE paper 2001-01-1334
Lin CC, Peng H, Grizzle JW, Kang JM (2003) Power management strategy for a parallel hybrid electric truck. IEEE Trans Control Syst Technol 11(6):839–849
Lukic SM, Emadi A (2004) Effects of drivetrain hybridization on fuel economy and dynamic performance of parallel hybrid electric vehicles. IEEE Trans Veh Technol 53(2):385–389
Mapelli FL, Tarsitano D, Mauri M (2010) Plug-in hybrid electric vehicle: modeling, prototype realization, and inverter losses reduction analysis. IEEE Trans Intell Transp Syst 57(2):598–607
Markel T, Brooker A, Hendricks T, Johnson V, Kelly K, Kramer B, O'Keefe M, Sprik S, Wipke K (2002) ADVISOR: a systems analysis tool for advanced vehicle modeling. J Power Sources 110:255–266
Miller JM (2004) Propulsion systems for hybrid vehicles. IEE power & energy series, vol 45. IEE, London
Onoda S, Emadi A (2004) PSIM-based modeling of automotive power systems: conventional, electric, and hybrid electric vehicles. IEEE Trans Veh Technol 53(2):390–400
Pesaran AA (2002) Battery thermal models for hybrid vehicle simulations. J Power Sources 110:377–382
Pistoia G (ed) (2010) Electric and hybrid vehicles: power sources, models, infrastructure and the market. Elsevier, Amsterdam
Plett GL (2004) High-performance battery-pack power estimation using a dynamic cell model. IEEE Trans Veh Technol 53(5):1586–1593
Pop V, Bergveld HJ, Danilov D, Regtien PPL, Notten PHL (2008) Battery management systems. Philips research book series, vol 9. Springer, New York
Routex JY, Gay-Desharnais S, Ehsani M (2000) Modeling of hybrid electric vehicles using gyrator theory: application to design. In: Proc IEEE veh technol conf, vol 5. IEEE, New York, pp 2090–2094
Sciarretta A, Back M, Guzzella L (2004) Optimal control of parallel hybrid electric vehicles. IEEE Trans Control Syst Technol 12(3):352–363
Shimizu H, Harada J, Bland C, Kawakami K, Chan L (1997) Advanced concepts in electric vehicle design. IEEE Trans Ind Electron 44(1):14–18
Syed FU, Kuang ML, Czubay J, Ying H (2006) Derivation and experimental validation of a power-split hybrid electric vehicle model. IEEE Trans Veh Technol 55(6):1731–1747
Szumanowaski A, Chang Y (2008) Battery management system based on battery nonlinear dynamics modeling. IEEE Trans Veh Technol 57(3):1425–1432
Tate ED, Boyd SP (2000) Finding ultimate limits of performance for hybrid electric vehicles. In: Hybrid electric vehicles (SP-1560), Costa Mesa, CA. SAE paper 2000-01-3099

Tremblay O, Dessaint LA, Dekkiche AI (2007) A generic battery model for the dynamic simulation of hybrid electric vehicles. In: Proc IEEE veh power and propul conf. IEEE, New York, pp 284–289

Tyrus JM, Long RM, Kramskaya M, Fertman Y, Emadi A (2004) Hybrid electric sport utility vehicles. IEEE Trans Veh Technol 53(5):1607–1622

UN/ECE (2010) Regulation No 49 of the economic commission for Europe of the United Nations (UN/ECE)—uniform provisions concerning the measures to be taken against the emission of gaseous and particulate pollutants from compression-ignition engines for use in vehicles, and the emission of gaseous pollutants from positive-ignition engines fuelled with natural gas or liquefied petroleum gas for use in vehicles. http://eur-lex.europa.eu/LexUriServ/LexUriServ.do?uri=OJ:L:2010:229:0001:0138:EN:PDF

UN/ECE (2012) Regulation No 83 of the Economic Commission for Europe of the United Nations (UN/ECE)—uniform provisions concerning the approval of vehicles with regard to the emission of pollutants according to engine fuel requirements. http://eur-lex.europa.eu/LexUriServ/LexUriServ.do?uri=OJ:L:2012:042:0001:0207:EN:PDF

West MJ, Bingham CM, Schofield N (2003) Predictive control for energy management in all/more electric vehicles with multiple energy storage units. In: Proc IEEE internat electric machines and drives conf, vol 1. IEEE, New York, pp 222–228

Williamson SS, Emadi A, Rajashekara K (2007) Comprehensive efficiency modeling of electric traction motor drives for hybrid electric vehicle propulsion applications. IEEE Trans Veh Technol 56(4):1561–1572

Chapter 3
Problem Definition

3.1 Formal Problem Statement

Hybrid electric vehicles incorporate at least two energy sources (i.e., fuel tank and battery pack) to satisfy the power request for vehicle propulsion. This means that freedom exists when to use which energy source. An energy management strategy (EMS) makes this decision according to an advanced control algorithm. Today, many solution concepts exist and in this work the method of optimal control will be applied. It will be shown that the control objective can be written as a mathematical optimization problem of the form

$$\mathscr{P}_0 := \begin{cases} \min_{u \in \mathscr{U}} & J(t, x, u, r) \\ \text{subject to:} & \dot{x}(t) = f(t, x, u, r), \\ & g(x, u) = 0, \\ & h(x, u) \leq 0, \end{cases} \tag{3.1}$$

here, u is the control variable, $\mathscr{U}$ the set of admissible controls, J the performance criterion (also called performance index, control objective or cost function), t the time index, x the state variable, r the extraneous input, f the dynamical state equations, g the equality constraints and h the inequality constraints. These elements will be further developed in the next sections.

3.2 Performance Criterion

Optimal control of an HEV means that a control law is searched which achieves best performance but also respects the dynamics of the system. It is clear that the term "best" is rather subjective and differs for each driver. Therefore, it is common practice to define optimality according to a performance criterion or numerical index. This criterion denotes how well the vehicle satisfies a particular control objective.

B. de Jager et al., *Optimal Control of Hybrid Vehicles*, Advances in Industrial Control,
DOI 10.1007/978-1-4471-5076-3_3,

Nonetheless, one should always keep in mind that the real performance depends on suitability of the chosen criterion.

In this work, the focus is on minimizing the overall energy consumption of the vehicle. A performance index J_f is constructed which calculates the total energy demand when traveling an arbitrary drive cycle with length t_f:

$$J_f = \int_{t_0}^{t_f} P_f(t, x, u, r)\,\mathrm{d}t, \tag{3.2}$$

where P_f denotes the fuel power consumption of the ICE (i.e., the prime mover). The mechanical ICE power demand can be calculated from its momentary fuel mass flow $\dot{m}_f$, see Sect. 2.2. There it was assumed that P_f and $\dot{m}_f$ are proportional to each other and a weighting factor w_1 is introduced representing the *lower heating value* h of fuel:

$$P_f = h\,\dot{m}_f = w_1 \dot{m}_f. \tag{3.3}$$

Typical values for w_1 can be found in Fig. 1.1 (e.g., for gasoline and diesel).

The combustion of fuel is closely related to CO_2 emissions but also other exhaust gases are produced. From an emission point of view, it can be attractive to define an alternative criterion and include all engine-out emissions using a weighted sum approach:

$$J = \int_{t_0}^{t_f} (w_1 \dot{m}_f + w_2 \mathrm{CO}_2 + w_3 \mathrm{CO} + w_4 \mathrm{NO}_x + w_5 \mathrm{HC} + w_6 \mathrm{PM})\,\mathrm{d}t, \tag{3.4}$$

where w_i are appropriate weighting factors for the individual emissions: carbon dioxide (CO_2), carbon monoxide (CO), nitrogen (di-)oxide (NO_x), hydro carbon (HC) and particulate matter (PM). Modern vehicles are equipped with an exhaust gas aftertreatment system or EAS (Engine Aftertreatment System). The EAS reduces the engine-out emissions by means of filters and catalytic converters. The associated chemical reactions are temperature dependent and their reaction rate is highly nonlinear. Optimizing engine-out emissions is important for maximizing the performance of the EAS, but one should be careful to assume that this automatically optimizes tailpipe-out emissions. To that end, an appropriate performance criterion should be formulated including the dynamics of both ICE and EAS. This is beyond the scope of this book, but the interested reader is referred to, e.g., Kessels et al. (2010) or Serrao et al. (2011) for further details and examples.

3.3 Vehicle Description

An HEV can be considered as a dynamical system with state equation:

$$\dot{x}(t) = f(t, x, u, r). \tag{3.5}$$

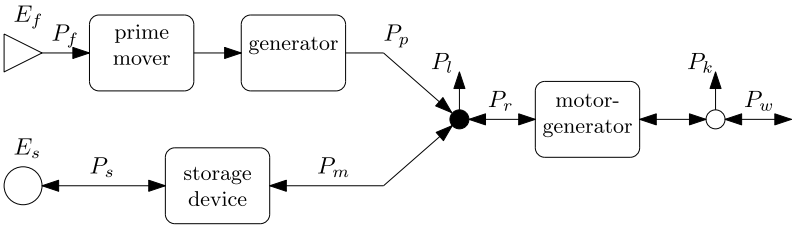

Fig. 3.1 Topology of a series HEV. The prime mover is connected to the generator and fuel is first converted into electric power. The motor-generator provides the propulsion power to the driveline, where electric power translates back into mechanical power. The storage device can supply/retrieve the electric power mismatch between generator and motor/generator

Without loss of generalization, hybrid vehicles with a series and parallel powersplit topology (S-HEV and P-HEV, respectively) can be described by this state equation. This will be demonstrated below.

3.3.1 Series Hybrid Topology

The vehicle topology of an S-HEV is shown in Fig. 3.1. The mechanical power from the prime mover (i.e., ICE) is directly converted into electric power P_p by means of a generator. Next, this electric power can be used for propulsion power P_r towards the driveline. Also auxiliaries with power request P_l can be connected to the (high voltage) electric powernet. In case there is a mismatch between supply P_p and demand P_r plus P_l, there is a power exchange P_m with the battery. Altogether, the electric powernet introduces the following power balance:

$$P_p + P_m = P_r + P_l. \tag{3.6}$$

Similar to Chap. 2, it is assumed that all power converters (i.e., ICE, generator and motor/generator) can be described by a (quasi) static equation to define their conversion losses. The battery model is composed of an energy storage buffer E_s in combination with energy losses for charging/discharging, see Sect. 2.3.3. The battery energy level is described by

$$E_s(t) = E_s(t_0) + \int_{t_0}^{t} -P_s(\tau)\,\mathrm{d}\tau. \tag{3.7}$$

3.3.2 Parallel Hybrid Topology

An overview of a P-HEV is shown in Fig. 3.2. In this vehicle configuration, the mechanical powersplit enables that both the ICE as well as the motor/generator can

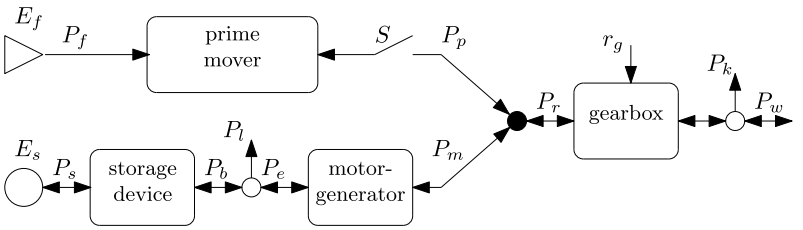

Fig. 3.2 Topology of a parallel HEV. A mechanical powersplit is present, such that the prime mover and the motor-generator can both give tractive force to the driveline. The motor-generator can also recapture mechanical power from the powersplit and store the electric power in the storage device

give tractive power to the wheels:

$$P_p + P_m = P_r. \tag{3.8}$$

Typical for the S-HEV is that the ICE speed is disconnected from the wheel speed. The P-HEV, however, relates the engine speed to the wheel speed using a final drive, a transmission and clutch (denoted by switch S in Fig. 3.2). The motor/generator is rigidly connected to the crankshaft of the ICE when the clutch is closed. This machine operates similar to the motor/generator in the S-HEV and can operate in two modes: motor mode ($P_m \geq 0$) and generator mode ($P_m < 0$).

The electric powernet connects the motor/generator to the battery (and possible other electric auxiliaries with power demand P_l). No losses are assumed in the wiring harness. The battery model is similar to the S-HEV. Energy losses appear during charging ($P_b < 0$) and discharging ($P_b \geq 0$) and an integrator keeps track of the net stored energy in the battery, see (3.7).

3.3.3 Vehicle State Equation

Returning back to the optimization problem $\mathscr{P}_0$, the S-HEV and P-HEV incorporate only one state variable $x := E_s$ and the state equation f follows from (3.7):

$$\dot{x} = -P_s. \tag{3.9}$$

For didactic reasons, it is desirable to select the control input equal to the net battery power, so $u := P_s$. In practical situations, however, P_s is preferably not a decision variable because it is not directly measurable from the battery. It is obvious that P_s eventually results from the selected motor/generator power P_m. Therefore, final vehicle implementation typically selects the motor/generator power as controlled input variable to charge or discharge the battery. From a control perspective, there are no strict reasons to decide for P_s or P_m.

Finally, the requested driving power $P_r(t)$ and associated speed ω can be seen as an extraneous input and follows from the drive cycle under consideration. The power

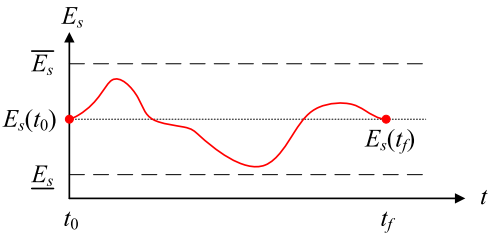

Fig. 3.3 Visualization of arbitrary state trajectory with end-point constraint (to achieve charge-sustaining EMS, i.e., $\Delta E_s = 0$). The maximum and minimum battery energy are denoted by $\overline{E}_s$ and $\underline{E}_s$, respectively

request of the driveline P_r is calculated with the vehicle model from Sect. 1.1.2. Given an arbitrary speed profile, this model calculates the mechanical power request P_r according to

$$P_r = T_r \omega, \tag{3.10}$$

with driveline torque T_r and speed ω.

3.4 State Constraints

The general control objective is to minimize the energy consumption of the vehicle. In the previous section, the performance criterion focused on minimizing the fuel consumption (and possibly other emissions) of the ICE. Since the stored energy in the battery is neglected in the performance criterion, there is a serious risk that the battery will be depleted at the end of the drive cycle.

Up to now, the EMS considers energy stored in the battery at the start of the drive cycle as energy available free of charge. Additional measures are needed to create a so-called *charge sustaining* EMS where the energy in the battery remains at a predefined level at the end of the drive cycle. This is achieved by including an end-point constraint on state x in the optimization problem $\mathscr{P}_0$, which expresses a desired energy level E_s of the battery at time t_f. In principle any reference value can be selected for the final energy level, but it is convenient to select it equal to the initial value at t_0, see Fig. 3.3. When comparing results from different EMS approaches, this avoids compensation for the energy difference $\Delta E_s = E_s(t_f) - E_s(t_0)$ when this is nonzero.

$$E_s(t_f) = E_s(t_0) \quad \Leftrightarrow \quad g(x,u) = \int_{t_0}^{t_f} P_s(t)\,\mathrm{d}t = 0. \tag{3.11}$$

Remark when considering a plug-in HEV, the normal situation will be that $\Delta E_s < 0$. These vehicles charge their battery from the grid and use this energy to lower the power request from the primary mover during driving.

An aspect that did not receive any attention so far is the maximum storage capacity of the battery. In situations where the HEV is equipped with a (relative) small battery pack, there is a possibility that the EMS will hit upper or lower bounds on

the battery energy level E_s. For these situations, the optimization problem $\mathscr{P}_0$ will also include inequality constraints that represent the maximum and minimum energy level, i.e., $\overline{E}_s$ and $\underline{E}_s$, respectively. These state constraints are visualized in Fig. 3.3 and in $\mathscr{P}_0$ they are denoted by $h(x)$:

$$\underline{E}_s \leq E_s(t) \leq \overline{E}_s \quad \Rightarrow \quad h(x) = \begin{bmatrix} E_s(t) - \overline{E}_s \\ -E_s(t) + \underline{E}_s \end{bmatrix} \leq \begin{bmatrix} 0 \\ 0 \end{bmatrix}. \tag{3.12}$$

3.5 Input Constraints

Besides constraints on the state variable x, also input constraints are present on the control input u. This guarantees that the maximum powerflow through components remains bounded. In practical situations the operating range of the components is always limited, so bounds have to be set on power from the ICE and the generator. This is done using the following constraints:

$$\underline{P}_p(\omega) \leq P_p \leq \overline{P}_p(\omega), \tag{3.13}$$

$$\underline{P}_m(\omega) \leq P_m \leq \overline{P}_m(\omega), \tag{3.14}$$

where $\underline{P}$ and $\overline{P}$ denote the minimum and maximum power limit, respectively. In $\mathscr{P}_0$ these constraints will be incorporated by restricting the set of admissible control inputs $\mathscr{U}$:

$$P_m \in \mathscr{U}(\omega, P_r), \tag{3.15}$$

with

$$\begin{aligned} \mathscr{U}(\omega, P_r) = \big[&\max\big(\underline{P}_m(\omega), -\overline{P}_p(\omega) + P_r\big), \\ &\min\big(\overline{P}_m(\omega), \max\big(\underline{P}_m(\omega), -\underline{P}_p(\omega) + P_r\big)\big)\big], \end{aligned} \tag{3.16}$$

the set of admissible controls where $P_l = 0$ is assumed. A feasible input trajectory is assumed such that there is always sufficient power available to match the power request, i.e., $P_r > \overline{P}_p + \overline{P}_m$ cannot occur and in case $P_r < \underline{P}_p + \underline{P}_m$ it is assumed that the service brakes can be applied to meet P_r while using $\underline{P}_m$.

3.6 Mixed State and Input Constraints

Sections 3.4 and 3.5 discussed pure state constraints on x and pure input constraints on u, respectively. In addition, also mixed constraints exist which consider the pair (x, u). This becomes apparent when considering the voltage U_t at the battery terminals. The internal voltage U_{oc} depends on state $x = E_s$ and when drawing current from the battery, a voltage drop occurs over the internal resistance R (see also

Fig. 2.9). In case the battery becomes at low state-of-charge, one should keep the discharge power limited, such that the minimum terminal voltage $\underline{U}_t$ will not be exceeded. Conversely, during charging one should avoid that overcharging does not take place and this can be done by respecting the maximum terminal voltage $\overline{U}_t$. These requirements lead to the following mixed state and input constraints:

$$\underline{U}_t \leq U_t(E_s, P_s) \leq \overline{U}_t \quad \Rightarrow \quad h(x,u) = \begin{bmatrix} U_t(E_s, P_s) - \overline{U}_t \\ -U_t(E_s, P_s) + \underline{U}_t \end{bmatrix} \leq \begin{bmatrix} 0 \\ 0 \end{bmatrix}. \tag{3.17}$$

3.7 Problem Definition Summary

In the preceding sections all elements of the optimization problem $\mathscr{P}_0$ have been described. The main results will be summarized here.

The first optimization problem $\mathscr{P}_1$ describes the control objective for an HEV with infinite battery storage capacity. This means that the inequality constraints from (3.12) vanish from the optimization problem:

$$\mathscr{P}_1 := \begin{cases} \min_{u \in \mathscr{U}} \ \int_{t_0}^{t_f} P_f(t, E_s, u, P_r, \omega)\, \mathrm{d}t, \\ \text{subject to: } \dot{E}_s = -P_s, \\ \qquad\qquad \int_{t_0}^{t_f} P_s(t)\, \mathrm{d}t = 0. \end{cases}$$

The second optimization problem $\mathscr{P}_2$ does include the storage limitations of the battery. This means that $\mathscr{P}_1$ is augmented with the constrains from (3.12):

$$\mathscr{P}_2 := \begin{cases} \min_{u \in \mathscr{U}} \ \int_{t_0}^{t_f} P_f(t, E_s, u, P_r, \omega)\, \mathrm{d}t, \\ \text{subject to: } \dot{E}_s = -P_s, \\ \qquad\qquad \int_{t_0}^{t_f} P_s(t)\, \mathrm{d}t = 0, \\ \qquad\qquad \begin{bmatrix} E_s(t) - \overline{E}_s \\ -E_s(t) + \underline{E}_s \end{bmatrix} \leq \begin{bmatrix} 0 \\ 0 \end{bmatrix}. \end{cases}$$

The third optimization problem $\mathscr{P}_3$ takes the storage limitations of the battery into account and simultaneously respects the minimum and maximum battery voltage. The mixed constraints from (3.17) are augmented to $\mathscr{P}_1$ giving the following problem definition:

$$\mathscr{P}_3 := \begin{cases} \min_{u \in \mathscr{U}} \ \int_{t_0}^{t_f} P_f(t, E_s, u, P_r, \omega)\, \mathrm{d}t, \\ \text{subject to: } \dot{E}_s = -P_s, \\ \qquad\qquad \int_{t_0}^{t_f} P_s(t)\, \mathrm{d}t = 0, \\ \qquad\qquad \begin{bmatrix} U_t(E_s, P_s) - \overline{U}_t \\ -U_t(E_s, P_s) + \underline{U}_t \end{bmatrix} \leq \begin{bmatrix} 0 \\ 0 \end{bmatrix}. \end{cases}$$

In the remainder of this book, these optimization problems will be frequently referred to. In all cases the selected vehicle configuration will be a P-HEV, unless stated otherwise. Furthermore, it is assumed that all powertrain components are properly scaled, such that the vehicle is always able to satisfy the driver's power request.

References

Kessels JTBA, Willems FPT, Schoot WJ, Van den Bosch PPJ (2010) Integrated energy & emission management for hybrid electric truck with SCR aftertreatment. In: Proc IEEE veh power and propul conf, IEEE, Lille, pp 1–6

Serrao L, Sciarretta A, Grondin O, Chasse A, Creff Y, di Domenico D, Pognant-Gros P, Querel C, Thibault L (2011) Open issues in supervisory control of hybrid electric vehicles: a unified approach using optimal control methods. In: Les rencontres scientifiques d'IFP energies nouvelles internat scient conf hybrid and electric vehicles, Rueil-Malmaison, France

Chapter 4
Analytical Solution Methods

4.1 Method of Lagrange Multipliers

This section presents first an illustrative example for (un)constrained optimization problems and introduces the method of Lagrange multipliers for solving these problems. Next, this method will also be applied to optimization problem $\mathscr{P}_1$ and an analytical EMS solution is derived.

4.1.1 Introduction to Method of Lagrange Multipliers

In Fig. 4.1 a quadratic function $y \in \mathbb{R}^2$ is visualized with analytical description:

$$y = (x_1 - a)^2 + (x_2 - b)^2 + c.$$

By setting the first differential equal to zero, one can find the minimum of this function:

$$\begin{cases} \frac{\partial y}{\partial x_1} = 2(x_1 - a) = 0 \\ \frac{\partial y}{\partial x_2} = 2(x_2 - b) = 0 \end{cases} \quad \Rightarrow \quad \begin{cases} x_1 = a, \\ x_2 = b. \end{cases}$$

Now consider once again the minimization of function y, but an extra constraint is added such that the optimal solution should appear outside or on a circle with radius d. This is visualized in Fig. 4.1 (right) and mathematically defined as follows:

$$\begin{aligned} &\min_{(x_1,x_2)\in\mathbb{R}^2} \quad y = (x_1 - a)^2 + (x_2 - b)^2 + c \\ &\text{subject to} \quad x_1^2 + x_2^2 \geq d^2. \end{aligned}$$

Owing to the merits of Joseph-Louis Lagrange (1736–1813), an elegant solution methods exist to solve these constrained optimization problems, see, e.g., Luen-

B. de Jager et al., *Optimal Control of Hybrid Vehicles*, Advances in Industrial Control,
DOI 10.1007/978-1-4471-5076-3_4, © Springer-Verlag London 2013

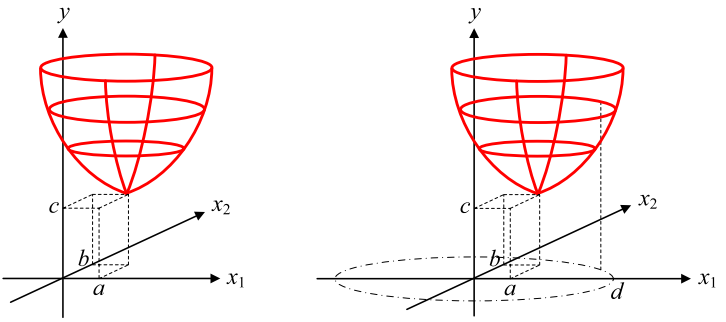

Fig. 4.1 Illustrative examples: unconstrained minimization of $y = (x_1 - a)^2 + (x_2 - b)^2 + c$ (*left*); constrained minimization of $y = (x_1 - a)^2 + (x_2 - b)^2 + c$ subject to $x_1^2 + x_2^2 \geq d^2$ (*right*)

berger (1969), Hull (2003). For each constraint a *Lagrange multiplier* λ is introduced. With this multiplier an equality constraint can be adjoined to the objective function and the *Lagrangian* L appears. This Lagrangian offers necessary conditions for the optimal solution, by setting its first differential equal to zero. These considerations are summarized as follows:

Let $J(x)$ be the objective function to be minimized and subject to constraints $g(x) = 0$:

$$\min_x J(x) \quad \text{subject to} \quad g(x) = 0.$$

Then the Lagrangian $L(x, \lambda)$ is defined as

$$L(x, \lambda) = J(x) + \lambda^\top g(x).$$

The necessary conditions for the optimal solution emerge by setting the first differential equal to zero:

$$\frac{\partial L(x, \lambda)}{\partial x} = 0,$$
$$\frac{\partial L(x, \lambda)}{\partial \lambda} = 0.$$

In the example above, the constraint $x_1^2 + x_2^2 \geq d^2$ needs to be rewritten such that the right-hand side becomes equal to zero: $x_1^2 + x_2^2 - d^2 = 0$. Next, the Lagrangian L is constructed:

$$L(x_1, x_2, \lambda) = (x_1 - a)^2 + (x_2 - b)^2 + c + \lambda\left(x_1^2 + x_2^2 - d^2\right).$$

Taking the first differential of $L(x_1, x_2, \lambda)$ with respect to x_1, x_2 and λ offers a set of three equations which can be set to zero. Solving this system of equations yields the optimal solution:[1]

$$\begin{cases} \frac{\partial L}{\partial x_1} = 2(x_1 - a) + 2\lambda x_1 = 0 \\ \frac{\partial L}{\partial x_2} = 2(x_2 - b) + 2\lambda x_2 = 0 \\ \frac{\partial L}{\partial \lambda} = (x_1^2 + x_2^2 - d^2) = 0 \end{cases} \Rightarrow \begin{cases} x_1 = \frac{a}{1+\lambda} \\ x_2 = \frac{b}{1+\lambda} \\ \lambda = -1 + \sqrt{\frac{a^2+b^2}{d^2}} \end{cases}$$

Although the method of Lagrange multipliers is a very powerful solution concept, one should recognize that it provides only *necessary conditions* for optimality. Setting the first differential equal to zero yields only information about the extreme values of a function. It is not possible to discriminate between for example a (local) minimum, maximum or a saddle point. This can only be guaranteed if the objective function and/or constraints satisfy properties for convexity. Nonetheless, sufficient conditions for a (local) minimum can be obtained when the second differential is positive. For more information on this topic, the interested reader is referred to for example Boyd and Vandenberghe (2009).

4.1.2 EMS Solution Using Method of Lagrange Multipliers

Optimization problem $\mathscr{P}_1$ can be solved using the method of Lagrange multipliers. The optimization problem is translated into discrete time. This way a set of algebraic equations appears which can be easily solved with the method of Lagrange multipliers. Some simplifications will be done to the conversion losses of powertrain components. The reader who wants to avoid these simplifications is referred to Pontryagin's Minimum Principle solution in Sect. 4.2. Furthermore, no restrictions are posed on the set of admissible controls $\mathscr{U}$, so the control input u is assumed to be unbounded.

The vehicle configuration under consideration is a P-HEV, but without loss of generality a similar approach can be applied for an S-HEV. A predefined drive cycle is selected (e.g., NEDC or FTP) including shift strategy. This means that the requested propulsion power P_r as well as engine speed ω are known a priori.

The Willans line model provides a quasi-static representation of the ICE losses, see also Sect. 2.3.1.1 or Wei and Rizzoni (2001). This model is selected to describe the input–output behavior of the ICE. When the requested power from the engine is always non-negative, a quadratic fit could be used:

$$P_f \approx \gamma_{p,2} P_p^2 + \gamma_{p,1} P_p + \gamma_{p,0}, \tag{4.1}$$

[1] In this example the optimal solution will only be found if $a^2 + b^2 \leq d^2$. If this condition is not satisfied, there will be no constraint active (i.e., the minimum of the function emerges outside the circle with radius d) and the trivial solution holds: $\min y = c$.

where $\gamma_{p,2}$, $\gamma_{p,1}$ and $\gamma_{p,0}$ are time dependent engine coefficients (depending on ICE speed ω). For didactic reasons, it is decided to omit this time and speed dependency in the equations below. Furthermore, it is assumed that electric loads do not consume power, so $P_l = 0$. Also the power losses in the other powertrain components are neglected. This means that the electric motor and battery convert energy without energy losses. Together with the powersplit from (3.8) one can now express P_f as function of control input $u = P_s$:

$$\begin{aligned} P_f &\approx \gamma_{p,2}(P_r - P_m)^2 + \gamma_{p,1}(P_r - P_m) + \gamma_{p,0}, \\ &= \gamma_{p,2}(P_r - P_s)^2 + \gamma_{p,1}(P_r - P_s) + \gamma_{p,0}, \\ &= \gamma_{p,2}P_s^2 - (2\gamma_{p,2}P_r + \gamma_{p,1})P_s + \gamma_{p,2}P_r^2 + \gamma_{p,1}P_r + \gamma_{p,0}, \\ &= \varphi_2 P_s^2 + \varphi_1 P_s + \varphi_0, \end{aligned} \tag{4.2}$$

where $\varphi_2 = \gamma_{p,2}$, $\varphi_1 = -2P_r\gamma_{p,2} - \gamma_{p,1}$ and $\varphi_0 = \gamma_{p,2}P_r^2 + \gamma_{p,1}P_r + \gamma_{p,0}$ characterize the complete energy path of the powertrain (depending on ω and P_r).

The performance index of $\mathscr{P}_1$ integrates the power consumption P_f along the drive cycle. In discrete time this translates into a summation over time:

$$J_f = \sum_{k=1}^{n} P_f(k, P_s, P_r)\Delta t \approx \sum_{k=1}^{n} \big(\varphi_2(k)P_s(k)^2 + \varphi_1(k)P_s(k) + \varphi_0(k)\big)\Delta t, \tag{4.3}$$

with discrete time index k and sampling interval Δt. The total number of samples n is calculated from the drive cycle length:

$$n = \left\lceil \frac{t_f - t_0}{\Delta t} \right\rceil. \tag{4.4}$$

Note that P_f in (4.3) does not depend on E_s, owing to the state independent battery model. As a result, the solution of $\mathscr{P}_1$ will not be influenced by the dynamical state equation (unless there are state constraints). After omitting this state equation only the end-point constraint remains. In discrete time this is written as

$$\sum_{k=1}^{n} P_s(k)\Delta t = 0. \tag{4.5}$$

Altogether, a simplified optimization problem emerges, where the sampling time has been omitted (without consequences for the solution):

$$\begin{aligned} \min_{P_s(k)} \quad & J_f = \sum_{k=1}^{n} \big(\varphi_2(k)P_s(k)^2 + \varphi_1(k)P_s(k) + \varphi_0(k)\big), \\ \text{subject to} \quad & \sum_{k=1}^{n} P_s(k) = 0. \end{aligned} \tag{4.6}$$

Searching for the optimal control input P_s^* will be done using the method of Lagrange multipliers. The Lagrangian is constructed from the performance index and adjoining the end-point constraint with a Lagrange multiplier p:

$$L = \sum_{k=1}^{n} \left(\varphi_2(k) P_s(k)^2 + \varphi_1(k) P_s(k) + \varphi_0(k)\right) + p \sum_{k=1}^{n} P_s(k). \tag{4.7}$$

In this Lagrangian the multiplier p can be seen as a fuel equivalent weighting factor:[2] it weights the cumulative energy exchange with the battery against energy consumed by the ICE. This explains the use of the name Equivalent Consumption Minimization Strategy (ECMS) in literature, see Paganelli et al. (2002), Guzzella and Sciarretta (2005). Two extreme situations can be recognized for p: the situation with $p \to -\infty$ means that energy from the battery can be utilized to reduce the Lagrangian and the battery will most probably be depleted at the end of the drive cycle. The situation with $p \to \infty$ makes energy in the battery extreme expensive and maximally charging the battery will be the preferred situation (such that the battery becomes eventually overcharged).

Taking the derivative of the Lagrangian offers necessary conditions for the optimal solution:

$$\frac{\partial L}{\partial P_s(k)} = 0 \quad \text{with } k = 1, 2, \ldots, n \tag{4.8}$$

$$\frac{\partial L}{\partial p} = 0. \tag{4.9}$$

These conditions offer a set of $n + 1$ equations with $n + 1$ unknown variables $P_s(1), P_s(2), \ldots, P_s(n)$ and p. Solving this set of equations yields

$$\begin{aligned} \frac{\partial L}{\partial P_s(k)} &= 2\varphi_2 P_s(k) + \varphi_1 + p = 0 \\ \Rightarrow \quad P_s^*(k) &= -\frac{p + \varphi_1}{2\varphi_2}, \end{aligned} \tag{4.10}$$

$$\begin{aligned} \frac{\partial L}{\partial p} &= \sum_{k=1}^{n} P_s(k) = -\sum_{k=1}^{n} \frac{p + \varphi_1}{2\varphi_2} = -\sum_{k=1}^{n} \frac{p}{2\varphi_2} - \sum_{k=1}^{n} \frac{\varphi_1}{2\varphi_2} = 0 \\ \Rightarrow \quad p^* &= \frac{-\sum_{k=1}^{n} \frac{\varphi_1}{2\varphi_2}}{\sum_{k=1}^{n} \frac{1}{2\varphi_2}}. \end{aligned} \tag{4.11}$$

Considering this analytical solution, the following observations are made:

[2] In the automotive industry λ is inextricable related to the ICE air/fuel ratio. It is desirable to use an alternative symbol and in this application area the symbol p is used instead of λ.

- Given the optimal solution P_s^* and p^*, the optimality conditions from (4.8) and (4.9) guarantee that a small disturbance δP_s^* or δp^* will not result in variation for:

$$\delta L := \frac{\partial L}{\partial P_s}\delta P_s^* + \frac{\partial L}{\partial p}\delta p^*. \tag{4.12}$$

  Recall that (4.8) and (4.9) offer only necessary conditions and without further knowledge of the optimization problem under consideration there exists the possibility that local extrema are found (i.e., local minimum/maximum or saddle point instead of the global minimum). Returning back to the quadratic fit of the ICE from (4.1), it follows that the second differential satisfies positiveness if $\gamma_{p,2} > 0$. Given the general properties of the Willans lines, it is reasonable to assume that this assumption holds in practice. As a result, it can be approved that the optimal solution P_s^* from (4.10) represents the sequence where (4.6) achieves its global minimum.
- An explicit expression is given for the optimal Lagrange multiplier p^* in (4.11). Calculation of p^* requires that the coefficients φ_1 and φ_2 are known for $k = 1, \ldots, n$. As shown in (4.2), they depend on ω and P_r. Consequently, it can be concluded that the exact drive cycle needs to be known in advance to calculate p^*. Requiring this a priori information means that the EMS is non-causal.

  Recall that $\varphi_2 = \gamma_{m,2}$ and $\varphi_1 = -2P_r\gamma_{p,2} - \gamma_{p,1}$. Under the assumption that the characteristic ICE equation (4.1) defines $\gamma_{p,2} > 0$ and that P_r, the power request requested for vehicle propulsion, is in most cases positive,[3] it follows that $\varphi_2 > 0$ and $\varphi_1 < 0$. Altogether, this means that $p^* > 0$ for most real-world drive cycles.
- $P_s^*(k)$ depends only on coefficients at time k as well as multiplier p^*. This means that in case p^* is known, one can calculate the optimal control input P_s^* with only information about the present moment k. This is an important property when considering online solutions and will be further discussed in Chap. 6.

The optimal solution P_s^* as function of p is visualized in Fig. 4.2. At each time instant k, the parameters φ_1 and φ_2 are updated and shape the relation between P_s^* and p. In the discussion up to now, no limitations were posed on the control input $u \in \mathscr{U}$. Component capabilities, however, will limit the admissible set $\mathscr{U}$. The power limits of the battery, motor/generator and ICE from Sect. 3.5 can be rewritten into a single upper and lower bound for $\mathscr{U}$:

$$\mathscr{U} = [\underline{P}_s, \overline{P}_s], \tag{4.13}$$

with

$$\begin{aligned} \underline{P}_s &= \max(\underline{P}_b, \underline{P}_m, -\overline{P}_p + P_r), \\ \overline{P}_s &= \min(\overline{P}_b, \overline{P}_m, -\underline{P}_p + P_r). \end{aligned} \tag{4.14}$$

[3] Only in situations of firm braking we have $P_r \ll 0$ such that φ_1 becomes non-negative.

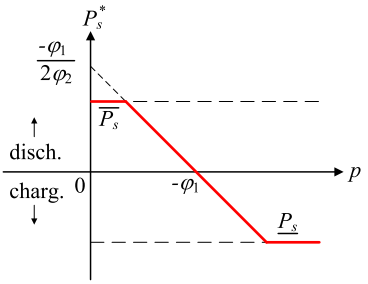

Fig. 4.2 Characterization of optimal solution P_s^* as function of Lagrange multiplier p. Maximum and minimum power limits of components are incorporated by means of saturation (i.e., $\overline{P}_s$ and $\underline{P}_s$, respectively)

Typically these limitations appear in terms of actuator saturation in the optimization problem, as visualized in Fig. 4.2. It is evident that these limitations influence the optimality of the unconstrained solution presented in (4.10). Solution methods exist to incorporate these input constraints without loss of optimality (although properties on convexity are required as discussed in, e.g., Hull (2003), Vinter (2000)). These solution methods will not be further discussed here.

4.2 Pontryagin's Minimum Principle

This introduction is inspired by the textbook of Zak (2003). It provides a clear explanation of the basic concepts behind the Hamiltonian function and Pontryagin's Minimum Principle (PMP). In a similar way, this section presents a concise overview which is directly applicable to the problem formulation for energy management. For an extensive and mathematically precise explanation, the interested reader is referred to Luenberger (1969), Kirk (1970) or Liberzon (2012) and the references therein.

4.2.1 Introduction to the Hamiltonian Function

In this section a dynamical system with the following state equation is considered:

$$\dot{x} = f(t, x, u), \qquad x(t_0) = x_0,$$

with time t, states x, initial state x_0 and control input u. For this system a basic performance index J is defined over a fixed time interval $t \in [t_0, t_f]$ and steers the system from x_0 to a final state x_f:

$$J\big(t_0, x(t_0), u\big) = \int_{t_0}^{t_f} F\big(\tau, x(\tau), u(\tau)\big)\,\mathrm{d}\tau. \tag{4.15}$$

The basic control problem is to find an optimal control law $u^*(t)$, $t \in [t_0, t_f]$ which minimizes this objective function, resulting in $J^*(t, x(t_0))$ with optimal state trajec-

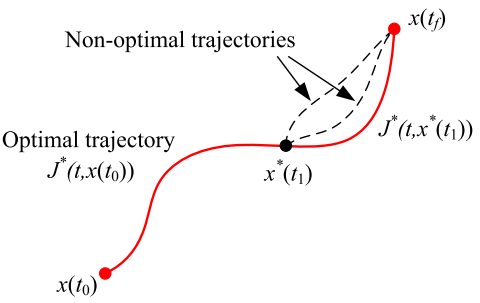

Fig. 4.3 Illustration of optimal state trajectory x^* from initial state $x(t_0)$ to final state $x(t_f)$ and corresponding performance index $J^*(t, x(t_0))$. An optimal trajectory also exists on the sub-interval $t = [t_1, t_f]$ and forms the basis behind Bellman's principle of optimality

tory $x^*(t)$. This optimal performance index and its corresponding state trajectory is visualized in Fig. 4.3.

In line with the optimal performance index $J^*(t, x(t_0))$, one can also define a subproblem starting at time t_1 on the optimal trajectory $x^*(t_1)$, $t_0 \leq t_1 \leq t_f$ and covering only the last part of the trajectory:

$$J\big(t, x^*(t_1), u\big) = \int_{t_1}^{t_f} F\big(\tau, x(\tau), u(\tau)\big)\,\mathrm{d}\tau \quad \text{with } t_1 \leq t \leq t_f. \tag{4.16}$$

Again we see that the optimal control input $u^*(t)$, $t \in [t_1, t_f]$ minimizes this truncated objective function, which is denoted by $J^*(t, x^*(t_1))$. In fact $J^*(t, x^*(t_1))$ denotes the optimal trajectory from state $x^*(t_1)$ to the final state x_f, see Fig. 4.3. Now recall Richard Bellman's *Principle of Optimality*:

> An optimal policy has the property that whatever the initial state and initial decision are, the remaining decisions must constitute an optimal policy with regard to the state resulting from the first decision; Bellman (1957).

Roughly speaking, the principle of optimality states the following fact: Let $u^*(t), t \in [t_0, t_f]$ be an optimal solution for the basic optimization problem with performance index (4.15). Then the truncated optimal solution $u^*(\tau)$, $\tau \in [t_1, t_f]$ is also optimal for the subproblem with performance index (4.16).

The justification of this fact is rather straightforward and is typically proved by contradiction. Suppose that the truncated solution $u^*(\tau)$ was not the optimal solution, there would exist another solution that further reduces the subproblem performance index. But that would also imply that at time t_1 the basic solution $u^*(t)$ could switch to this alternative solution and improve its performance. This contradicts with the assumption that $u^*(t)$ is the optimal solution.

A small example is given. Assume that the fastest route from Amsterdam to Paris passes through Brussels. Then the fastest route from Brussels to Paris will also coincide with the last part of the fastest route from Amsterdam to Paris. For more details on this principle of optimality, the reader is referred to the work of Bertsekas (2000), Vol. 1.

Returning back to the basic performance index, the principle of optimality makes it possible to split up the integration interval of the basic optimization problem (4.15) and formulate an inequality that should always hold (i.e., necessary condition). The integration of the original function $F(t, x, u)$ is split up in two time intervals: $t \in [t_0, t_1] \cup [t_1, t_f]$. Suppose that the first interval starts with state x_0 and an arbitrary control law u is applied. The second interval starts with optimal state $x^*(t_1)$ and applies the optimal control law u^*. By construction, the performance of the first interval plus the second interval will always be higher (or equal in the best situation) than the optimal performance index, so the following inequality should hold:

$$\int_{t_0}^{t_1} F\big(\tau, x(\tau), u(\tau)\big)\,\mathrm{d}\tau + J^*\big(t, x^*(t_1)\big) \geq J^*\big(t, x^*(t_0)\big). \tag{4.17}$$

Bringing all terms of the above equation to the left and dividing by $(t_1 - t_0)$ yields

$$\frac{1}{t_1 - t_0}\int_{t_0}^{t_1} F\big(\tau, x(\tau), u(\tau)\big)\,\mathrm{d}\tau + \frac{J^*(t, x^*(t_1)) - J^*(t, x^*(t_0))}{t_1 - t_0} \geq 0. \tag{4.18}$$

Let the interval $(t_1 - t_0)$ become infinitely small, so $t_1 \to t_0$. Then the integral from the first term is eliminated and the partial derivative can be obtained from the second term:

- Eliminating the integral of the first term is illustrated with a simple approximation:

$$\int_{t_0}^{t_1} F(t)\,\mathrm{d}t \approx \frac{F(t_0) + F(t_1)}{2}(t_1 - t_0) \approx F(t_0)(t_1 - t_0),$$

  where the approximation becomes exact[4] when $t_1 \to t_0$.
- The second term expresses a difference quotient and the partial derivative emerges when the limit tends to zero:

$$\lim_{\Delta t \downarrow 0} \frac{\phi(t + \Delta t) - \phi(t)}{\Delta t} = \frac{\partial \phi(t)}{\partial t}.$$

  Recall that J^* in (4.18) is a function of two variables t and x^*, so the partial derivative is obtained. Furthermore, x^* is a function of t, so also the chain rule needs to be taken into account.

Using these mathematical principles, the following inequality emerges:

[4]Note that mathematical conditions, e.g., $F(t)$ should be continuous and has continuous partial derivatives, are neglected here for simplicity.

$$F\big(t, x(t), u(t)\big) + \frac{\partial J^*(t, x(t))}{\partial t} + \sum_{i=1}^{n} \frac{\partial J^*(t, x(t))}{\partial x_i} \dot{x}_i$$

$$= F\big(t, x(t), u(t)\big) + \frac{\partial J^*(t, x(t))}{\partial t} + \sum_{i=1}^{n} \frac{\partial J^*(t, x(t))}{\partial x_i} f_i \geq 0.$$

Altogether, it is concluded that for any $x_0 \neq x_f$ we have

$$F + \frac{\partial J^*}{\partial t} + \sum_{i=1}^{n} \frac{\partial J^*}{\partial x} f \geq 0.$$

Now the *Hamiltonian* function is defined:

$$H(t, x, u, p) = F + p^\top f(t, x, u), \tag{4.19}$$

with

$$p = \begin{bmatrix} \frac{\partial J^*}{\partial x_1} & \frac{\partial J^*}{\partial x_2} & \cdots & \frac{\partial J^*}{\partial x_n} \end{bmatrix}^\top, \quad p^\top \neq 0. \tag{4.20}$$

This results in the following inequality:

$$\frac{\partial J^*(t, x)}{\partial t} + H(t, x, u, p) \geq 0. \tag{4.21}$$

The reasoning followed so far split up the state trajectory from x_0 to x_f in two subsequent trajectories with x_1 as intermediate point. An arbitrary control input u was selected for the first part (from x_0 to x_1), which will in most cases not result in an optimal trajectory x^*. For this reason, an inequality is introduced in (4.17). From the same principle of optimality one can also derive that equality should hold by selecting the optimal control input u^* for the state trajectory from x_0 to x_1. In that particular situation the Hamiltonian should achieve its minimum. This is expressed as

$$\frac{\partial J^*(t, x)}{\partial t} + \min_u H(t, x, u, p) = 0. \tag{4.22}$$

This (partial) differential equation is called the *Hamilton–Jacobi–Bellman* (HJB) equation. Its solution provides the optimal control input u^*, but an analytical solution is typically not found in practical cases. Nonetheless, the HJB equation turns out to be a powerful tool in finding numerical solutions. More specifically, the Hamiltonian $H(t, x^*, u, p^*)$ has a global minimum if $u = u^*$, so we have

$$H\big(t, x^*, u^*, p^*\big) \leq H\big(t, x^*, u, p^*\big), \tag{4.23}$$

for all admissible u and all $t \in [t_0, t_f]$. In other words, from the optimal control input it is known that it will minimize the Hamiltonian. This property is graphically shown in Fig. 4.4. A formal proof is provided in, e.g., Geering (2007). Note that this

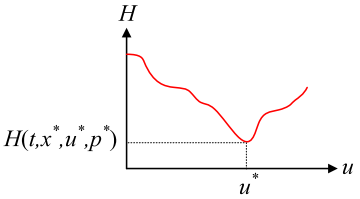

Fig. 4.4 Graphical representation of Hamilton–Jacobi–Bellman equation where optimal input u^* minimizes the Hamiltonian: $H(t, x^*, u^*, p^*) \leq H(t, x^*, u, p^*)$

is only a necessary condition, which means that an optimal solution must satisfy the minimum principle. However, the reverse does not automatically hold, so there can exist alternative solutions which satisfy this minimum principle but they are not optimal, see Kirk (1970), p. 232.

To summarize these considerations, Theorem 5.5 is cited from Zak (2003):

Let $\dot{x} = f(t, x, u)$ be a control system model, let $\mathscr{U}$ be a set of admissible control inputs, and let x_f be a prescribed final state. If we suppose that

1. for any $x \neq x_f$ there exists an admissible optimal control input transferring x to x_f, and
2. the function $J^*(t, x(t))$, which is the time optimal transfer of the system from x, at time t, to x_f, is continuously differentiable except at the point x_f, then

$$\frac{\partial J^*(t,x)}{\partial t} + H(t, x, u, p) \geq 0 \quad \text{for any } u \in \mathscr{U} \text{ and } x \neq x_f,$$

$$\frac{\partial J^*(t,x)}{\partial t} + \min_u H(t, x, u, p) = 0$$

for any optimal transfer where $x \neq x_f$.

4.2.2 Introduction to Pontryagin's Minimum Principle

In the previous section the HJB equation has been introduced. It was discussed that searching for the optimal control input u^* can be done by minimizing the Hamiltonian function:

$$u^* = \arg\min_{u \in \mathscr{U}} H(t, x, u, p). \tag{4.24}$$

The knowledge that u^* minimizes the Hamiltonian (and offering the optimal trajectory x^*), can also be used to derive necessary conditions for optimality on u and p. There should be noted that the optimal solution will also prescribe $p^*(t)$ according

to a dynamical equation and finding this so-called costate equation will be described in this section.

Suppose that the optimal trajectory x^* and corresponding input u^* are known. By construction of the Hamiltonian in (4.19) we have

$$\frac{\partial H}{\partial p} = f\left(t, x^*, u^*\right) = \dot{x}^*(t). \tag{4.25}$$

Furthermore, due to (4.24), one finds that a small disturbance δu will not lead to a lower value of the Hamiltonian.[5] This implies that the partial derivative of H can be set to zero to search for the optimal solution:

$$\frac{\partial H}{\partial u} = 0. \tag{4.26}$$

Condition (4.26) can be directly applied in practice and needs no further explanation. To derive a solution for the costate p can be done in several ways and is more involved. One approach[6] is to require that J in (4.15) is stationary, but also to respect the state equation. To this end, the state equation, in the form of $f(t, x, u) - \dot{x} = 0$, can be added with p as Lagrange multiplier to the integrand of J, leading to

$$\tilde{J} = \int_{t_0}^{t_f} \left(F(t, x, u) + p^\top \left(f(t, x, u) - \dot{x}\right)\right) \mathrm{d}t.$$

Use the definition of H in (4.19) to get

$$\tilde{J} = \int_{t_0}^{t_f} \left(H(t, x, u, p) - p^\top \dot{x}\right) \mathrm{d}t. \tag{4.27}$$

The resulting expression should be invariant for small perturbations δx, δu, and δp. The variation of (4.27) for these perturbations will lead to the following sequence:

$$\delta\tilde{J} = \int_{t_0}^{t_f} \left(H_x^\top \delta x + H_u^\top \delta u + H_p^\top \delta p - p^\top \delta\dot{x} - \dot{x}^\top \delta p\right) \mathrm{d}t,$$

with $H_x = \frac{\partial H}{\partial x}$, etc. Rearrange to get

$$\delta\tilde{J} = \int_{t_0}^{t_f} \left(H_x^\top \delta x + H_u^\top \delta u + (H_p - \dot{x})^\top \delta p - p^\top \delta\dot{x}\right) \mathrm{d}t.$$

Integration by parts will introduce a term $\dot{p}^\top \delta x$, instead of $-p^\top \delta\dot{x}$,

$$\delta\tilde{J} = p^\top(t_f)\delta x(t_f) - p^\top(t_0)\delta x(t_0)$$

[5] Some mathematical background is neglected here, but in general this requires that J^* has continuous second partial derivatives and also the dynamical system equation f has continuous first derivatives.

[6] Also in this derivation some assumptions are left implicit.

$$+\int_{t_0}^{t_f}\left((H_x+\dot{p})^\top\delta x+H_u^\top\delta u+(H_p-\dot{x})^\top\delta p\right)\mathrm{d}t.$$

Now realize that $x(t_0)=x_0$ so $\delta x(t_0)=0$ and when $x(t_f)=x_f$ is prescribed then $\delta x(t_f)=0$ also, thus

$$\delta\tilde{J}=\int_{t_0}^{t_f}\left((H_x+\dot{p})^\top\delta x+H_u^\top\delta u+(H_p-\dot{x})^\top\delta p\right)\mathrm{d}t.$$

The coefficients before the perturbations should vanish for the optimal solution. From this requirement follow (4.25) and (4.26), that were already derived in a different way, but also

$$H_x=\frac{\partial H}{\partial x}=-\dot{p}^*. \tag{4.28}$$

Altogether, the results from PMP describe the following set of necessary conditions for all $t\in[t_0,t_f]$:

$$\begin{aligned}\dot{x}^*(t)&=\frac{\partial H}{\partial p}\big(t,x^*(t),u^*(t),p^*(t)\big),\\ \dot{p}^*(t)&=-\frac{\partial H}{\partial x}\big(t,x^*(t),u^*(t),p^*(t)\big),\\ 0&=\frac{\partial H}{\partial u}\big(t,x^*(t),u^*(t),p^*(t)\big).\end{aligned}$$

It is possible to use a definition of the Hamiltonian different from (4.19), namely

$$H(t,x,u,p)=F-p^\top f(t,x,u), \tag{4.29}$$

which involves only a sign change for p. By carrying on this sign change for p, the necessary conditions become

$$\begin{aligned}\dot{x}^*(t)&=-\frac{\partial H}{\partial p}\big(t,x^*(t),u^*(t),p^*(t)\big),\\ \dot{p}^*(t)&=\frac{\partial H}{\partial x}\big(t,x^*(t),u^*(t),p^*(t)\big),\\ 0&=\frac{\partial H}{\partial u}\big(t,x^*(t),u^*(t),p^*(t)\big).\end{aligned} \tag{4.30}$$

This formulation has the advantage of leading to equations that follow the same pattern as the solution with the Lagrange multiplier and is also leading to solutions for the EMS problem with a p that is normally positive, facilitating the interpretation of the results, where p can be interpreted as a cost ratio.

4.2.3 EMS Solution Using Pontryagin's Minimum Principle

This section presents the solution to optimization problem $\mathscr{P}_1$ using the minimum principle of Pontryagin. The first step is to derive the Hamiltonian from $\mathscr{P}_1$. Then the necessary conditions from PMP are applied to derive an optimal solution.

Recall the dynamical system $\dot{x} = f$ from $\mathscr{P}_1$ which has only one state variable $x = E_s$, which is the energy stored in the battery. The state equation becomes

$$\dot{x} = f(t, x, u) = -P_s(t). \tag{4.31}$$

Following the same reasoning as with the method from Lagrange multipliers, P_s is selected as control input, so $u = P_s$. Again, the performance index J represents the cumulative fuel consumption and can be written as function of P_s. The same approximation (4.2) will be adopted:

$$\begin{aligned} J\big(t_0, x(t_0), u\big) &= \int_{t_0}^{t_f} F\big(t, x(t), u(t)\big)\,\mathrm{d}t \\ &= \int_{t_0}^{t_f} P_f\big(t, x(t), u(t)\big)\,\mathrm{d}t \\ &\approx \int_{t_0}^{t_f} \varphi_2(t) P_s^2(t) + \varphi_1(t) P_s(t) + \varphi_0(t)\,\mathrm{d}t. \end{aligned} \tag{4.32}$$

Now the Hamiltonian from (4.29) can be constructed using (4.31) and (4.32). For simplicity the dependence on time is omitted:

$$H = F - pf = \varphi_2 P_s^2 + \varphi_1 P_s + \varphi_0 + p P_s. \tag{4.33}$$

Note that the dynamic system $\dot{x} = f(t, x, u)$ incorporates only one state equation, so p is a scalar and not a vector.

The necessary conditions will be applied to search for the optimal solution. From (4.30) the solution for P_s^* can be derived:

$$\frac{\partial H}{\partial u} = 0 \quad \Rightarrow \quad 2\varphi_2 P_s + \varphi_1 + p = 0 \quad \Rightarrow \quad P_s^* = -\frac{p + \varphi_1}{2\varphi_2}. \tag{4.34}$$

The costate equation is

$$\dot{p} = \frac{\partial H}{\partial x} = \frac{\partial H}{\partial E_s} = 0. \tag{4.35}$$

According to the expectations, the solution P_s^* from (4.34) is exactly identical to the solution (4.10) obtained with the method of Lagrange multipliers. Moreover, it turns out that $p(t)$ is constant and remains equal to its initial value $p(t_0)$. A similar observation was also done in Sect. 4.1.2. Note that therein (4.11) an analytical expression was derived for p^*. Applying this value for p will also yield here the

optimal solution and one can calculate P_s^* from (4.34). This solution will provide a charge sustaining solution where E_s returns back to the initial state x_0 at $t = t_f$.

That the necessary conditions from PMP do not provide an explicit solution for $p(t_0)$ is a weak point, compared to the method with the Lagrange multipliers. But it is well understandable because PMP does not include an explicit end-point constraint on x. On the other hand, PMP easily provides the solution for P_s without converting the optimization problem into discrete time. This is an attractive advantage for using PMP. In general one can say that finding an analytical expression for the initial costate requires knowledge about the target final state $x(t_f)$. With this information one can calculate back the required starting value for the costate $p(t_0)$. A detailed description is given in Chap. 5.

4.2.4 EMS Solution with Model Equations Taken from Chap. 2

PMP presented in the previous section offers an analytical solution for the optimal value P_s^*. By careful selection of the decision variable P_s and the (oversimplified) model equations, this analytical solution emerged. However, finding an analytical solution for practical situations is far from trivial as will be shown in this section. By selecting more complex model equations, the necessary conditions from PMP typically lead to expressions that cannot be solved analytically. Instead, numerical solvers need to be used.

Similar to the previous section, the optimization problem $\mathscr{P}_1$ will be solved for the P-HEV configuration using PMP. Now the decision variable P_b is selected instead of P_s, so the battery terminal power is selected and not the net stored battery power. This is more attractive from a practical point of view, since P_b can be measured from the battery terminals whereas P_s is not directly observable. Also the model equations from Chap. 2 are now considered such that losses in the motor/generator and the battery are introduced. For convenience, all model equations for the P-HEV are repeated below using a concise notation (to save space in the final equations).

- *Powersplit*: The mechanical powersplit between ICE, electric motor and requested driveline power is described by

$$P_r = P_p + P_m. \tag{4.36}$$

- *ICE*: Instead of selecting a quadratic approximation for the relation between fuel power P_f and mechanical power P_p, now the affine relation from (2.4) is selected. For didactic reasons the negative power range is neglected and the dependency on engine speed ω is also omitted:

$$P_f = \gamma_{p,1} P_p + \gamma_{p,0} \overline{P}_p, \tag{4.37}$$

with $\overline{P}_p$ the maximum ICE power.

- *Motor/generator*: The motor/generator incorporates losses which are represented by the quadratic relation from (2.8). Here a single quadratic relation is adopted. The distinct quadratic functions for motor and generator mode can be obtained by evaluating with the parameters for the appropriate mode:

$$P_b = \gamma_{m,2} P_m^2 + \gamma_{m,1} P_m + \gamma_{m,0}. \tag{4.38}$$

This quadratic equation can be solved for P_m as follows:

$$P_m = \frac{-\gamma_{m,1} + \sqrt{\gamma_{m,1}^2 + 4\gamma_{m,2}(P_b - \gamma_{m,0})}}{2\gamma_{m,2}}. \tag{4.39}$$

Note that P_l is assumed to be zero here, so electric power for the auxiliaries is neglected.

- *Battery*: The battery model from Sect. 2.3.3 offers the description for the battery with internal series resistance R:

$$P_s = I_s^2 R + P_b. \tag{4.40}$$

The relation between I_s and P_s is taken from (2.16) with U_{oc} the state-of-energy dependent open-circuit voltage:

$$I_s = \frac{U_{\text{oc}} - \sqrt{U_{\text{oc}}^2 - 4RP_b}}{2R}. \tag{4.41}$$

This latter relation makes it possible to express P_s as function of U_{oc} and P_b by using $P_s = U_{\text{oc}} I_s$, so

$$P_s = \frac{U_{\text{oc}}}{2R}\left(U_{\text{oc}} - \sqrt{U_{\text{oc}}^2 - 4RP_b}\right). \tag{4.42}$$

Finally, (2.12) provides the affine relation between U_{oc} and battery state E_s:

$$U_{\text{oc}}(E_s) = U_0 + \phi E_s. \tag{4.43}$$

Now that the model equations are known, a Hamiltonian will be formulated for $\mathscr{P}_1$. The associated performance index is obtained by writing P_f as function of P_b. Therefore, (4.36) and (4.39) are substituted into (4.37):

$$\begin{aligned} P_f &= \gamma_{p,1}(P_r - P_m) + \gamma_{p,0}\overline{P}_p \\ &= \gamma_{p,1}\left(P_r - \frac{-\gamma_{m,1} + \sqrt{\gamma_{m,1}^2 + 4\gamma_{m,2}(P_b - \gamma_{m,0})}}{2\gamma_{m,2}}\right) + \gamma_{p,0}\overline{P}_p. \end{aligned} \tag{4.44}$$

The state equation $\dot{E}_s = -P_s$ of the battery is a constraint that should be respected. It is adjoined to the performance index with the Lagrange multiplier p. By considering

(4.42) and (4.44) the following Hamiltonian emerges, where the sign convention for p compatible to the Lagrangian approach has been used:

$$\begin{aligned} H &= P_f - p\dot{x} = P_f + pP_s \\ &= \gamma_{p,1}\left(P_r - \frac{-\gamma_{m,1} + \sqrt{\gamma_{m,1}^2 - 4\gamma_{m,2}(\gamma_{m,0} - P_b)}}{2\gamma_{m,2}}\right) + \gamma_{p,0}\overline{P}_p \\ &\quad + p\frac{U_{\mathrm{oc}}}{2R}\left(U_{\mathrm{oc}} - \sqrt{U_{\mathrm{oc}}^2 - 4RP_b}\right). \end{aligned} \tag{4.45}$$

To find the optimal control inputs, the necessary conditions from PMP are calculated:

$$\frac{\partial H}{\partial P_b} = 0,$$
$$\frac{\partial H}{\partial E_s} = \dot{p}.$$

The first condition can be calculated straightforward from (4.45):

$$\begin{aligned} \frac{\partial H}{\partial P_b} &= \frac{\gamma_{p,1}}{2\gamma_{m,2}} \frac{-2\gamma_{m,2}}{\sqrt{\gamma_{m,1}^2 + 4\gamma_{m,2}(P_b - \gamma_{m,0})}} + p\frac{U_{\mathrm{oc}}}{2R}\frac{-2R}{\sqrt{U_{\mathrm{oc}}^2 - 4RP_b}} \\ &= \frac{-\gamma_{p,1}}{\sqrt{\gamma_{m,1}^2 + 4\gamma_{m,2}(P_b - \gamma_{m,0})}} + p\frac{U_{\mathrm{oc}}}{\sqrt{U_{\mathrm{oc}}^2 - 4RP_b}} = 0. \end{aligned} \tag{4.46}$$

Solving this expression finally yields the optimal control input P_b^*:

$$P_b^* = \frac{U_{\mathrm{oc}}^2(\gamma_{p,1}^2 - p^2\gamma_{m,1}^2 + 4p^2\gamma_{m,2}\gamma_{m,0})}{4(R\gamma_{p,1}^2 + p^2U_{\mathrm{oc}}^2\gamma_{m,2})}. \tag{4.47}$$

There should be noted that this analytical solution comes with additional constraints. For example (4.46) poses two extra restrictions on P_b to make sure that no complex roots emerge:

$$\gamma_{m,1}^2 - 4\gamma_{m,2}(\gamma_{m,0} - P_b) > 0 \quad \Rightarrow \quad P_b > \gamma_{m,0} - \frac{\gamma_{m,1}^2}{4\gamma_{m,2}}, \tag{4.48}$$

$$U_{\mathrm{oc}}^2 - 4RP_b > 0 \quad \Rightarrow \quad P_b < \frac{U_{\mathrm{oc}}^2}{4R}. \tag{4.49}$$

The first restriction stems from the electric machine characteristic which obtains a horizontal slope for $P_b = \gamma_{m,0} - \frac{\gamma_{m,1}^2}{4\gamma_{m,2}}$. This solution for P_b^* will be obtained for $p \to \infty$. The second restriction is the maximum power that can be drained from the battery. This solution will be obtained for $p \downarrow 0$. Using the data from Table 2.1,

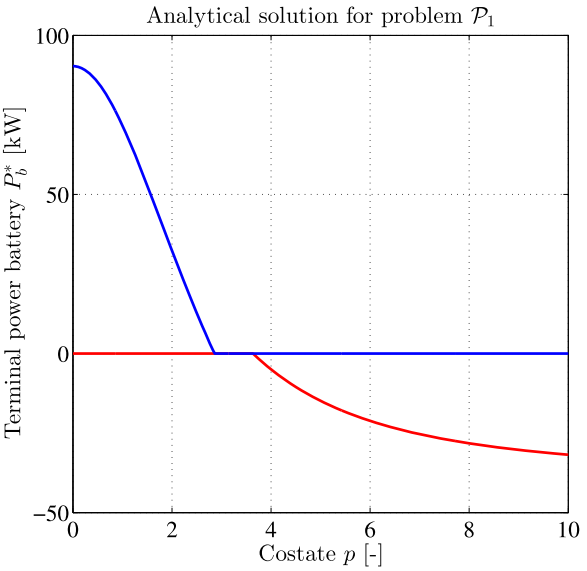

Fig. 4.5 Optimal solution for control input P_b as a function of costate p. Note that the solution for different branches of the motor/generator characteristic is saturated to the appropriate domain of P_b

the relation between p and the optimal P_b is depicted in Fig. 4.5. Instead of this analytical solution, numerical solvers can be used to calculate the optimal P_b^* that achieves the global minimum for (4.45). This method will be further explained in Chap. 6.

Now the second PMP condition is applied to find an expression for the costate p. First (4.43) needs to be substituted into (4.45) to express the dependency on E_s for U_{oc}. Next, taking the differential of the Hamiltonian gives

$$\begin{aligned}\dot{p} = \frac{\partial H}{\partial E_s} &= \frac{p}{R}(U_0 + \phi E_s)\phi - \frac{\phi p}{2R}\sqrt{(U_0 + \phi E_s)^2 - 4RP_b} \\ &\quad - (U_0 + \phi E_s)\frac{p}{4R}\frac{2(U_0 + \phi E_s)\phi}{\sqrt{(U_0 + \phi E_s)^2 - 4RP_b}} \\ &= \frac{\phi p U_{\text{oc}}}{2R}\left(2 - \frac{\sqrt{U_{\text{oc}}^2 - 4RP_b}}{U_{\text{oc}}} - \frac{U_{\text{oc}}}{\sqrt{U_{\text{oc}}^2 - 4RP_b}}\right).\end{aligned} \tag{4.50}$$

Also this second PMP condition offers an elegant analytical solution. This solution is derived from the special form that (4.50) has:

$$\dot{p} = p\zeta\left(2 - \chi - \frac{1}{\chi}\right) \tag{4.51}$$

being a first order differential equation, with $\zeta = \frac{\phi U_{\text{oc}}}{2R}$ and $\chi = \frac{\sqrt{U_{\text{oc}}^2 - 4RP_b}}{U_{\text{oc}}}$. The three terms between the brackets in (4.51) are visualized in Fig. 4.6. It can be seen that their sum never exceeds zero, so $p\dot{p} = \frac{1}{2}\frac{\mathrm{d}p^2}{\mathrm{d}t} \leq 0$ and $\dot{p} = 0$ for $\chi = 1$, so

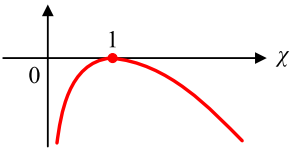

Fig. 4.6 Sign of costate derivative $\dot{p}$ will always oppose sign for costate p, so $p\dot{p} \leq 0$, which is desirable from a stability point of view

for $P_b = 0$. It is concluded that the costate p obeys a differential equation whose solution is always directed towards $p = 0$.

Note that the initial condition $p(t_0)$ is still unknown, but can be calculated if the following information is a priori known: (I) the power request from the driver (i.e., P_r) along the entire drive cycle; (II) the final battery state $E_s(t_f)$. Chapter 5 provides more background information on this subject and will show that the so-called *two-point boundary value problem* will solve this problem.

In retrospect one can say that the model equations determine to a high extend the complexity of the solution. In the solution presented in this last example the losses for the motor/generator and battery are incorporated. Indeed, this improves the accuracy of the corresponding EMS, but one must accept that also the numerical complexity readily increases. In practical situations, the model equations often incorporate many numerical data (e.g., stored in look-up-tables like brake specific fuel consumption maps) to achieve highest accuracy. Those situations will lead to a numerical solution, rather than the analytical solution presented so far. Chapter 6 will demonstrate these numerical solution concepts.

4.2.5 EMS Solution Incorporating State Constraints

All solution concepts presented so far considered the optimization problem $\mathscr{P}_1$. These solutions will work as long as the upper and lower limit of the energy storage capacity are not reached. To date, battery packs or alternative energy storage devices contribute significantly to the weight and add-on price for an HEV. Therefore HEVs are equipped with a relative small energy storage buffer. This means that the upper and lower bound for storing energy are dominantly present. Optimization problem $\mathscr{P}_2$ and $\mathscr{P}_3$ take into account these state constraints and will be addressed in this section.

The work from Maurer (1977), Seierstad and Sydsæter (1987), Hartl et al. (1995) offers necessary optimality conditions for the constrained optimization problem in $\mathscr{P}_2$. For the unconstrained problem $\mathscr{P}_1$ the PMP solution from Sect. 4.2.3 demonstrated that the costate $p(t)$ takes a constant value along the entire drive cycle. The state dependent battery losses in Sect. 4.2.4, however, resulted into a non-constant costate $p(t)$ as shown by (4.50). This will again be different with the optimal solution for $\mathscr{P}_2$. Instead of following one constant value, the trajectory for $p(t)$ now becomes piecewise constant (under the assumption that the losses in the battery are not state dependent). The necessary optimality conditions are considered in this section.

Given the optimization problem $\mathscr{P}_2$, the Hamiltonian is constructed by augmenting the performance index with the dynamic state equation:

$$H(t, E_s, P_m, p) = F - p(t) f = P_f(P_m) + p(t) P_s(E_s, P_m). \tag{4.52}$$

Note that P_m is selected here as decision variable. This makes it convenient to express P_s as function of decision variable P_m as well as battery energy state E_s.

$\mathscr{P}_2$ incorporates two state constraints which express the upper and lower bounds of the battery energy:

$$E_s(t) - \overline{E}_s \leq 0$$
$$-E_s(t) + \underline{E}_s \leq 0.$$

Following the method of Lagrange multipliers, both inequality constraints can be adjoined to the Hamiltonian using two Lagrange multipliers where λ_1 relates to the upper bound and λ_2 relates to the lower bound. The resulting Lagrangian reads

$$L(t, p, E_s, P_m) = H + \lambda_1(t)\big(E_s(t) - \overline{E}_s\big) + \lambda_2(t)\big(\underline{E}_s - E_s(t)\big). \tag{4.53}$$

It is assumed that the optimal state trajectory $E_s^*(t)$ has only finite many junction times. This means that the state constraints may become active only at a finite number of time instants. Then PMP results from Vinter (2000), Theorem 9.3.1 on p. 339, state that the optimal control sequence $P_m(t)$ requires a piecewise continuous costate trajectory (nontrivial, so $p^*(t) \not\equiv 0$) with piecewise continuous multiplier functions $\lambda_1(t)$ and $\lambda_2(t)$. Complementary slackness conditions hold for the multiplier functions $\lambda_1(t)$ and $\lambda_2(t)$. This means that they become zero at moments when the state equations are inactive.

There can be concluded that the optimal costate trajectory $p^*(t)$ may show a discontinuity at moments when a state equation becomes active. The work from Hartl et al. (1995), Theorem 4.1, p. 186, is used to define necessary jump conditions. From these conditions it follows that the jump direction is positive in case the upper constraint is reached and negative in case the lower constraint is reached. Finding analytical expressions to calculate the exact height of a jump (as well as its time location) is a cumbersome task. This will not be further treated in this chapter. Nonetheless, numerical algorithms exist that solve this problem efficiently. These algorithms will be explained in Chap. 5.

4.3 Summary Analytical Solutions

This section provides a brief overview of the method of Lagrange multipliers and Pontryagin's Minimum Principle. By showing both methods in parallel, one can recognize various analogies.

Problem definition:

$$\min_x \; J(x) \qquad \min_u \int_{t_0}^{t_f} F(t,x,u)\,\mathrm{d}t$$

$$g(x) = 0 \qquad \dot{x} = f(t,x,u)$$

Lagrangian: Hamiltonian:

$$L = J(x) + p^\top g(x) \qquad H = F - p^\top f$$

Optimality conditions:

$$\frac{\partial L}{\partial x} = 0 \qquad \frac{\partial H}{\partial x} = \dot{p}^*$$

$$\frac{\partial L}{\partial p} = 0 \qquad \frac{\partial H}{\partial p} = -\dot{x}^*$$

$$\frac{\partial H}{\partial u} = 0$$

or

$$H\left(t, x^*, u^*, p^*\right) \leq H\left(t, x^*, u, p^*\right)$$

4.4 Bibliographical Notes

In 1697 Johann Bernoulli (1667–1748) published his solution to the famous *Brachystochrone problem* when he was professor at the University of Groningen, The Netherlands. Apparently, Bernoulli was one of the first mathematicians who searched for the optimal state trajectory of a dynamical system and optimal control was born, see Willems (1996).

A good introduction to parameter optimization and optimal control theory is provided by Hull (2003). Also recommended on this subject is the work of Kirk (1970). Less focus on the mathematical aspects, but very suitable for undergraduate students is the work from Zak (2003). This textbook inspired the authors to write the informal discussion on optimal control in Sect. 4.2. People with a strong mathematical background can read the very recent work of Liberzon (2012). Also interesting is the book from Geering (2007), which gives a compact overview of different optimal control problems including many illustrative examples.

An excellent survey on (optimal) control strategies for hybrid vehicles is given by Sciarretta and Guzzella (2007). Tate and Boyd (2000) recognized as one of the first researchers that the powersplit problem in hybrid electric vehicles can be solved

using an optimal control approach. They apply a Linear Programming (LP) framework to estimate the optimal solution. In Koot et al. (2005) a similar approach has been followed, although the models used there lead to a Quadratic Programming (QP) problem. Both LP and QP relate back to the method of Lagrange multipliers as explained in Sect. 4.1.2.

Alternatively, Delprat et al. (2004) and Sciarretta et al. (2004) present the solution to the powersplit problem using Pontryagin's Minimum Principle. Nowadays the textbook by Guzzella and Sciarretta (2005) is considered as a standard on modeling and optimization of vehicle propulsion systems. It provides also a clear explanation of the Equivalent Consumption Minimization Strategy. This strategy originates from PMP as explained in Sect. 4.2. It will be further discussed in Chap. 6 when considering real-time implementable strategies.

The majority of the literature on optimal powersplit control considers only one state variable: the energy stored in the battery. Recently, researchers recognized that adding extra dynamical states in their problem definition leads to integrated powertrain control or complete vehicle energy management. For example Lescot et al. (2010) incorporated the thermal behavior of the engine cooling system and Kessels et al. (2010) treads the thermal interaction between engine and aftertreatment system. Further challenges regarding complete vehicle management can be found in Serrao et al. (2011).

References

Bellman RE (1957) Dynamic programming. Princeton University Press, Princeton
Bertsekas DP (2000) Dynamic programming and optimal control. Athena Scientific, Belmont
Boyd SP, Vandenberghe L (2009) Convex optimization, 7th edn. Cambridge University Press, New York
Delprat S, Lauber J, Guerra TM, Rimaux J (2004) Control of a parallel hybrid powertrain: optimal control. IEEE Trans Veh Technol 53(3):872–881
Geering HP (2007) Optimal control with engineering applications. Springer, Berlin
Guzzella L, Sciarretta A (2005) Vehicle propulsion systems. Springer, Berlin
Hartl RF, Sethi SP, Vickson RG (1995) A survey of the maximum principles for optimal control problems with state constraints. SIAM Rev 37:181–218
Hull D (2003) Optimal control theory for applications. Mechanical engineering series. Springer, New York
Kessels JTBA, Willems FPT, Schoot WJ, den Bosch PPJ V (2010) Integrated energy & emission management for hybrid electric truck with SCR aftertreatment. In: Proc IEEE veh power and propul conf, IEEE, Lille, pp 1–6
Kirk DE (1970) Optimal control theory: an introduction. Prentice-Hall, Englewood Cliffs
Koot M, Kessels JTBA, De Jager B, Heemels WPMH, Van den Bosch PPJ, Steinbuch M (2005) Energy management strategies for vehicular electric power systems. IEEE Trans Veh Technol 54(3):771–782
Lescot J, Sciarretta A, Chamaillard Y, Charlet A (2010) On the integration of optimal energy management and thermal management of hybrid electric vehicles. In: Proc IEEE veh power and propul conf, IEEE, Lille
Liberzon D (2012) Calculus of variations and optimal control theory: a concise introduction. Princeton University Press, Princeton

Luenberger DG (1969) Optimization by vector space methods. Series in decision and control. Wiley, New York
Maurer H (1977) On optimal control problems with bounded state variables and control appearing linearly. SIAM J Control Optim 15:345–362
Paganelli G, Guerra TM, Delprat S, Guezennec Y, Rizzoni G (2002) Optimal control theory applied to hybrid fuel cell powered vehicle. In: Proc 15th IFAC. World Congress, Barcelona, Spain, 6 pages
Sciarretta A, Guzzella L (2007) Control of hybrid electric vehicles. IEEE Control Syst Mag 27(2):60–70
Sciarretta A, Back M, Guzzella L (2004) Optimal control of parallel hybrid electric vehicles. IEEE Trans Control Syst Technol 12(3):352–363
Seierstad A, Sydsæter K (1987) Optimal control theory with economic applications. Advanced textbooks in economics, vol 24. Elsevier, Amsterdam
Serrao L, Sciarretta A, Grondin O, Chasse A, Creff Y, di Domenico D, Pognant-Gros P, Querel C, Thibault L (2011) Open issues in supervisory control of hybrid electric vehicles: a unified approach using optimal control methods. In: Les rencontres scientifiques d'IFP energies nouvelles internat scient conf hybrid and electric vehicles, Rueil-Malmaison, France
Tate ED, Boyd SP (2000) Finding ultimate limits of performance for hybrid electric vehicles. In: Hybrid electric vehicles (SP-1560), Costa Mesa, CA, SAE paper 2000-01-3099
Vinter R (2000) Optimal control. Systems & control: foundations & applications. Springer, New York
Wei X, Rizzoni G (2001) A scalable approach for energy converter modeling and supervisory control design. In: Proc ASME IMECE
Willems JC (1996) The birth of optimal control. In: Proc IEEE conf decision and control. IEEE, Kobe, pp 1586–1587
Zak SH (2003) Systems and control. Oxford series in electrical and computer engineering. Oxford University Press, New York

Chapter 5
Numerical Solutions for Known Trajectories

5.1 Introduction on Numerical Solutions

A major benefit of hybrid vehicles is the ability to recover energy during braking or driving downhill. The recovered energy can be stored in the battery and deployed at a later time to assist the prime mover to provide tractive power. On routes with high energy recovery potential, e.g., when driving in the city, the stored energy can be deployed relatively fast to avoid overcharging of the battery. On the other hand when vehicles are driving on a free and flat motor-way, where the recovery potential is low, the recuperated energy can be used deliberately such that the battery is not depleted and the discharge losses remain low.

So, apparently, the optimal control policy depends on the characteristics of the drive cycle. To compute the optimal control sequence it is thus required to know the power and velocity requests in advance. This conclusion can also be drawn from the analytical solution for the powersplit problem for hybrid vehicles, obtained in Chap. 4. Here, the optimal control, see (4.10), depends explicitly on the power requests and engine velocity, i.e., φ_1 and φ_2 are a function of P_r and ω.

The model used for the analytical solution in Chap. 4 is rather limited, however; it does not include control constraints, or the inequality constraints on the battery state-of-energy. Also, the component descriptions are simplified compared to the models discussed in Chap. 2, for instance battery state dependent losses are not included. A more involved model is described by (4.36)–(4.43). For this model we were able to derive necessary conditions of optimality in the form of a static optimization of the Hamiltonian, and a differential equation and jump conditions on the costate. So far, a solution in the form of an explicit description of the optimal control and state trajectory is not provided.

In this chapter we will develop the theory needed to compute the optimal control trajectory for prescribed power and velocity trajectories. To go from the analytical results to optimal control trajectories requires in general a numerical approach. This chapter presents two numerical methods for the powersplit problem.

Before we go into the numerical approaches, let us first give a motivation for finding the optimal control trajectory. Obtaining a numerical solution can be of interest

B. de Jager et al., *Optimal Control of Hybrid Vehicles*, Advances in Industrial Control,
DOI 10.1007/978-1-4471-5076-3_5, © Springer-Verlag London 2013

for several reasons. The global optimal powersplit trajectory for known trajectories can be used:

- To evaluate the fuel reduction potential of a hybrid vehicle. The optimal topology and component size of electric machine, engine, and of battery capacity, can be investigated by, repeatedly, computing the fuel reduction potential for each configuration. Due to the interdependency of the component sizes and topology with the control algorithm, the optimization requires evaluation of the global optimal control. The search space for all topologies and component sizes might be very large, this asks for a computational efficient method.
- To evaluate and benchmark real-time controllers. Comparing the real-time strategy, on particular drive cycles, with the global optimal solution, provides a good measure for the quality of the real-time strategy (real-time strategies are later developed in Chap. 6). For this application, accuracy might be of greater importance than computational time.
- To compute the optimal control based on predicted future power and velocity requests. Knowledge of the future optimal powersplit, based on predicted trajectories, can improve the optimality of the decision for the powersplit at the current time. Given the limited computational power and storage capacity of the in-vehicle Electronic Control Unit (ECU), strict requirements regarding the computational load and memory are imposed.

In summary, fast and accurate computation of the optimal powersplit trajectory, based on predefined velocity and power trajectories, is useful. Depending on the application, one criteria might be preferred over the other.

Numerical solutions for optimal control problems often fall into two categories, direct methods and indirect methods.

Firstly, indirect methods use additional costate information to derive the optimal solution using a three step procedure; as a first step the system dynamics are adjoined with a costate variable to the objective function to form the Hamiltonian function. Next, Pontryagin's Minimum Principle (PMP) is used to derive necessary conditions for optimality in the form of a differential equation on the costate variable and the static optimization of the Hamiltonian function, as is outlined in detail in Chap. 4. These analytical results allow to write the optimal control problem $\mathscr{P}_1$, see Sect. 3.7, into a boundary value problem. As a second step, which we will discuss in this chapter, the remaining boundary value problem can then be solved numerically using information about the state and costate at the boundaries. Solving problem $\mathscr{P}_2$ requires a third step in which the touching points of the state with the state boundaries are found, e.g., using a recursive scheme, hereby fulfilling the jump conditions on the costate. One advantage of the indirect method over other numerical approaches is that it does not require quantization of the state and control variables.

Secondly, direct method solvers require only information given by the initial optimal control problem, i.e., information regarding the system dynamics, the objective function, and the control and state constraints, so without the need for costate information. A well known direct solver which is often applied to the powersplit problem

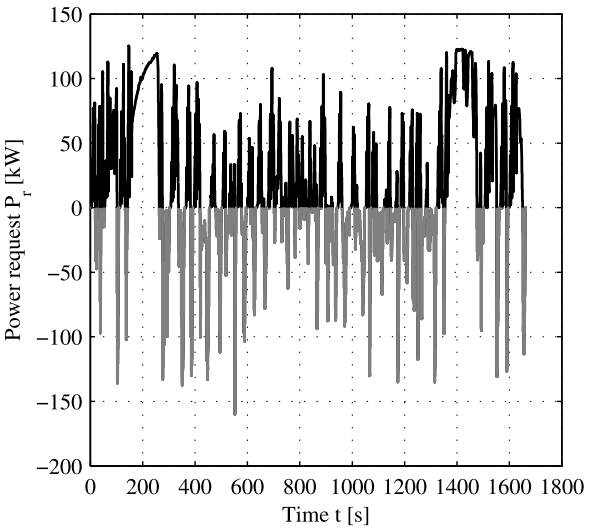

Fig. 5.1 Power request input trajectory as a function of time. The power request is reconstructed from torque and velocity measurements at the drum of a chassis dynamometer, where a 9×10^3 [kg] truck is controlled to follow the FTP-75 cycle with added elevations. Requests for tractive power are in *black*, while in *gray* are the negative power request that can be used for energy recuperation

for hybrid vehicles is the Dynamic Programming (DP) algorithm. The DP algorithm takes advantage of Bellman's Principle of Optimality, and is able to deal with even more involved models than the indirect method such as mixed state-control constrained problems, see $\mathscr{P}_3$ in Sect. 3.7, and it can deal with non-convexity of the objective function. On the other hand, DP is computationally more heavy and the required quantization of state and control variables reduces the accuracy. So, application of DP introduces the classical trade-off between computational demand versus accuracy of the solution.

5.2 Power and Velocity Trajectories

This section provides an example of predefined power and velocity trajectories. This example is used to illustrate the techniques outlined in later sections.

The vehicle used in this simulation example is a hybrid electric truck with a gross vehicle weight of 9×10^3 [kg]; the parameters are given in Table 2.1. The engine map, electric machine, and storage device characteristics are also depicted in Figs. 2.5 to 2.11.

The predefined power, velocity and elevation input trajectories which are used to compute the optimal powersplit trajectory are displayed in Figs. 5.1, 5.2 and 5.3. The elevation profile is added to obtain an input trajectory that requires the control to use the complete operating range of the battery, i.e., to ensure that the state boundaries are reached at some point of the route. These data are obtained from chassis

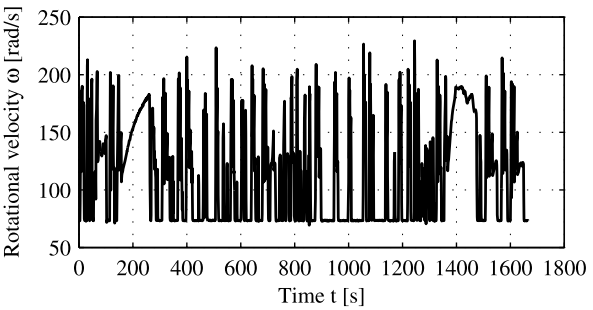

Fig. 5.2 Rotational velocity of the engine and electric machine as a function of time. Start–stop functionality is not implemented in this vehicle, so we can recognize the idle speed of 70 [rad/s]

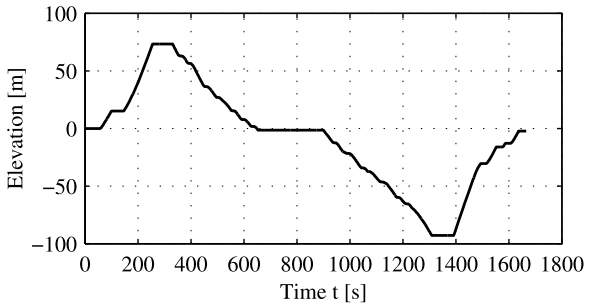

Fig. 5.3 Route elevation, supplemented to the FTP-75 route, as a function of time. The *middle* part of the route has a large recovery potential with two subsequent descents

dynamo meter measurements with the hybrid electric truck at the Federal Test Procedure (FTP), see Fig. 2.18, with added elevations. The power was reconstructed from torque and rotational velocity measurements at the dynamo drum. The measured data are corrected for rolling resistance and drivetrain losses such that they represent the power requests at the crankshaft. The velocity depicted in Fig. 5.2 is directly measured at the crankshaft, therefore, the gear shift strategy can be excluded from the powersplit optimization.

5.3 Indirect Solution Based on a Boundary Value Problem Description

We will now develop a numerical solution for the optimal control problem with control constraints $\mathscr{P}_1$ and the state constrained optimal control problem $\mathscr{P}_2$ which are introduced in Chap. 3. A solution for problem $\mathscr{P}_3$ is not presented in this section but is found in Sect. 5.4, where a direct solution method is outlined.

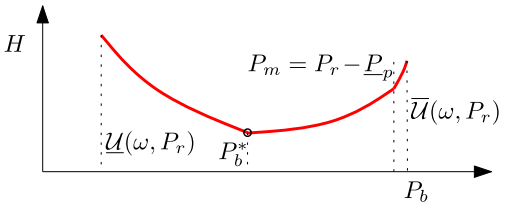

Fig. 5.4 The Hamiltonian function. The optimal control P_b^* is the minimizer of H. Typically, the Hamiltonian is non-smooth in the point $P_m = P_r - \underline{P}_p$, see Fig. 2.3. The function interval is determined by $\underline{\mathscr{U}}$ and $\overline{\mathscr{U}}$ that depend on the predefined trajectories ω and P_r

5.3.1 Control Constrained Solution

Here, we start with the numerical solution for the optimal control problem with control constraints of the form $\mathscr{P}_1$. From the analytical results of Chap. 4, it is possible to define a two point Boundary Value Problem (BVP). The BVP consists of the differential equations on the state and costate. The stored energy at the initial and end time define the two boundary conditions. To keep the notation short, the extraneous inputs ω and P_r are dropped. The BVP is given by

$$\mathscr{P}_{\mathrm{BVP}} \begin{cases} \dot{E}_s(t) = -I_s^2\big(t, E_s, P_b(E_s, p)\big)R - P_b(t, E_s, p), \\ \dot{p}(t) = p(t)\dfrac{\phi U_{\mathrm{oc}}(t, E_s)}{2R}\left[2 - \dfrac{\sqrt{U_{\mathrm{oc}}^2(t, E_s) - 4RP_b(t, E_s, p)}}{U_{\mathrm{oc}}(t, E_s)}\right. \\ \qquad\qquad \left. - \dfrac{U_{\mathrm{oc}}(t, E_s)}{\sqrt{U_{\mathrm{oc}}^2(t, E_s) - 4RP_b(t, E_s, p)}}\right], \\ E_s(t_0) - E_s^0 = 0, \\ E_s(t_f) - E_s^f = 0, \\ t_0 \le t \le t_f. \end{cases}$$

Here, I_s is given by (2.16), P_b depends on E_s and p using the analytical solution for the minimization of the Hamiltonian function given by (4.47), E_s^0 is the initial state, E_s^f is the desired final state. Note that problem description $\mathscr{P}_{\mathrm{BVP}}$ states $\mathscr{P}_1$ in another form since the optimization of the fuel cost over the complete trajectory is replaced by an additional differential equation and a static optimization.

Let us take a closer look at the Hamiltonian function. It can be shown that, with the model (4.36) to (4.43), the Hamiltonian is a (strictly) convex function in the control variable P_b, see Fig. 5.4. This convexity property is important because it results in a monotonic decreasing relation between control variable P_b and costate variable p. Later, this property ensures us that the optimal solution is unique and the numerical methods will converge to this optimal solution.

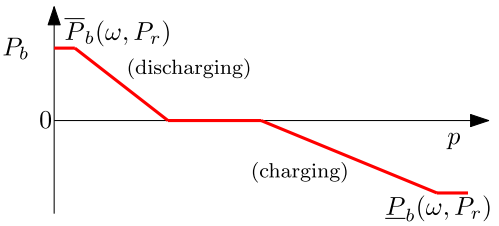

Fig. 5.5 Monotonic decreasing relation between the costate variable p and control variable P_b. Here, P_b ranges between $\overline{P}_b$ and $\underline{P}_b$. Taking into account the non-smoothness in the relation $P_f(P_b)$ we obtain a dead zone: for a range of p the control $P_b = 0$

The monotonic decreasing function $P_b(p)$ is obtained by solving (4.47) for a range of p and the two sets of parameters for the electric machine and is schematically depicted in Fig. 5.5. The optimal control P_b is saturated on the boundary of the interval $\mathscr{U}(\omega, P_r)$ in case the minimizer of H is outside the interval, i.e., when the control constraints are active. For example, the bound $P_f \geq 0$ results in the obvious solution that for sufficiently large negative power requests $P_r \ll 0$ the optimal control is such that $P_m = P_r$, unless P_m is bounded.

With the monotonic decreasing function $P_b(p)$, it follows that an optimal state and costate trajectory for the BVP exist. This optimal trajectory cannot be directly computed, however. Rather, as intermediate step, the solution for an Initial Value Problem (IVP) is searched:

$$\mathscr{P}_{\text{IVP}} \begin{cases} \dot{E}_s(t) = -I_s^2\big(t, E_s, P_b(E_s, p)\big)R - P_b(t, E_s, p), \\ \dot{p}(t) = p(t)\dfrac{\phi U_{\text{oc}}(t, E_s)}{2R}\left[2 - \dfrac{\sqrt{U_{\text{oc}}^2(t, E_s) - 4RP_b(t, E_s, p)}}{U_{\text{oc}}(t, E_s)}\right. \\ \qquad\qquad \left. - \dfrac{U_{\text{oc}}(t, E_s)}{\sqrt{U_{\text{oc}}^2(t, E_s) - 4RP_b(t, E_s, p)}}\right], \\ E_s(t_0) = E_s^0, \\ p(t_0) = p^0, \\ t \geq t_0, \end{cases}$$

in which the condition $E_s(t_f) - E_s^f = 0$ in $\mathscr{P}_{\text{BVP}}$ is replaced by the initial condition on the costate $p(t_0) = p^0$.

Using a strictly convex description of the Hamiltonian function it can be shown that a solution for $\mathscr{P}_{\text{IVP}}$ can be found; denoted $p(t; p^0)$. Solving the BPV as an IVP, using the method of a single guess p^0 for $p(t_0)$, is known as single shooting. Other, more involved, methods for solving a BVP are known, e.g., collocation or multiple shooting (Ascher et al. 1988, p. 175).

Analytical solutions for the differential equations $\dot{E}_s$ and $\dot{p}$ generally do not exist. Therefore, we have to apply numerical methods to solve the IVP. Let us approximate $\mathscr{P}_{\mathrm{IVP}}$ by the discrete time problem with equidistant time samples using the Euler scheme for numerical integration:

$$\mathscr{P}_{\mathrm{EUL}}\begin{cases} E_s(k+1) = E_s(k) - \left[I_s^2\big(k, E_s, P_b(E_s, p)\big)R + P_b(k, E_s, p)\right]\Delta t, \\ p(k+1) = p(k) + p(k)\dfrac{\phi U_{\mathrm{oc}}(k, E_s)}{2R}\left[2 - \dfrac{\sqrt{U_{\mathrm{oc}}^2(k, E_s) - 4RP_b(k, E_s, p)}}{U_{\mathrm{oc}}(k, E_s)}\right. \\ \qquad\qquad \left. - \dfrac{U_{\mathrm{oc}}(k, E_s)}{\sqrt{U_{\mathrm{oc}}^2(k, E_s) - 4RP_b(k, E_s, p)}}\right]\Delta t, \\ E_s(0) = E_s^0, \\ p(0) = p^0. \end{cases}$$

Here, the discrete time sample moments are indicated by variable $k = [0, \ldots, n-1]$ with length $n \in \mathbb{N}$ defined by the length of the prescribed velocity and power trajectories $t_f - t_0$ with equidistant step size Δt:

$$n = \left\lceil \frac{t_f - t_0}{\Delta t} \right\rceil. \tag{5.1}$$

More advanced numerical integration methods than the Euler scheme are known, i.e., Runge–Kutta schemes that incorporate derivative information, see Ascher et al. (1988).

The solution of $\mathscr{P}_{\mathrm{IVP}}$, $p(t; p^0)$, solves also problem $\mathscr{P}_{\mathrm{BVP}}$ if the initial condition p^0 is chosen to satisfy the boundary condition $E_s(t_f) - E_s^f = 0$. The BVP can thus be solved if we find a root for the nonlinear function:

$$\mathscr{P}_{NL}\left\{\psi\big(p^0\big) \equiv E_s(n) - E_s^f = 0.\right.$$

Too small estimates of p^0 will result in depletion of the storage device and the end-point error $\psi > 0$. Too large estimates of p^0 will result in overcharging of the storage device and hence $\psi < 0$. Again, it can be shown that a unique solution for $\psi(p^0) = 0$ exists provided that the Hamiltonian function is strictly convex. The relation $\psi(p^0)$ is schematically depicted in Fig. 5.6. Since the numerical approach hinges on the PMP and we assumed a strictly convex Hamiltonian function, we have $p^0 > 0$.

A root finding algorithm is required to find p^0 that solves $\mathscr{P}_{NL}$. A straightforward root finding algorithm is the bisection algorithm:

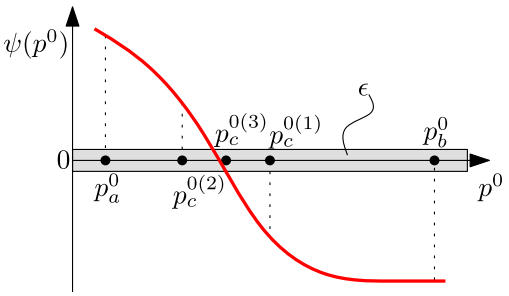

Fig. 5.6 Sketch of the nonlinear and non-convex relation between the initial value of the costate variable p^0 and the error of the end state given by $\psi(p^0)$ which has a single root. The root of $\psi(p^0)$ can be approximated by, e.g., a bisection algorithm for which the first three iterations are illustrated

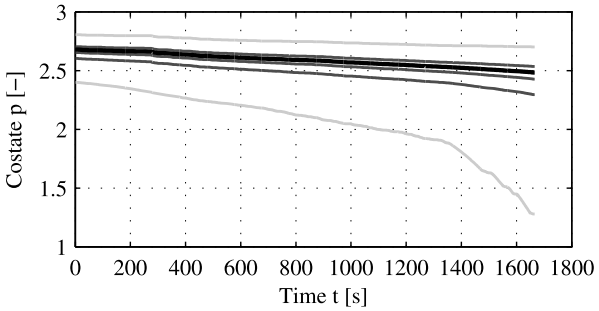

Fig. 5.7 Costate trajectories resulting from several bisection iterations. In *light gray* are the trajectories resulting from initial guesses p_a^0 and p_b^0, in *medium gray* the trajectories of the intermediate iterations, and in *black* the optimal costate trajectory fulfilling $|\psi| < \epsilon$

Bisection algorithm: The root $p^0 \in [p_a^0, p_b^0]$ such that $|\psi(p^0)| = 0$ can be approximated with error ϵ using the following sequence:
compute:

$$p_c^0 = \frac{p_a^0 + p_b^0}{2}$$

repeat

$$p_a^0(i+1) = p_a^0(i), \qquad p_b^0(i+1) = p_c^0(i), \qquad \text{if } \psi\left(p_c^0(i)\right)\psi\left(p_a^0(i)\right) < 0$$

$$p_a^0(i+1) = p_c^0(i), \qquad p_b^0(i+1) = p_b^0(i), \qquad \text{if } \psi\left(p_c^0(i)\right)\psi\left(p_b^0(i)\right) < 0$$

$$p_c^0(i+1) = \frac{p_a^0(i+1) + p_b^0(i+1)}{2},$$

until $|\psi(p_c^0(i+1))| < \epsilon$

Here, for each function evaluation $\psi(p^0)$ for a given $[p_a^0, p_b^0]$, $\mathscr{P}_{\text{EUL}}$ is integrated numerically. The bisection method is globally convergent for continuous

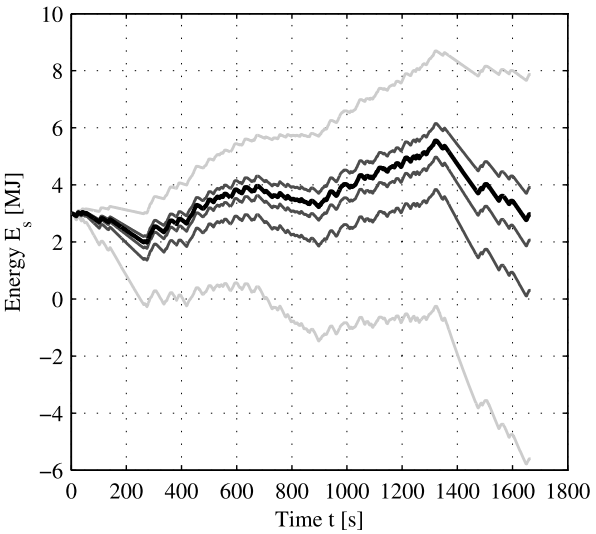

Fig. 5.8 The state trajectories resulting from several bisection iterations. In *light gray* are the trajectories resulting from initial guesses p_a^0 and p_b^0, in *medium gray* the trajectories of the intermediate iterations, and in *black* the optimal state trajectory fulfilling $|\psi| < \epsilon$. Note that the segments where energy recovery is possible are identical for all solutions. The differences arise in the segments where the battery is discharged

Table 5.1 Bisection parameters

Name	Description	Value	Unit
E_s^0	Initial condition of the state	3.0	[MJ]
E_s^f	End-point condition of the state	3.0	[MJ]
p_a^0	Initial guess costate	2.4	–
p_b^0	Initial guess costate	2.805	–
ϵ	Allowed end-point error	0.1	[MJ]

functions for which a solution exists, meaning that $|\psi(p_c^0(i+1))| \to 0$ for $i \to \infty$, see Quarteroni et al. (2000). Other, more advanced root finding algorithms can be applied, e.g., the secant method or Newton's method. Typically, these methods require less function evaluations to reach accuracy ϵ. However, each function evaluation might require more computational power to find information regarding the derivative of $\psi(p^0)$.

An example of solving the powersplit BVP with the method outlined in this section, is given in Figs. 5.7 and 5.8. Here, the power and velocity trajectories of Figs 5.1 and 5.2 and vehicle parameters of Table 2.1 are used as input. The bisection settings are displayed in Table 5.1. The bisection algorithm provides the

initial condition of the costate, $p(t_0)$, see Fig. 5.7. It can be seen that the costate trajectory is a monotonic decreasing function of time which agrees with our earlier observation that $\dot{p} \leq 0$ for all t, see (4.51). Figure 5.8 shows that the state trajectory quickly converges in four iterations to the end point constraint E_s^f with accuracy $\epsilon = 0.1$ [MJ].

5.3.2 State Inequality Constrained Solution

In the previous section, the observations obtained from the necessary conditions of optimality for problems of type $\mathscr{P}_1$ are used to construct a two point boundary value problem which, using an initial value problem description as intermediate step, can be solved with a root finding algorithm such as bisection.

The necessary conditions for state constrained optimal control problems, i.e., of type $\mathscr{P}_2$, are much more involved as we have seen in Sect. 4.2.5. Besides the differential equation on p, we obtain also a jump condition on p. Since a priori the location and number of jumps as well as the height of each jump is unknown, the boundary value problem is not well defined anymore. Nevertheless, some information can be obtained from the PMP; the direction of the jump is known. This directionality property is exploited in this section to find also the global optimal powersplit trajectory in case state-of-energy boundaries of the battery are active.

In this section, an algorithm is presented that rewrites the constrained optimal control problem $\mathscr{P}_2$ as a sequence of optimal control problems without inequality constraints on the state, i.e., of the form $\mathscr{P}_1$ which can be solved using the solution developed in Sect. 5.3.1. For more details on the algorithm for (scalar) optimal control problems with inequality constraints on the state, including a proof for optimality, consult van Keulen (2011).

The procedure is briefly outlined:

- The unconstrained optimal state (and costate) trajectory is calculated.
- If state constraints are exceeded, the problem is split into two subproblems at the sample time where the unconstrained solution exceeds the state constraint the most.
- The subproblem for the interval prior to the sample time where the split occurred, has an endpoint constraint at the boundary that is reached, while the subproblem for the interval after the sample time where the split occurred has an initial condition at the boundary.
- This procedure is repeated until none of the sub-trajectories exceeds a bound (recursion).

This procedure can be executed with the algorithm described in the gray box below.

Table 5.2 Fuel consumption results of the constrained optimal solution compared to the baseline and unconstrained optimal solution

Strategy	E_f [MJ]	E_f %
Baseline (engine only)	160.1	100.0
State unconstrained optimal solution	135.7	84.78
State constrained optimal solution	135.9	84.88

State constrained solution algorithm: The optimal multiplier p^* and state E_s^* trajectories for the state constrained optimal control problem of the form $\mathscr{P}_2$ are found by the following sequence:

- compute the unconstrained optimal solution, i.e., solve the two point boundary value problem $\mathscr{P}_{\text{BVP}}$, if a state constraint is exceeded,

  repeat
- find the instant τ_i where the state boundary is exceeded the most,

$$\tau_i = \arg \max_{k \in [k_a k_b]} \left(\underline{E}_s - E_s(k), E_s(k) - \overline{E}_s \right),$$

  where k_a and k_b are the initial and final sample time of the sub-trajectory in which the state boundary is exceeded the most, and i is the ith iteration of this recursive scheme,
- split the initial (sub-)trajectory in two sub-trajectories: $[k_a \ \tau_i]$ and $[\tau_i \ k_b]$. Calculate the unconstrained optimal solution at both sub-trajectories using:
  - in case the upper capacity constraint is exceeded $E_s(\tau_i) := \overline{E}_s$ as end point constraint for the interval $[k_a \ \tau_i]$ and as initial condition for the interval $[\tau_i \ k_b]$,
  - in case the lower capacity constraint is exceeded $E_s(\tau_i) := \underline{E}_s$ as end point constraint for the interval $[k_a \ \tau_i]$ and as initial condition for the interval $[\tau_i \ k_b]$,

  until $\max(\underline{E}_s - E_s(k), E_s(k) - \overline{E}_s) \leq 0$ for all $1 \leq k \leq n$.

The algorithm is demonstrated on the same example as used for the unconstrained problem but now using the state inequality constraints $\underline{E}_s = 1.8$ and $\overline{E}_s = 4.1$ [MJ]. The results of the algorithm are displayed in Figs. 5.9 and 5.10. The constrained optimal solution is calculated in three iterations. It can be seen that the unconstrained solution, which was computed in the previous section, exceeds the upper state constraint the most. Therefore, the first iteration has a contact point on the upper bound. In one of the sub-trajectories the lower constraint is exceeded, thus a second iteration is required. In Fig. 5.9 the optimal costate values are depicted. It can be seen that the costate has a jump at the instants that the boundary is touched. The calculated costate trajectory fulfills the jump condition, i.e., a downwards jump is observed in case the lower bound is touched, while a jump upwards is seen when the upper bound is touched. Table 5.2 shows the difference in fuel consumption be-

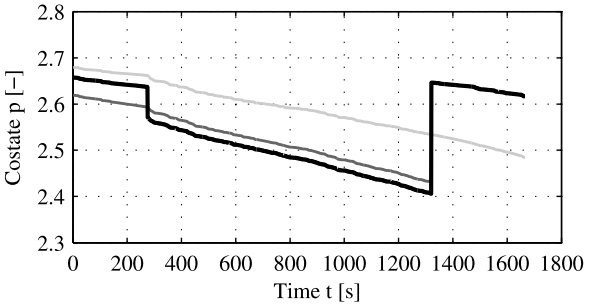

Fig. 5.9 Optimal multiplier trajectory p for the state constrained optimal control problem $\mathscr{P}_2$ with intermediate iterations to achieve constraints. In *light gray* the unconstrained optimal solution, in *dark gray* the intermediate solution, and in *black* the optimal state constrained solution. The multiplier has a negative jump in case the lower constraint is reached, and a positive jump in case the upper constraint is reached

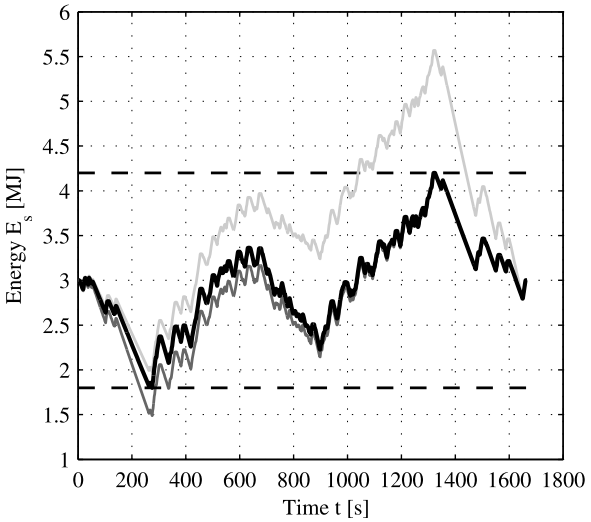

Fig. 5.10 Optimal state trajectory E_s with intermediate iterations to achieve constraints. The *dashed line* indicates the inequality constraints on the state $\overline{E}_s$ and $\underline{E}_s$. Clearly, the unconstrained solution (*light gray*) exceeds the upper state constraint. The first iteration (*dark gray*) results in a trajectory that violates the lower state constraint. The second iteration (*black*) provides the global optimal trajectory

tween a non-hybrid reference and the state constrained and unconstrained optimal powersplit solution for the same hybrid vehicle. It can be seen that the difference in fuel consumption between the constrained and unconstrained solution is very small (0.1 %). From this it can be concluded that, as long as the battery bounds are "wide" enough to store the recoverable energy available in route segments and if before a

recovery segment E_s is low enough to allow storage of all recoverable energy, it does not matter too much when this energy is re-used.

5.4 Direct Solution Based on the Dynamic Programming Algorithm

This section provides a direct method to solve the powersplit optimal control problem with state constraints using the Dynamic Programming (DP) algorithm. In DP use is made of Bellman's Principle of Optimality to find optimal state and control input trajectories. This principle states that each individual transition inside an optimal trajectory should be optimal itself. This means that, for a problem in discrete time, it is sufficient to find the optimal trajectories for state and for control inputs in going from any state at sample time k to any other state at sample time $k+1$. By concatenating those optimal solutions for all instants a globally optimal solution is found. In DP implementations, time is discretized and the state and control input are quantized. The set of possible instants is finite and so is the set of possible states and control inputs at each instant. Therefore, the globally optimal solution can be found, in finite time, by an exhaustive search procedure. This procedure may be time consuming, but even problems of type $\mathscr{P}_3$ with mixed state-control constraints, e.g., obtained by including voltage limitations on the battery, see (2.14), can be solved. When the solution is not unique, the algorithm will just pick one of the optimal solutions. Therefore, DP can handle also problems with a non-convex cost function description. The sizes of the quantization and discretization intervals determine the accuracy of the solution and also the computational burden. Those are inversely related. For optimal control problems with only a single state, as in the powersplit problem for hybrid vehicles, the computational expense is quite acceptable, as will become clear from some examples. Several measures are discussed to keep the computational burden as small as possible.

5.4.1 Discretization of the Time, and Quantization of the State and Control Variable

Dynamic Programming involves a discretization of the time, and a quantization of the state and control variables. Recall from (5.1) the number of time intervals n:

$$n = \left\lceil \frac{t_f - t_0}{\Delta t} \right\rceil.$$

The continuous time model of the dynamics (4.31) can be approximated with the discrete time model given by

$$E_s(k+1) = E_s(k) - P_s(k)\Delta t. \tag{5.2}$$

Here, $P_s(k)$ can be based on model description (2.12) to (2.16). However, it is also possible to use more involved model descriptions, e.g., directly based on map-based data presented in Figs. 2.10 and 2.11.

As said before, the DP algorithm also involves quantization of the state variable. Hence, the state variable E_s is restricted to take a value on a finite grid with distance ΔE_s. Due to the state constraints $\underline{E}_s$ and $\overline{E}_s$ it is convenient to consider exactly $m+1$ energy levels in the storage device, with

$$m = \frac{\overline{E}_s - \underline{E}_s}{\Delta E_s}. \tag{5.3}$$

Thus, the time-state grid has size $(n+1) \times (m+1)$.

Moreover, DP requires quantization of the control variable. For an implementation with low computational cost it is beneficial to avoid interpolations and to assume that the time interval and the state and control input quantization levels are compatible, so the next level of the control input will give, in a single time interval, the next level of the state. Then P_s is the most suitable control variable instead of P_b that is used as control variable for the indirect method. Therefore, ΔP_s is chosen as

$$\Delta P_s = \frac{\Delta E_s}{\Delta t}, \tag{5.4}$$

such that interpolation of the operating cost between time-state grid points is not required.

For the DP algorithm it is immaterial if the search procedure goes forward or backward in time. In our case a forward in time procedure is chosen, which delivers the cost-to-arrive at any final battery state $E_s(n)$ given an initial battery state-of-energy $E_s(0)$. This is especially convenient in the computation of the optimal control policy for plug-in hybrids. Plug-in hybrid vehicles drain energy from the battery along the trip. However, it is normally not the case that a plug-in hybrid will end its trip with a completely depleted battery, because at the end a deceleration will occur to bring the vehicle to a stop. The optimal E_s at the end will then be larger than its lower bound. To fix a final $E_s(n)$ level in advance is then inconvenient. On the other hand, hybrid vehicles without facilities to charge from an external source require a charge sustaining control policy, then it is appropriate to define a lower bound on the final battery state equal to the initial battery state, see (3.11).

The feasible operating range of the battery is thus bounded by those trajectories that are possible between an initial energy level of the battery $E_s(0)$ and an end state $E_s(n)$ possibly bounded from below. The feasible area for E_s along the drive cycle is restricted by five individual constraints, i.e., the minimum and maximum value for P_s, the upper and lower bound on E_s, the initial state $E_s(0)$ and possibly a lower bound on the end state $E_s(n)$. Together, they define stricter boundaries on E_s, given by

$$\underline{E}_s^* = \max\left(\underline{E}_s, \underline{E}_s^1, \underline{E}_s^2\right), \tag{5.5}$$

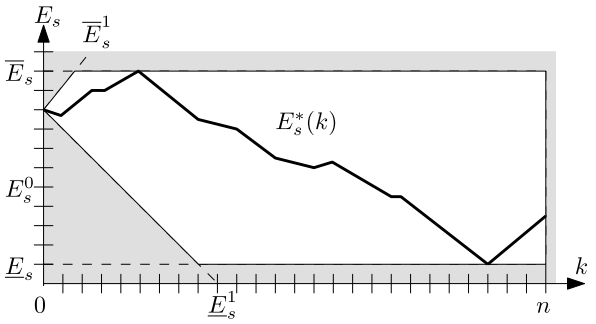

Fig. 5.11 Sketch of the feasible window for the battery energy level of a plug-in hybrid vehicle along the drive cycle. At the initial time the battery is close to fully charged. At the end of the cycle the battery is close to depleted. However, during a final deceleration in the cycle the battery energy stored in the battery is allowed to have an energy level higher than the constraint $\underline{E}_s$

$$\overline{E}_s^* = \min\left(\overline{E}_s, \overline{E}_s^1\right), \tag{5.6}$$

where

$$\overline{E}_s^1(k) = E_s(0) - \sum_{i=0}^{k-1} \min(P_s)\Delta t, \tag{5.7}$$

$$\underline{E}_s^1(k) = E_s(0) - \sum_{i=0}^{k-1} \max(P_s)\Delta t, \tag{5.8}$$

$$\underline{E}_s^2(k) = E_s(n) + \sum_{i=k}^{n-1} \min(P_s)\Delta t. \tag{5.9}$$

The boundaries (5.7) and (5.8) are illustrated in Fig. 5.11. Starting from an initial state $E_s(0)$, it is possible to charge or discharge the battery until one of the boundaries $\overline{E}_s$ or $\underline{E}_s$ becomes active. It is allowed to stay between those boundaries, as long as the end of the drive cycle is sufficiently far away. In the end, it is necessary to return to $E_s(n) \geq \underline{E}_s^2(n)$, so the feasible area of E_s converges according to the limitation (5.9) on P_s.

5.4.2 The Dynamic Programming Algorithm

To describe the implementation of the DP algorithm, we only have to discuss a single step from the search procedure, say from time k to $k+1$. Assume the optimal cost-to-arrive at any level of E_s at time k is known, and is denoted by row vector L. The initial value for L will be 0 for the initial level of $E_s(0)$ and ∞ for all other grid values of $E_s(0)$. Furthermore, there is a cost-to-go column vector U available

at time k which is the fuel power P_f for all grid values of P_s given the external inputs: power request P_r and engine velocity ω for a single interval $k \to k+1$.

$$U = P_f\big(P_s, P_r(k), \omega(k)\big)\Delta t. \tag{5.10}$$

If P_f is a function of the state-of-energy, then U will become a matrix

$$U = P_f\big(E_s, P_s, P_r(k), \omega(k)\big)\Delta t, \tag{5.11}$$

with all costs for the state-input grid space. The entries of U are computed using the relations for the (state dependent) battery, $P_b(P_s)$, electric machine, $P_m(P_b)$, and engine, $P_f(P_r - P_m, \omega)$, from Chap. 2. The control input P_s needs to obey the power limitations of the power converters. Due to the velocity dependent power limitations, at some part of the route the power limitations are more restrictive. Besides the restriction on the power output of the power converters, the control input P_s should respect also the state constraints $\underline{E}_s$ and $\overline{E}_s$ on the storage device in case of Problem $\mathscr{P}_2$, or the voltage constraints $\underline{U}_t$ and $\overline{U}_t$ in case of Problem $\mathscr{P}_3$. Those requirements will provide time dependent bounds on P_s, namely $\underline{P}_s(k)$ and $\overline{P}_s(k)$. The constraints $\underline{P}_s(k)$ and $\overline{P}_s(k)$ are required to match with elements in the input grid. For any value of P_s that is infeasible, so any grid point below $\underline{P}_s$ or above $\overline{P}_s$, the corresponding entry in U is ∞, so the optimal solution will not employ this particular control input, because the costs are too high. Correspondingly, any level of E_s that is not feasible can be avoided by setting the corresponding entry in L, or in U in case of a state dependent battery model, equal to ∞. In general it is easier to percolate the infeasibilities through the chain of computations leading to the cost P_f for all grid points than to find analytical expressions for the bounds on the control variable P_s.

The cumulative cost of all transitions to arrive at time $k+1$, feasible or not, is given by the "element-by-element binary sum" operation for a row vector, L, and the cost-to-go column vector, U,

$$LL = L + U$$

where LL is built up like

$$LL = \begin{bmatrix} L(1)+U(1) & L(2)+U(1) & \cdots \\ L(1)+U(2) & L(2)+U(2) & \cdots \\ \vdots & \vdots & \ddots \end{bmatrix}. \tag{5.12}$$

In case U is a matrix, this matrix will be employed, replacing the entries for U in (5.12). When the ordering in the state and input vector is from low to high values, the matrix LL achieves its highest values in the top-right corner, corresponding to a large E_s and high charging level, $P_s \ll 0$, and its lowest values in the bottom-left

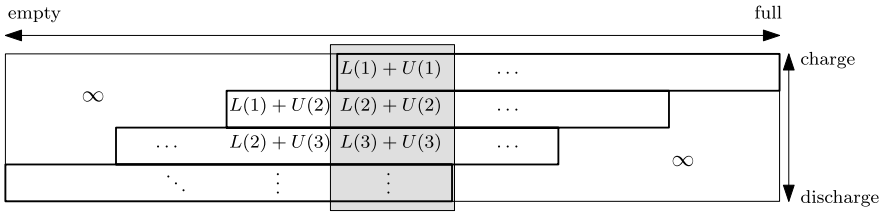

Fig. 5.12 Sketch of the "skewing" procedure of the matrix LL. Horizontally are the quantization levels obtained with a constant control input P_s, the column in the *gray panel* depicts a constant quantization level for E_s. The optimal cost to go to a specific quantization level for E_s is obtained by finding the minimum over all values in the appropriate column, like in the *gray panel*

corner. The resulting state corresponding to the entries in matrix LL has the shape

$$\begin{bmatrix} \ddots & \vdots & \vdots & \vdots & \ddots \\ \cdots & E_s(l) & E_s(l+1) & E_s(l+2) & \cdots \\ \cdots & E_s(l-1) & E_s(l) & E_s(l+1) & \cdots \\ \cdots & E_s(l-2) & E_s(l-1) & E_s(l) & \cdots \\ \ddots & \vdots & \vdots & \vdots & \ddots \end{bmatrix}$$

where l denotes an arbitrary quantization level for E_s. The middle row, corresponding to $P_s = 0$, is not shifted, it just denotes all possible levels for E_s, while rows above that one, corresponding to $P_s < 0$, are shifted to the left because the battery is charged and E_s increases, and lower rows, corresponding to $P_s > 0$, are shifted to the right because the battery is discharged and E_s decreases. Note that an upper right triangle of LL, corresponding to the highest levels of E_s and still charging, and a lower left triangle, corresponding to the lowest levels of E_s and still discharging, are infeasible.

To find the lowest cost to arrive at level l of $E_s(k+1)$, the minimum value on the appropriate diagonals of LL has to be found. This can be done in a loop, but to profit from multi-threaded library functions it may be better to search instead for the minimum of all rows or columns of a newly defined rectangular matrix, say R. This can be done by "skewing" rows of the matrix LL, so the diagonals of LL become column vectors in R, see Fig. 5.12. The left-upper and right-lower triangular corners of matrix R should be padded first.

When the minimum entry of each column in R is found, the optimal values are stored in column L to be used for the next time step. Some of these values may be ∞, indicating an infeasible state level. The optimal transitions, obtained from the indices of the minimum values in R, are also stored. They describe the state level at time k that is the optimal starting point to arrive at a certain state level at time $k+1$. Note that the optimal input P_s can always be obtained from the optimal state trajectory, being found from the difference between a certain state and its optimal predecessor. So, the optimal state trajectories are built up going forward, k to $k+1$, while the optimal control input is reconstructed looking back, $k+1$ to k. The final

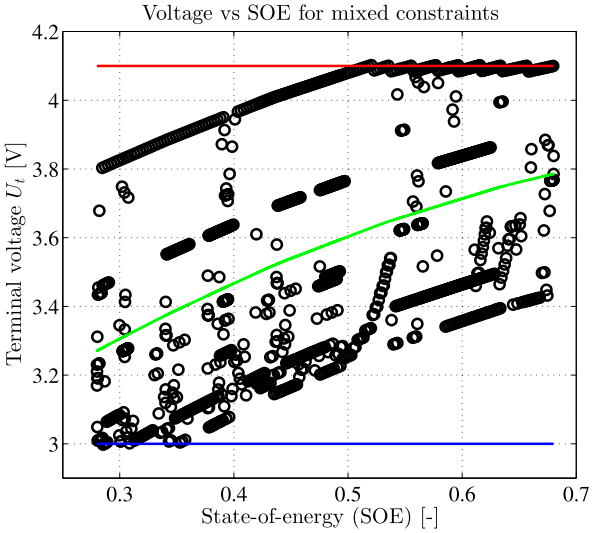

Fig. 5.13 Example solution of DP with mixed state-input constraints. Here, U_{oc} is the nominal voltage in *solid green*, the maximum terminal voltage $\overline{U}_t$ in *red*, the minimal terminal voltage in *blue*, and the optimal control indicated with *black circles*. It can be seen that during both charging and discharging the mixed constraints become active, i.e., the minimum and maximum terminal voltages are reached. Due to the quantization of the control variable, the voltage shows steps along the mixed constraint perpendicular to the nominal voltage

L for $k = n$ represent the cost-to-arrive at any final $E_s(n)$ level from a particular initial $E_s(0)$ level, and should normally be a monotonic increasing function of the E_s level. The stored optimal transitions allow the determination of the optimal state and input trajectories to arrive at any final E_s level starting from a particular initial E_s. The problem is then solved completely, having determined the optimal cost, optimal control input, and optimal state trajectory for all levels of the final state $E_s(n)$. An example of the results of a DP computation with mixed constraints, so for Problem $\mathscr{P}_3$, is shown in Fig. 5.13.

5.4.3 Estimation of the Costate Variable

The DP algorithm discussed above does not require to compute the costate variable. However, it can be of interest to find the optimal costate trajectory, e.g., to bench mark the real-time strategy. Given the necessary conditions of optimality, (4.26), it follows that the first derivative of the Hamiltonian function to the control is zero; $\frac{\partial H}{\partial P_b} = \frac{\partial P_f}{\partial P_b} + p\frac{\partial P_s}{\partial P_b} = 0$, which leads to the following condition on the costate $p = \frac{-\partial P_f}{\partial P_s}$. From the DP solution (on a grid) it is possible to provide bounds on the

costate value by approximating $\frac{-\partial P_f}{\partial P_s}$ with

$$\begin{aligned} &\frac{P_f(k, P_s^*(k)) - P_f(k, P_s^*(k) + \Delta P_s)}{\Delta P_s} \\ &\leq p(k) \\ &\leq \frac{P_f(k, P_s^*(k)) - P_f(k, P_s^*(k) - \Delta P_s)}{-\Delta P_s}. \end{aligned} \tag{5.13}$$

By using one control step ΔP_s above and below the optimal control we get a lower and upper bound for p. In case control constraints are active, then there is no direct relation between $\frac{-\Delta P_f}{\Delta P_s}$ and p.

5.5 Comparison of the Indirect and Direct Method

In this section, the indirect algorithm and the DP algorithm are evaluated on accuracy and computation time.

5.5.1 Accuracy

The optimal constrained trajectory obtained with the indirect approach outlined in Sect. 5.3 is compared on accuracy and computational effort with the DP solution discussed in Sect. 5.4. Besides, different battery models are compared. In Chap. 2, different battery models are presented; a model that has a constant nominal voltage, and a model with a nominal voltage that is increasing with the battery state-of-energy. Here, we will evaluate the influence of battery voltage dependency on the state-of-energy on the accuracy in fuel consumption estimation.

The computed costate and state results, for the input trajectories presented in Figs. 5.1 and 5.2, are depicted in Figs. 5.14 and 5.15. The DP results overlap the results of the indirect method algorithm (red-dashed on top of blue line). The model with battery state dependency has a state trajectory which is slightly higher than the state trajectory resulting from the state independent battery model. It follows from (2.12) that the open-circuit voltage U_{oc} increases with state E_s, thus, a power request P_b at a slightly higher state-of-energy requires a lower current than one at a lower state-of-energy. Therefore, the optimal costate starts at a higher value such that the state-of-energy is directed to higher values.

The accuracy in fuel consumption is depicted in Fig. 5.16. The DP solution is obtained for different grid sizes. Typically, the DP algorithm provides an upper bound in the calculated fuel, by increasing the number of grid points the fuel consumption

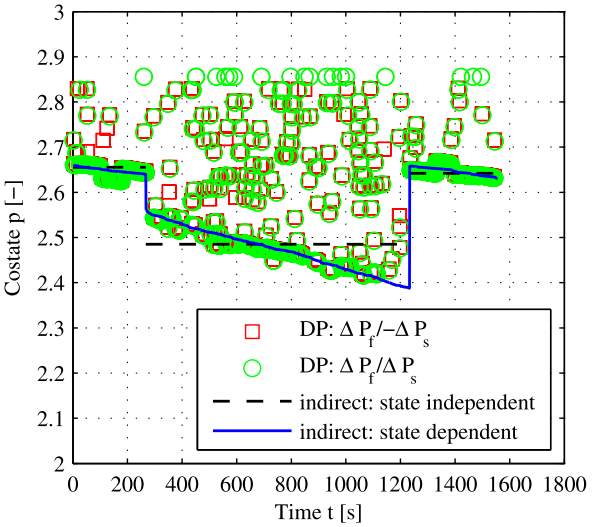

Fig. 5.14 Optimal costate trajectories. The *red squares* indicate the upper bound on the optimal costate computed with DP for the battery state dependent model and the *green circles* the lower bound. The *dashed line* indicates the optimal costate trajectory obtained with the indirect method for the battery model with constant nominal voltage. The *solid line* shows the optimal costate trajectory computed with the indirect method using the battery state dependent model

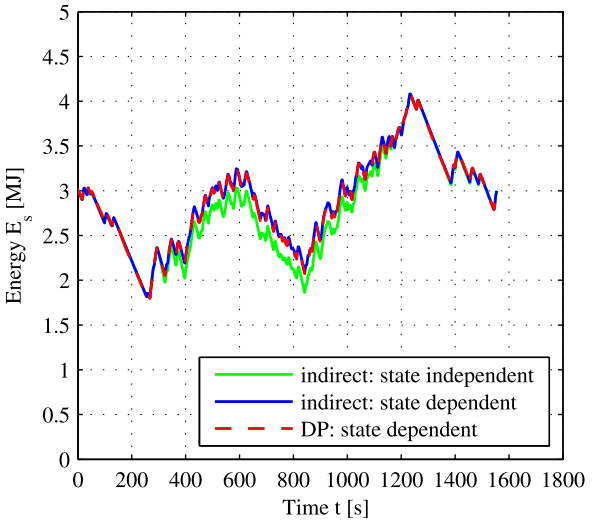

Fig. 5.15 Optimal battery energy trajectories. The results obtained with the indirect method using a state dependent battery voltage (*blue*), and using a state independent battery model with constant voltage (*green*) are compared with the DP solution using a state dependent battery model (*red-dashed*) hereby using a grid size of $\Delta P_s = 1$ [kW]

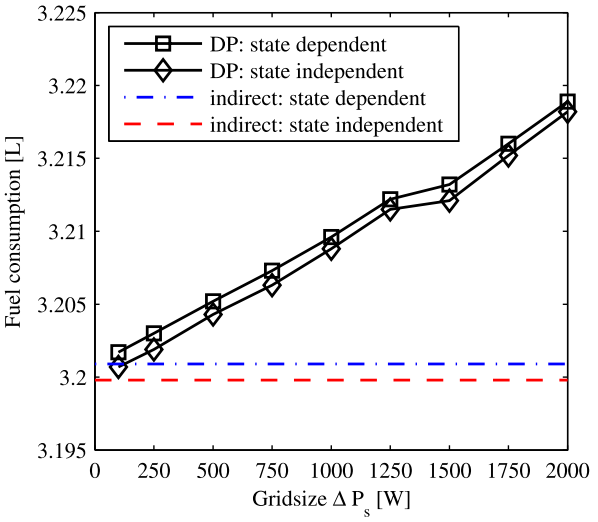

Fig. 5.16 Fuel consumption versus Dynamic Programming grid size. Four different cases are displayed. A state dependent and a state independent solution obtained both with DP (indicated with squares and diamonds, respectively) and the indirect method (indicated with *blue* and *red*). For smaller grid sizes (denser grid) the fuel consumption computed with DP becomes lower since more solutions are available. DP approaches the solution computed with the indirect method for grid sizes that approach 0

lowers due to the increasing number of possible state trajectories. Note that the indirect method solution lies at the point which is expected to be reached if the grid size approaches 0. So, it is concluded that a superior accuracy in fuel consumption (and costate estimation) can be obtained with the indirect method algorithm.

The difference in fuel consumption between the model that accounts for state-of-energy dependent voltage and the state independent model is tiny: <0.05 %. Therefore, it is concluded that neglecting battery state-of-energy dependent losses, for the Li-ion battery used in this example, results in a good approximation of the fuel consumption. For other applications, for instance with super capacitors, where the voltage increase factor ϕ is larger, including state dependent losses could lead to larger differences in fuel consumption.

5.5.2 Computational Effort

The computation times for DP, for different grid sizes, and the indirect approach, both for the state dependent and independent situation, are depicted in Fig. 5.17. All computations where performed on a standard laptop with a 2.00 [GHz] Intel dual core processor using Matlab® (2011a).

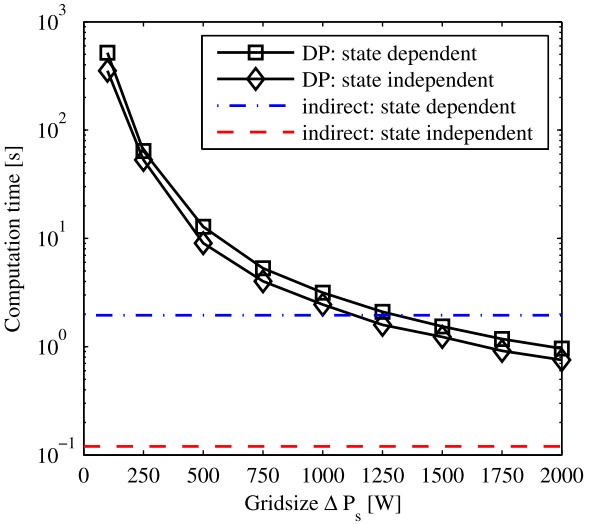

Fig. 5.17 Computation time versus dynamic programming grid size. For smaller grid sizes (denser grid) the computation time for DP increases quadratically. The state dependent battery model is included in the DP algorithm with only a small increase in computation time. The state independent solution (*red-dashed*) is at least an order of magnitude faster than DP

The computation time of the DP algorithm depends on the grid size for the cost-to-go matrix. The computation time of the proposed indirect algorithm depends on the location and the number of times the constraints are reached.

In the worst case the computation time of the indirect method algorithm increases linearly with the number of times a constraint is reached. In general the length of each sub-trajectory reduces after each bound that is reached, such that the computation time increases less than linearly. Moreover, in the worst case the increase of computation time of the indirect method approach is quadratic with the length of the input trajectory, in the best case it grows proportionally.

The computation time of the indirect method algorithm compared to the DP algorithm, for a comparable case with a grid size of 1 [kW] (length $\mathbf{P}_s = 48$ and length $\mathbf{E}_s = 2280$), is of the same order of magnitude in case the state dynamics are accounted for and, at least, one order of magnitude less for the state independent algorithm.

5.6 Case Study: Component Sizing for Hybrid Vehicles

This section provides a case study that demonstrates the algorithm presented in Sect. 5.3 on a component sizing problem. Here, a real-life drive cycle with a length of 513 [km] is used to investigate the effect of the hybridization ratio of heavy-duty vehicles.

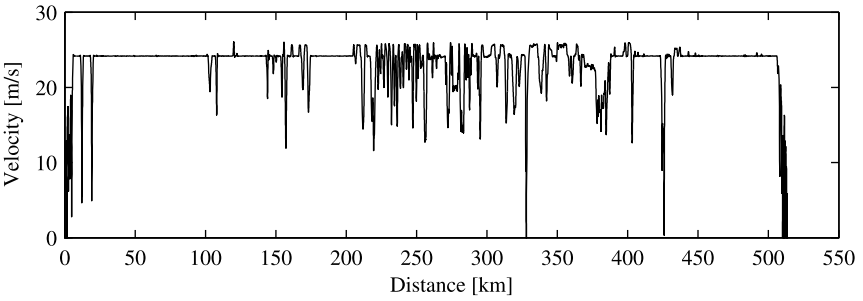

Fig. 5.18 Vehicle velocity versus traveled distance

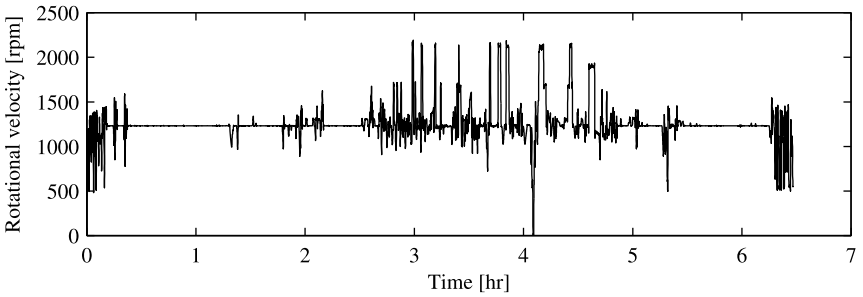

Fig. 5.19 Engine rotational velocity versus time

5.6.1 Introduction to the Case

Although hybrid vehicles offer a fuel economy benefit, the additional cost of an electric machine and especially a battery are considerable. A careful balancing of the expected (fuel) savings and the additional cost is, therefore, required. The optimal component sizing of electric machine and engine maximum power output and of battery capacity is a challenging task. This is due to the interdependency of the component sizes with the control algorithm that governs the powersplit between the engine and the electric machine. Therefore, a fast computation of the optimal powersplit trajectory, based on prescribed velocity and power request trajectories, is useful for the optimization of drivetrain topology and sizing of the components Rizzoni et al. (1999), Filipi et al. (2004), Lukic and Emadi (2004), Hofman et al. (2007), Sundström et al. (2010b), Rotenberg et al. (2011).

In this section, the algorithm presented in Sect. 5.3 is used to derive the fuel optimal engine, electric machine, and battery size for a long-haul truck driving on a highway trajectory in a hilly environment.

The route is driven with a non-hybrid test vehicle with a gross vehicle weight of 40×10^3 [kg] and a maximum engine capacity of 345 [kW]. The measured vehicle velocity and crankshaft velocity are sampled with 1 [Hz] and are shown in Figs. 5.18

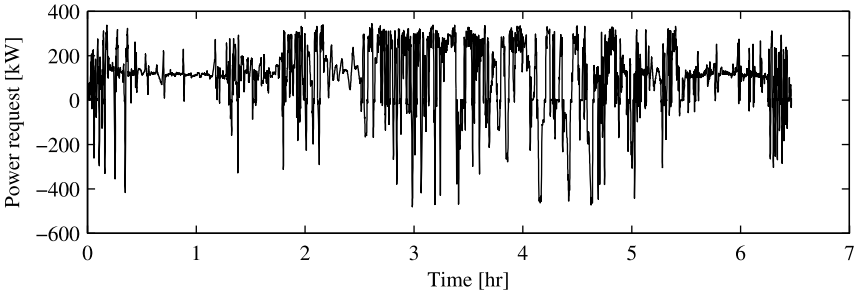

Fig. 5.20 Power request versus time

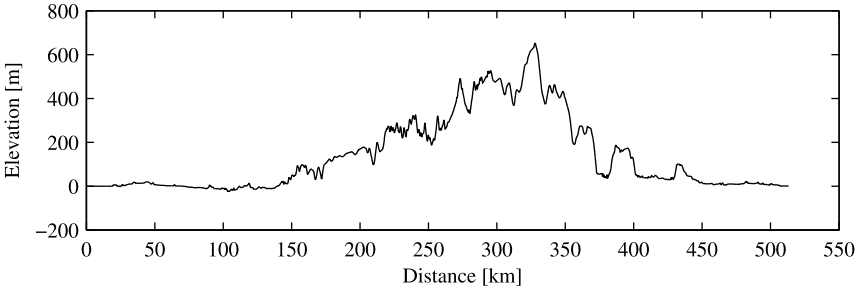

Fig. 5.21 Elevation versus distance

and 5.19. The power request trajectory, see Fig. 5.20, is estimated based on rated engine output of the test vehicle in combination with estimated road load forces based on the velocity and road slope information. The elevation for this trip is depicted in Fig. 5.21. During descents the velocity of the test vehicle increases while coasting ($P_f = 0$), such that the recovery of potential energy is primarily used to acquire kinetic energy.

5.6.2 Component Sizing Results

Next, the effect of hybridizing the drivetrain and downsizing the engine is evaluated. The drag torque of the engine of the test vehicle $\gamma_{p,0}(\omega)$ is known. The incremental cost parameter $\gamma_{p,1}$ is then scaled such that for $P_p = P_r$, P_f according to (2.4), it matches the measured fuel consumption of the test vehicle on the trajectory. By downsizing, the engine parameters $\gamma_{p,0}(\omega)$ and $\gamma_{p,1}$ in (2.4) are kept constant while, obviously, $\overline{P}_p$ is scaled accordingly.

Moreover, it is assumed that the electric machine maximum (dis)charge power matches the battery maximum power throughput. It is assumed that the battery cells are connected in series, such that the battery power and state limitations and open-circuit voltage U_{oc} scale proportionally with the battery capacity (number of cells),

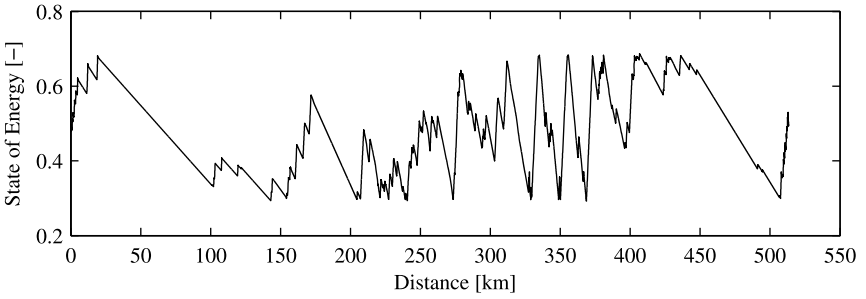

Fig. 5.22 Optimal state-of-energy trajectory versus distance for a hybridization ratio $r_h = 0.18$

while the battery internal resistance also scales proportionally. Furthermore, the electric machine cost is scaled with the maximum electric machine power according to (2.8). For the sake of compactness the effects of the hybridization factor for the engine, electric machine and battery losses are kept simple.

The sizing of the hybrid drivetrain is, therefore, described by a single parameter, the hybridization ratio:

$$r_h = \frac{\overline{P}_m}{\overline{P}_p + \overline{P}_m}, \tag{5.14}$$

the ratio between the electric motor power and the total power of engine $\overline{P}_p$ and electric motor $\overline{P}_m$ combined. Two cases are computed; (i) keep the engine power and add electric power, so $\overline{P}_p = 345$ [kW], and (ii) downsize the engine power for constant combined power of the engine and electric machine, so $\overline{P}_p + \overline{P}_m = 400$ [kW]. In the latter case the total tractive power has to be larger than for the conventional vehicle in order to obtain a feasible solution for the given power trajectory, i.e., in certain parts of the route the maximum torque output becomes the limiting factor.

For this sizing problem, the battery losses are assumed to be state independent, so with constant battery voltage, resulting in a constant costate $\dot{p} = 0$ value. Calculation of the constrained optimal trajectory for the 6.5 [hr] long trajectory required 0.4 to 0.8 [s] depending on the number of times the constraints where hit which ranged from 13 to 20 times. The optimal state-of-energy trajectory, for a hybridization ratio $r_h = 0.18$ is depicted in Fig. 5.22. The fuel consumption as a function of the hybridization ratio is shown in Fig. 5.23. The fuel consumption is decreasing with increasing hybridization ratio.

The absolute fuel consumption reduction potential, for long-haul trucks, is limited. The reduction is approximately 6.6 % for a downsized engine with a hybridization ratio $r_h = 0.275$ ($\overline{P}_p = 290$ [kW], $\overline{P}_m = 110$ [kW]) on the, somewhat hilly, test trajectory. Since the electric machine and engine are not only bounded by power but also by torque, at lower rotational velocities the available torque (and thus power) reduces. Downsizing the engine with a hybridization ratio larger than 0.275 will result in $P_r > P_p + P_m$ for some t, so the problem becomes infeasible.

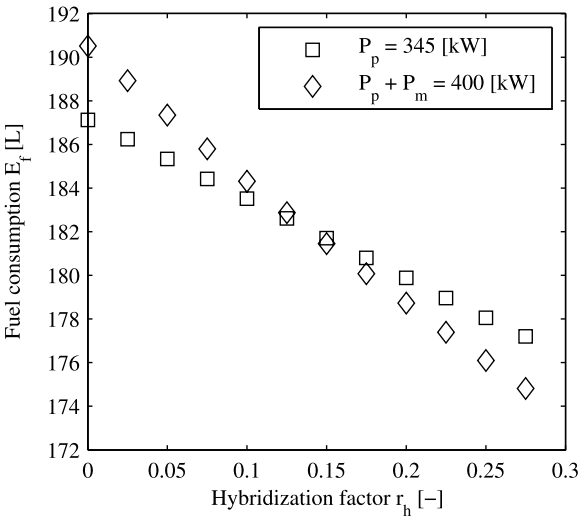

Fig. 5.23 Fuel consumption versus hybridization ratio

Due to the high mileage ($>1\times10^6$ [km]) and fuel consumption (>30 [$\ell/100$ km]) during the lifetime of the heavy-duty vehicle, a hybrid drivetrain might be cost effective. A cost analysis is outside the scope of this case study, however.

5.7 Bibliographical Notes

The powersplit problem for hybrid vehicles can be seen as a general optimal control problem with a scalar state. Numerical solutions for optimal control problems have a long history.

As outlined in this chapter, the Minimum Principle introduced by Pontryagin, see Pontryagin et al. (1962) provides necessary conditions for optimality which allows to rewrite an optimal control problem (without inequality constraints on the state) into a boundary value problem. Numerical solutions for boundary value problems and related issues as stability of the algorithm, can be found in Ascher et al. (1988), Quarteroni et al. (2000), Boyce and Diprima (2003).

One of the first attempts to approach the powersplit problem for hybrid vehicles using an optimal control framework based on Pontryagin's Minimum Principle is by Delprat et al. (2002) in which the necessary conditions of optimality are applied to the powersplit problem for hybrid vehicles with an unconstrained storage device. In van Keulen (2011) the results are extended to also include inequality constraints on the state, state dependent battery losses, and non-smooth cost function descriptions.

Numerical solutions based on the necessary conditions of optimality for problems including inequality constraints on the state (and control) can also be found in, e.g., Gerdts and Kunkel (2008) or Loxton et al. (2009).

Besides indirect methods to solve optimal control problems, other numerical methods that tackle optimal control problems are available, e.g., a direct method

using multiple shooting by Bock and Plitt (1984), Sager (2005), where the original problem is reformulated as a sequence of finite (non)linear programming problems by a parametrization of the controls and states. In Tate and Boyd (2000), the powersplit problem is approximated and rewritten as a linear programming problem, where the power conversion of primary and secondary power converter are approximated with a piecewise affine function.

Dynamic Programming, initiated by Bellman (1957), is another numerical solution method for state constrained optimal control problem. A standard work on Dynamic Programming is Bertsekas (2000). In the context of the powersplit control problem, Dynamic Programming is applied by many researchers. Details on the DP algorithm for hybrid vehicles can be found in Brahma et al. (2000), Kirschbaum et al. (2002), Lin et al. (2003), Koot (2006), Kessels (2007), Sundström et al. (2010a), to name a few references.

References

Ascher UM, Mattheij RMM, Russell RD (1988) Numerical solution of boundary value problems for ordinary differential equations. Prentice-Hall, Englewood Cliffs

Bellman RE (1957) Dynamic programming. Princeton University Press, Princeton

Bertsekas DP (2000) Dynamic programming and optimal control. Athena Scientific, Belmont

Bock H, Plitt K (1984) A multiple shooting algorithm for direct solution of optimal control problems. In: Proc 9th IFAC world Congress, Budapest, Hungary, pp 243–247

Boyce WE, Diprima RC (2003) Elementary differential equations and boundary value problems. Wiley, New York

Brahma A, Guezennec Y, Rizzoni G (2000) Dynamic optimization of mechanical/electrical power flow in parallel hybrid electric vehicles. In: Proc internat symp advanced veh control, Ann Arbor, MI, USA

Delprat S, Guerra TM, Rimaux J (2002) Optimal control of a parallel powertrain: from global optimization to real time control strategy. In: Proc IEEE veh technol conf. IEEE, Birmingham, pp 2082–2088

Filipi Z, Louca L, Daran B, Lin CC, Yildir U, Wu B, Kokkolaras M, Assanis D, Peng H, Papalambros P, Stein J, Szkubiel D, Chapp R (2004) Combined optimisation of design and power management of the hydraulic hybrid propulsion system for the 6 × 6 medium truck. Int J Heavy Veh Syst 11:372–402

Gerdts M, Kunkel M (2008) A nonsmooth Newton's method for discretized optimal control problems with state and control constraints. J Ind Manag Optim 4:247–270

Hofman T, Steinbuch M, Van Druten R, Serrarens A (2007) Rule-based energy management strategies for hybrid vehicles. Int J Elec Hybrid Veh 1:71–94

Kessels JTBA (2007) Energy management for automotive power nets. PhD thesis, Technische Universiteit Eindhoven, Eindhoven, The Netherlands

van Keulen T (2011) Fuel optimal control of hybrid vehicles. PhD thesis, Technische Universiteit Eindhoven, Eindhoven, The Netherlands

Kirschbaum F, Back M, Hart M (2002) Determination of the fuel-optimal trajectory for a vehicle along a known route. In: Proc 15th IFAC world congress, Barcelona, Spain, pp 1–5

Koot M (2006) Energy management for vehicular electric power systems. PhD thesis, Technische Universiteit Eindhoven, Eindhoven, The Netherlands

Lin CC, Peng H, Grizzle JW, Kang JM (2003) Power management strategy for a parallel hybrid electric truck. IEEE Trans Control Syst Technol 11(6):839–849

Loxton R, Teo K, Rehbock V, Yiu K (2009) Optimal control problems with a continuous inequality constraint on the state and the control. Automatica 45:2250–2257

Lukic SM, Emadi A (2004) Effects of drivetrain hybridization on fuel economy and dynamic performance of parallel hybrid electric vehicles. IEEE Trans Veh Technol 53(2):385–389

Pontryagin LS, Boltyanskii VG, Gamkrelidze RV, Mischenko EF (1962) The mathematical theory of optimal processes. Wiley, New York

Quarteroni A, Sacco R, Saleri F (2000) Numerical mathematics. Texts in applied mathematics, vol 37. Springer, New York

Rizzoni G, Guzzella L, Baumann BM (1999) Unified modeling of hybrid electric vehicle drivetrains. IEEE/ASME Trans Mechatron 4(3):246–257

Rotenberg D, Vahidi A, Kolmanovsky I (2011) Ultracapacitor assisted powertrains: modeling, control, sizing, and the impact on fuel economy. IEEE Trans Control Syst Technol 19(3):576–589

Sager S (2005) Numerical methods for mixed integer optimal control problems. PhD thesis, Universität Heidelberg, Heidelberg, Germany

Sundström O, Ambühl D, Guzzella L (2010a) On implementation of dynamic programming for optimal control problems with final state constraints. Oil Gas Sci Technol Rev IFP 65:91–102

Sundström O, Guzzella L, Soltic P (2010b) Torque-assist hybrid electric powertrain sizing: from optimal control towards a sizing law. IEEE Trans Control Syst Technol 18(4):837–849

Tate ED, Boyd SP (2000) Finding ultimate limits of performance for hybrid electric vehicles. In: Hybrid electric vehicles (SP-1560), Costa Mesa, CA, SAE paper 2000-01-3099

Chapter 6
Real-Time Implementable Strategies

6.1 Introduction to Real-Time Implementable Strategies

Hybrid vehicles require an algorithm to govern the powersplit between engine and electric machine. Previous chapters have shown that the optimal powersplit control, which requires the minimal amount of fuel for an arbitrary drive cycle, is completely governed by the costate variable. The optimal costate trajectory can be computed in case the power request for the future drive cycle is exactly known. In practice, the future power request is not exactly known. So, the solutions developed in Chaps. 4 and 5 cannot directly be implemented in the vehicle.

Instead, a causal strategy is required that has no knowledge of the future power requests and uses only information available in the vehicle from the past and the present time. Examples of actual vehicle signals available for the powersplit control are; accelerator pedal position; state-of-energy of the battery; vehicle velocity; and operating conditions of the power converters such as temperature and rotational speed. Available historical data such as recent road slopes and power requests can also be explored by the real-time strategy.

The real-time implementable control policy is in general suboptimal, i.e., when the implemented strategy is evaluated retrospectively with the off-line computed optimal solution, a control sequence that achieves a lower fuel consumption can usually be found. One of the objectives in the design of the real-time implementable strategy is to achieve a fuel consumption that is close to the off-line computed optimal solution. Additional requirements on the real-time strategy are imposed by the limited computational power and storage capacity of the Electronic Control Unit (ECU). Besides, in the automotive industry, the calibration of the implemented strategy is normally done by engineers that have only a basic notion of optimal control theory. It is therefore desirable that the calibration of the implemented strategy is intuitive and does not require a profound understanding of the underlying mathematics.

This chapter discusses powersplit algorithms that do not require exact knowledge of the future power requests, that have a computational burden suitable for real-time

B. de Jager et al., *Optimal Control of Hybrid Vehicles*, Advances in Industrial Control,
DOI 10.1007/978-1-4471-5076-3_6,

implementation, that are easy to calibrate, but still obtain a control policy close to optimal. Two different real-time implementable approaches are discussed:

- Rule-based strategies. These methods are based on a finite set of rules. The rules can, e.g., be based on heuristic considerations.
- Optimal control-based strategies. Using the necessary conditions of optimality, obtained by Pontryagin's Minimum Principle, it is possible to derive a real-time implementable control policy, i.e., an optimal-control-based strategy that consists of real-time optimization of a Hamiltonian-like function and on-line estimation of the costate variable.

These two different approaches will be discussed in detail in the next sections, starting with the rule-based approach.

6.2 Rule-Based Approaches

Strategies based upon 'if-then' type of control rules are known as rule-based strategies. Rule-based strategies require virtually no computational effort or storage capacity and are, therefore, suitable for real-time implementation on the ECU.

The set of rules that achieve a good performance depend strongly on the topology and component characteristics. Here, we will focus on rules for a parallel hybrid topology using the component descriptions presented in Chap. 2. In case of another topology or different component characteristics, one should be aware that the rules below do not necessarily hold.

To derive a set of heuristic rules, let us recapitulate some of the component characteristics. Comparing the component limitations of the internal combustion engine with the electric machine, it can be seen (Figs. 2.5 and 2.7) that the maximum torque lines as function of the rotational velocity are quite different. It is well known that the electric machine can produce a high torque already at low rotational velocity while the engine can produce a relatively low torque at low rotational velocity. Thus, from a drivability point of view, it can be attractive to use the electric machine for vehicle launch.

Furthermore, looking at the energy conversion properties of the battery, electric machine and engine, some observations can be made. The drag losses of both the engine and electric machine are mainly rotational velocity dependent. In case the rotational speed of engine and electric machine is coupled, as in a parallel hybrid topology, the powersplit cannot reduce the friction losses. So, the powersplit decision should be made based on the incremental cost rather than on the absolute conversion cost. Here, the incremental cost of the engine is defined as the slope of the fuel power as function of its output power, and the incremental cost of the electric machine and battery as the slope of the storage energy as function of the power throughput, see Fig. 2.3.

The energy conversion of the engine can often be approximated with an affine relation, see Fig. 2.6, meaning that the incremental cost of the engine is constant.

The conversion losses in the battery and electric machine depend quadratically on the power throughput, see Fig. 2.13, meaning that the incremental conversion cost increase with power throughput. Hence, re-using the recovered and stored energy in the battery with low power is preferred to minimize component losses.

Nevertheless, if the discharge power is chosen too low, we have the risk that the battery is completely charged while brake energy recovery is available. A trade-off has to be made by sufficiently fast discharging to avoid battery overcharging and sufficiently slow to minimize conversion losses. The trade-off is clearly influenced by the drive cycle characteristics, i.e., the available recoverable energy. On a specific cycle, the rule-based strategy can be tuned such that a fuel economy close to the optimum can be obtained. It is much harder to achieve good fuel economy on an arbitrary drive cycle.

For topologies where the drag losses can be influenced by a control action, for instance by engine stop–start functionality, the optimal solution can be very different of nature. At one part of the route the prime mover can provide excess energy which is stored in the battery. Hereafter, the prime mover is shut down and the vehicle drives electric. This avoids the drag losses of the prime mover in the second part of the route.

Keeping the component characteristics in mind, the optimal solutions found in Chap. 5 can be analyzed. It can be seen that energy recovery during braking is always done. Recharging of the battery with the engine is not seen in any of the solutions with the parallel hybrid topology. The stored energy in the battery is re-used at a moderate power as was expected from the quadratic conversion cost relation.

Using a small set of rules based on the observations above, it is relatively easy to setup a real-time implementable strategy. Consult Guzzella and Sciarretta (2005), Pisu and Rizzoni (2007) for an example of a rule-based strategy. The thresholds of the rules can be tuned using off-line computed optimal solutions on a set of drive cycles that represent the operation of the vehicle. However, on top of this set of rules, generally a larger set of rules is required to prevent, e.g., the battery from overcharging or overheating and the electric machine from over-speeding, etc. In practice this results in a long list of rules making the calibration cumbersome.

6.3 Optimal Control-Based Approaches

In the previous section, rule-based strategies are presented as a computationally efficient approach to obtain a real-time implementable powersplit strategy. Moreover, based on a small set of rules one can obtain relatively good results with little effort. Nevertheless, the rule-based strategies become less attractive, from a calibration point of view, in case the number of rules increases. Another difficulty is to obtain robustness against varying conditions such as city driving versus highway driving. In this section it is shown that good robustness with little calibration effort can be found with a strategy that takes advantage of the optimal control results obtained in Chap. 4.

The necessary conditions for optimality, derived in Chap. 4, show that the optimal control can be found at each time instance by static optimization of the Hamiltonian function. Recall that the Hamiltonian function includes a costate variable that adjoins the battery state dynamics to the fuel cost criteria. It can thus be observed that the optimal control is governed by one variable only; the costate. Hence, optimal control-based real-time strategies address the following challenges: (i) to solve the local minimization of the Hamiltonian function with the limited available computational power, and (ii) to compute a suitable estimation of the costate variable by using available real-time information. These two challenges are addressed in the next subsections.

6.3.1 On-line Optimization of the Hamiltonian Function

Real-time computation of the Hamiltonian function, with the limited available computational power, forms the first challenge. In Chap. 4 an explicit solution for the optimization of the Hamiltonian function is derived where the function is approximated as a convex one, allowing for an analytical solution. For convenience the solution is repeated from (4.47):

$$P_b^* = \frac{U_{\text{oc}}^2(\gamma_{p,1}^2 - p^2\gamma_{m,1}^2 + 4p^2\gamma_{m,2}\gamma_{m,0})}{4(R\gamma_{p,1}^2 + p^2U_{\text{oc}}^2\gamma_{m,2})}.$$

Computing this analytical expression consumes little computational effort and is therefore suitable for real-time implementation. The computed control P_b is normally not directly influenced by the power request P_r, so (4.47) is solely governed by costate p and the known component characteristics R, U_{oc}, $\gamma_{m,0}$, $\gamma_{m,1}$, $\gamma_{m,2}$, and $\gamma_{p,1}$ which could depend on real-time measurements of E_s and ω.

Nonetheless, the conversion of fuel into power using the diesel engine presented in Chap. 2 displays non-convex behavior. Furthermore, it can be interesting to include also non-convex operations as clutch operation and idling of the engine in the solution. In case one would like to include such non-convex behavior of the components, a numerical solution for the optimization of the Hamiltonian function is required. This involves for example a gridding procedure, hereby calculating the Hamiltonian value at each grid point and finding the minimizer over all grid points. The suggested gridding-based optimization approach could be solved in real-time. If the computational load is too high, the optimization can be solved also off-line for a range of costate values and relevant component characteristics, and stored in a look-up table. Disadvantage of look-up tables is that the size of the table grows exponentially with the number of dimensions. Storage capacity of the ECU can become an issue, if one likes to include more component characteristics, such as temperature influences or aging.

Figure 6.1 depicts the result of an off-line optimized Hamiltonian function in the form of a look-up table using the component models of Chap. 2. For a total number

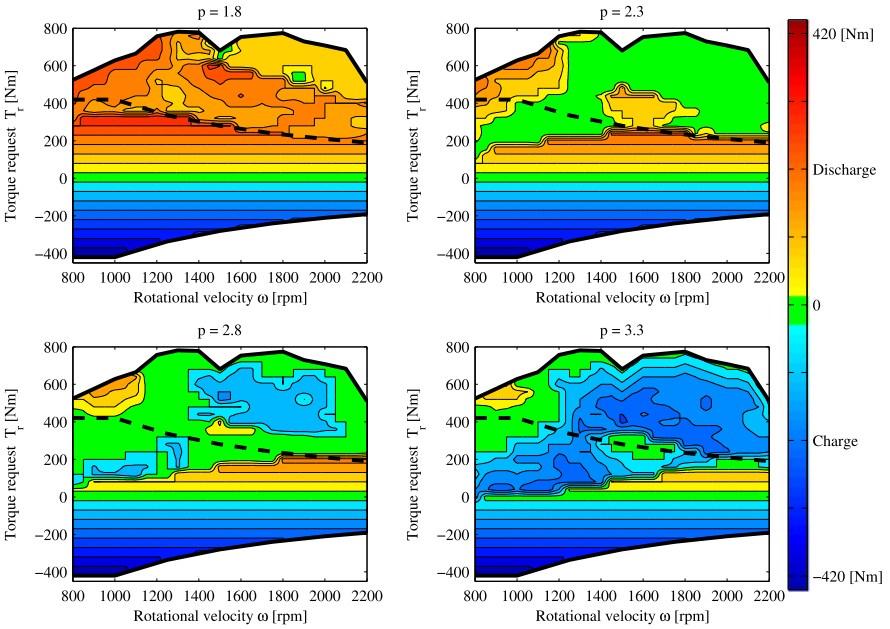

Fig. 6.1 Isocontour plot of electric machine torque T_m [Nm] for various values of the costate p, rotational velocity ω, and torque request T_r. Four subfigures indicate the solution for four of the 17 different costate values p. Each *subfigure* depicts the optimal electric machine torque T_m^* (in *color*) as a function of the electric machine rotational velocity ω_m, and the torque request T_r, with discharging ($T_m^* > 0$) in *yellow/red*, ($T_m^* = 0$) in *green*, and charging ($T_m^* < 0$) in *blue*. Clutch opening ($S = 0$) is indicated by the *colored area* with *horizontal lines* where $T_m^* = T_r$. The *dark solid line* indicates torque limitations, and the *dark dashed line* indicates the electric machine torque limitation with opened clutch. In case of clutch opening, the ICE does idle, it does not stop

of 8704 operating points (16 different rotational velocities, 32 torque requests, and 17 different costate values), the Hamiltonian is constructed locally and the optimal control is calculated. In the implemented strategy, the battery open-circuit voltage and resistance are approximated with a constant, $U_{\text{oc}} = 340$ [V] and $R = 0.32$ [Ω], respectively. The dependency of U_{oc} and R on the state-of-energy could be incorporated in the look-up table, taking more memory.

It can be seen in Fig. 6.1 that for small values of the costate variable, at the upper left subfigure, with $p = 1.8$, electric driving is favored because $T_m^* = T_r$ for $T_r < \overline{T}_m$, almost everywhere, and $T_m^* > 0$ for $T_r > 0$ almost always, especially at engine operating points where the engine incremental cost are relatively high. Looking at the second subfigure, with $p = 2.3$, it can be seen that discharging is preferred less, in fact, the non-smoothness in $P_m = 0$ leads to engine-only fields (in green) for large parts of the operating range. In the lower two subfigures, it can be seen that for increasing costate p, charging the battery is used more and more.

Both the analytical solution (4.47) and the gridding-based solution displayed in Fig. 6.1 require the costate variable as input. All other inputs are measured or known

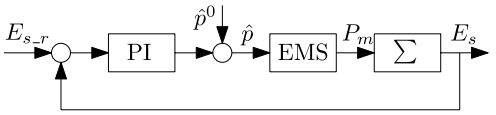

Fig. 6.2 Linear feedback on the state-of-energy to estimate the costate variable $\hat{p}$. Here, E_{s_r} is the reference state-of-energy, $\hat{p}^0$ is the initial guess for the costate, P_m is the electric machine power, and E_s is the energy stored in the battery

at the present time. If, however, P_m exceeds a component limitation, the computed control P_m can be saturated on the relevant boundary. We have

$$P_{m\_r} = \min\big(\max\big[P_m^*, P_m(\underline{P}_s)\big], P_m(\overline{P}_s)\big), \tag{6.1}$$

where P_{m_r} is the resulting electric machine power request which is communicated to a lower level controller, $P_m(P_s)$ the functional inverse of (2.8) and Fig. 2.7, and the control bounds are given by

$$\underline{P}_s = \frac{\underline{U}_R(E_s)}{R} U_{\mathrm{oc}}, \tag{6.2}$$

and

$$\overline{P}_s = \frac{\overline{U}_R(E_s)}{R} U_{\mathrm{oc}}, \tag{6.3}$$

in which $\underline{U}_R$ is the state-of-energy dependent allowable charge over-potential which becomes zero at $\overline{E}_s$, $\overline{U}_R$ the state-of-energy dependent allowable discharge over-potential which becomes zero at $\underline{E}_s$. So, the electric machine power is gradually reduced if a state-of-energy bound (a state inequality constraint) is reached.

6.3.2 On-line Estimation of the Costate Variable

The powersplit is completely governed by the costate variable. The second challenge, for the optimal control-based powersplit strategy, is therefore to find a good estimate for the costate variable p. In the previous chapters it was already mentioned that costate p is closely related to the state-of-energy of the battery. In Sect. 5.3.1 the example shows that a too large costate value results in overcharging of the battery while a too small costate value leads to depletion.

Looking at this observation from a control perspective, a tracking problem can be obtained; govern p such that E_s is kept near a desired trajectory. So, drift of E_s can be avoided by using feedback on the battery state-of-energy to estimate the costate variable, see Fig. 6.2. The feedback of E_s is meant to avoid overcharging or depletion of the battery in the long term. Nevertheless, short term fluctuations of

E_s should still be possible, see Koot et al. (2005). Thus the bandwidth of the PI-controller proposed to control E_s should be chosen rather low. A description of the feedback becomes

$$\hat{p}(t) = \hat{p}^0(t) + K_p\big(E_{s\_r}(t) - E_s(t)\big) + K_i \int_{t_0}^{t} \big(E_{s\_r}(\tau) - E_s(\tau)\big)\,\mathrm{d}\tau, \tag{6.4}$$

here, parameter $\hat{p}$ is the estimated costate at the current time t, $\hat{p}^0$ is an "initial" guess, K_p is the proportional feedback gain, K_i is the integral feedback gain, and E_{s_r} the reference state-of-energy.

Reference E_{s_r} can be chosen constant such that the stored recovered energy is kept near a nominal state-of-energy. However, the vehicle itself, like the battery, can also be seen as a reversible energy storage system (Rodatz et al. 2005). Therefore, the state-of-energy reference E_{s_r} can be corrected for expected future energy recoveries (Van Keulen et al. 2008), by accounting for the current kinetic and potential energy of the vehicle:

$$E_{s\_r}(t) = E^0_{s\_r}(t) - K_E\hat{m}\frac{1}{2}v^2(t) - K_h\hat{m}g_a\int_{t_0}^{t} \sin\hat{\alpha}(\tau)v(\tau)\,\mathrm{d}\tau, \tag{6.5}$$

where $E^0_{s\_r}$ is the preferred reference at zero kinetic and potential energy, K_E a tuning parameter that estimates the, driver dependent, kinetic energy recovery effectiveness, $\hat{m}$ the estimated vehicle mass, v the actual vehicle longitudinal velocity, K_h a tuning parameter estimating the recovery effectiveness of potential energy, g_a the gravitational constant, $\hat{\alpha}$ the estimated road slope. Real-time estimation of $\hat{m}$ based on actual vehicle parameters is possible (Vahidi et al. 2005). An adaptive state-of-energy reference leads to more freedom in the storage device operation since deviations of state-of-energy are only corrected if they are different from the expected kinetic and potential energy recovery.

For charge-sustaining hybrids, the control set point $E^0_{s\_r}$ can be constant and predictive information is not necessarily required, while, for plug-in hybrids, or green-zone entering, a time (or distance) dependent set point is required which involves, at least, information about the distance to the next green-zone or plug-in location, e.g.,

$$E^0_{s\_r}(t) = E^0_s + \frac{E^f_s - E^0_s}{s_{\text{trip}}}s(t), \tag{6.6}$$

where E^f_s is the desired state-of-energy at the end of the cycle, E^0_s the initial state-of-energy, s_{trip} the distance to the next plug-in station or green-zone, and $s(t)$ the distance traveled at time t.

Finally, the strategy based on (6.4) is suited to include predictive information. If geographic information of the route ahead is available, optimization methods can be used to estimate $\hat{p}^0$ and optimal state-of-energy reference trajectory E_{s_r} (see, e.g., Kessels and Van den Bosch 2008; Van Keulen et al. 2010).

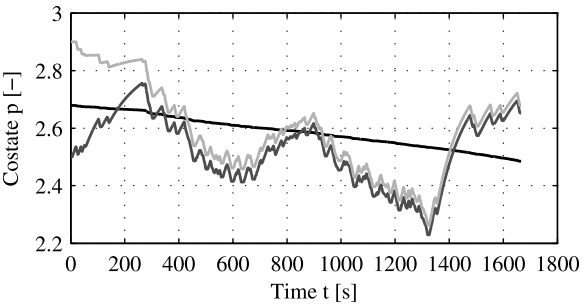

Fig. 6.3 Costate trajectories of the real-time implementable strategy. In *black* the optimal solution, in medium gray the costate trajectory that results from a high initial guess, and in *light gray* the costate trajectory that results from a low initial guess of $\hat{p}$

6.3.3 Example of an Optimal Control-Based Strategy

In this section, the optimal control-based real-time implementable strategy is demonstrated with two examples. First, an example for the case that state-of-energy bounds can be ignored. Second, the case that state-of-energy bounds become active. The examples take use of the same underlying model that is used for the example in Sect. 5.3, i.e., using the velocity and power request trajectories of Figs. 5.1 and 5.2, component models (4.36) to (4.43), and the analytical solution (4.47) for minimization of the Hamiltonian function. Stop–start functionality of the engine or clutch operation is not considered in these examples.

6.3.3.1 Without State Constraints

The feedback parameters $E_{s\_r} = 3$ [MJ], $K_p = 0.01$ and $K_i = 0.2$ are used. Two different settings for $\hat{p}^0$ are evaluated in this example: $\hat{p}^0 = 2.5$ and $\hat{p}^0 = 2.9$. The performance of the real-time strategy, for two different initial guesses $\hat{p}^0$, is shown in Figs. 6.3 and 6.4. In Fig. 6.3 it can be seen that the costate variable shows large deviations from the optimal costate trajectory. Although the initial guess is different, the two real-time strategies converge to the same costate trajectory corresponding to different trajectories in E_s, separated by $\Delta E_s = \Delta \hat{p}^0 / K_p$ if the influence of the integrating action is small compared to the proportional action. Figure 6.4 shows that the deviation of the battery energy state of the real-time strategies compared to the optimal solution remains bounded. Nevertheless, the real-time strategies, using feedback on the battery state-of-energy to estimate the costate variable, obtain a fuel consumption close to the optimum, see Table 6.1. Tuning rules for K_p and p_0 are further discussed in the case study presented in Sect. 7.2.3.

6.3.3.2 With State Constraints

In this second example, the effect of state constraints on real-time strategies is demonstrated. Two real-time strategies are compared with the baseline vehicle and

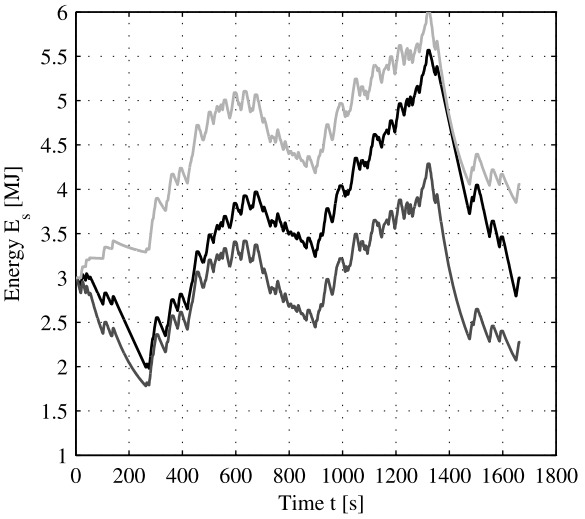

Fig. 6.4 The state-of-energy trajectories of the real-time implementable strategy. In *black* the optimal solution, in *medium gray* the state-of-energy trajectory that results from a high initial guess of the costate, and in *light gray* the state-of-energy trajectory that results from a low initial guess of the costate

Table 6.1 Fuel consumption results of the real-time implementable strategies compared to the baseline and optimal solution. Here, E_f is the fuel consumption, ΔE_s is the state-of-energy deviation at the end of the cycle, $\tilde{E}_f$ is the equivalent fuel consumption using the optimal costate variable at $p^*(t_f)$ to account for the difference in battery state-of-energy. The difference in fuel consumption relative to the baseline vehicle is also given

Strategy/Situation	E_f [MJ]	ΔE_s [MJ]	$\tilde{E}_f$ [MJ]	$\tilde{E}_f$ %
Baseline (engine only)	160.1	–	160.1	100
Unconstrained optimal solution	135.7	$<\pm 0.01$	135.7	84.78
Real-time solution with $\hat{p}^0 = 2.5$	134.2	0.725	136.0	84.96
Real-time solution with $\hat{p}^0 = 2.9$	138.7	-1.057	135.9	84.91

the off-line computed optimal constrained solution. The first real-time strategy is based on (6.4) with constant reference $E_{s\_r} = 3$ [MJ]. The second real-time strategy takes use of the adaptive reference based on (6.5). The following settings are used. For the kinetic energy gain $K_E = 0.4$, meaning that it is expected that 40 % of the kinetic energy can be re-used. For the potential energy gain $K_h = 0.10$, meaning that 10 % of the available potential energy is re-used. The potential energy gain is relatively low because part of the potential energy is transferred directly into kinetic energy. Both real-time strategies use the same settings for the feedback parameters; $E_{s\_r} = 3$ [MJ], $p^0 = 2.6$, $K_p = 0.01$ and $K_i = 0.2$.

The results are shown in Figs. 6.5 and 6.6. It can be seen that both real-time strategies saturate on the upper state-of-energy bound. The real-time strategy with constant reference obtains a fuel consumption that is one percent point higher than the optimal solution, see Table 6.2. Since the real-time strategy is saturated not all available recoverable energy can be recovered. Using the adaptive real-time strategy

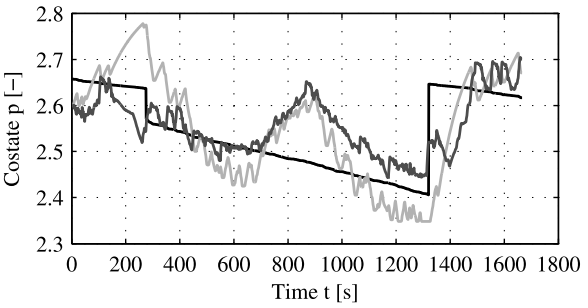

Fig. 6.5 Costate trajectories of the real-time implementable strategy. In *black* the optimal solution, in *light gray* the costate trajectory that results from the real-time strategy with constant reference, and in *medium gray* the real-time strategy with adaptive state-of-energy reference

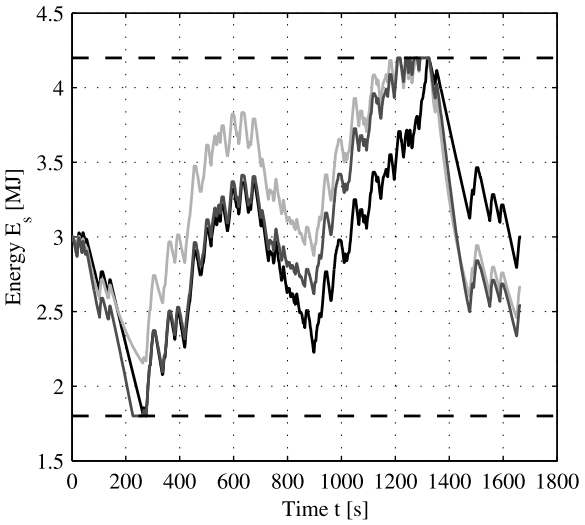

Fig. 6.6 The state-of-energy trajectories of the real-time implementable strategy. In *black* the optimal solution, in *light gray* the costate trajectory that results from the real-time strategy with constant reference, and in *medium gray* the real-time strategy with adaptive state-of-energy reference

Table 6.2 Fuel consumption results of the real-time strategies compared to the baseline and constrained optimal solution. Here, E_f is the fuel consumption, ΔE_s is the state-of-energy deviation at the end of the cycle, $\tilde{E}_f$ is the equivalent fuel consumption using the optimal costate variable at $p^*(t_f)$ to account for the difference in battery state-of-energy. The difference in fuel consumption relative to the baseline vehicle is also given

Strategy/Situation	E_f [MJ]	ΔE_s [MJ]	$\tilde{E}_f$ [MJ]	$\tilde{E}_f$ %
Baseline (engine only)	160.1	–	160.1	100
Constrained optimal solution	135.9	<0.01	135.9	84.88
Real-time strategy with $E_{s\_r} = 3$	136.5	0.337	137.3	85.76
Real-time strategy with E_{s_r} adaptive	135.1	0.459	136.2	85.05

it is, however, possible to stay within 0.2 % of the global optimum. It can also be seen that the adaptive strategy follows the optimal state-of-energy trajectory better.

6.4 Bibliographical Notes

At first glance, the easiest way to get a hybrid vehicle up and running with a real-time implemented strategy is to define a set of rules that decide when to use the electric machine and when not. Some rule-based strategies can be found in Baumann et al. (2000), Lin et al. (2004), Hofman et al. (2007). Fuzzy logic is proposed by Schouten et al. (2003) to obtain a systematic approach to derive a set of rules.

Optimal control-based approaches have been explored by several researchers as well. Paganelli et al. (2001) introduced the concept of Equivalent Consumption Minimization Strategy (ECMS). In ECMS the cost of using the stored energy in the battery is weighted against the cost of using fuel with an introduced "equivalence factor". Similar ideas can be found in Johnson et al. (2000). In Delprat et al. (2002) it was recognized that the equivalence factor is closely related to the state-of-energy variation and a feedback on the state-of-energy is suggested. In the same year, without providing a link to optimal control, feedback on the state-of-energy is also proposed by Kleimaier and Schröder (2002). In Koot et al. (2005), feedback to estimate an equivalence factor is demonstrated in an optimal control framework.

Hereafter, real-time strategies that are based upon the observations obtained with Pontryagin's Minimum Principle are further developed. Pisu and Rizzoni (2007) and Ambühl et al. (2010) suggest to apply nonlinear feedback on the state-of-energy, to reduce control actions for a state-of-energy around the reference. In Van Keulen et al. (2008) a feedback on a state-of-energy corrected for kinetic and potential energy is proposed. For the optimization of the Hamiltonian-like function, analytical solutions presented in Bernard et al. (2010), Van Keulen (2011) can be applied. A numerical approach can be found in Van Mullem et al. (2010).

The real-time control of plug-in hybrids is more involved in the sense that a depleting strategy is required such that a constant state-of-energy reference does not work. Supervisory strategies for plug-in hybrid vehicles can be found in, e.g., Stockar et al. (2011). Real-time strategies that use predictive information, coming from an on-board navigation system, to enhance optimality is a research topic that has drawn attention as well, see Kessels and Van den Bosch (2008), Van Keulen et al. (2010).

References

Ambühl D, Sundström O, Sciarretta A, Guzzella L (2010) Explicit optimal control policy and its practical application for hybrid electric powertrains. Control Eng Pract 18:1429–1439

Baumann BM, Washington G, Glenn BC, Rizzoni G (2000) Mechatronic design and control of hybrid electric vehicles. IEEE/ASME Trans Mechatron 5(1):58–72

Bernard J, Delprat S, Guerra TM, Büchi FN (2010) Fuel efficient power management strategy for fuel cell hybrid powertrains. Control Eng Pract 18:408–417

Delprat S, Guerra TM, Rimaux J (2002) Optimal control of a parallel powertrain: from global optimization to real time control strategy. In: Proc IEEE veh technol conf. IEEE, Birmingham, pp 2082–2088

Guzzella L, Sciarretta A (2005) Vehicle propulsion systems. Springer, Berlin

Hofman T, Steinbuch M, Van Druten R, Serrarens A (2007) Rule-based energy management strategies for hybrid vehicles. Int J Elec Hybrid Veh 1:71–94

Johnson VH, Wipke KB, Rausen DJ (2000) HEV control strategy for real-time optimization of fuel economy and emissions. In: 2000 future car congress proc, Arlington, VA. SAE paper 2000-01-1543

Kessels JTBA, Van den Bosch PPJ (2008) Electronic horizon: road information used by energy management strategies. Int J Intell Inform Database Syst 2(2):187–203

Van Keulen T (2011) Fuel optimal control of hybrid vehicles. PhD thesis, Technische Universiteit Eindhoven, Eindhoven, The Netherlands

Van Keulen T, De Jager B, Steinbuch M (2008) An adaptive sub-optimal energy management strategy for hybrid drivetrains. In: Proc 17th IFAC. World Congress, Seoul, Korea, pp 102–107

Van Keulen T, De Jager B, Serrarens A, Steinbuch M (2010) Optimal energy management in hybrid electric trucks using route information. Oil Gas Sci Technol Rev IFP 65:103–113

Kleimaier A, Schröder D (2002) An approach for the online optimized control of a hybrid powertrain. In: Proc internat workshop advanced motion control, Maribor, Slovenia, pp 215–220

Koot M, Kessels JTBA, De Jager B, Heemels WPMH, Van den Bosch PPJ, Steinbuch M (2005) Energy management strategies for vehicular electric power systems. IEEE Trans Veh Technol 54(3):771–782

Lin CC, Jeon S, Peng H, Lee JM (2004) Driving pattern recognition for control of hybrid electric trucks. Veh Syst Dyn 42:41–58

Van Mullem D, Van Keulen T, Kessels JTBA, De Jager B, Steinbuch M (2010) Implementation of an optimal control energy management strategy in a hybrid truck. In: Proc IFAC symp advances automotive control, München, Germany, 6 p

Paganelli G, Ercole G, Brahma A, Guezennec Y, Rizzoni G (2001) General supervisory control policy for the energy optimization of charge-sustaining hybrid electric vehicles. JSAE Rev 22:511–518

Pisu P, Rizzoni G (2007) A comparative study of supervisory control strategies for hybrid electric vehicles. IEEE Trans Control Syst Technol 15(3):506–518

Rodatz P, Paganelli G, Sciarretta A, Guzzella L (2005) Optimal power management of an experimental fuel cell/supercapacitor-powered hybrid vehicle. Control Eng Pract 13:41–53

Schouten NJ, Salman A, Kheir NA (2003) Energy management strategies for parallel hybrid vehicles using fuzzy logic. Control Eng Pract 11:171–177

Stockar S, Marano V, Canova M, Rizzoni G, Guzzella L (2011) Energy-optimal control of plug-in hybrid electric vehicles for real-world driving cycles. IEEE Trans Veh Technol 60(7):2949–2962

Vahidi A, Stefanopoulou A, Peng H (2005) Recursive least squares with forgetting for online estimation of vehicle mass and road grade. Veh Syst Dyn 43:31–55

Chapter 7
Experimental Case Studies

7.1 Micro Hybrid Energy Management

This case study[1] introduces an Energy Management Strategy (EMS) solution for a light-duty vehicle, a micro hybrid, showing through simulations and roller–dynamometer experiments the profits that can be expected in fuel economy with very small additional investments in vehicle hardware.

The electric power demand in light-duty vehicles increases rapidly and to supply all electric loads efficiently, energy management turns out to be a suitable solution. The strategies developed in this case study focus on vehicles with a conventional drivetrain where the alternator is controlled and the standard battery is used as a storage device, a so-called *micro hybrid*. By exploiting the storage capacity of the battery, the production and distribution of electric power is rescheduled to more economic moments. In addition, this case study explores the advantages of electric loads with a flexible power demand. Based on optimization techniques, an optimal off-line strategy as well as a causal online strategy are presented. Simulations illustrate the benefits of the EMS in terms of fuel economy. The online strategy has also been implemented in a series-production vehicle. Real-world experiments on a chassis dynamometer test-bench validate the strategy, but also reveal additional fuel economy benefits because of unexpected side-effects from the engine control unit and the driver. Measured profits in fuel economy are as large as 2.6 %, with only minimal changes to the vehicle hardware.

7.1.1 Optimal Power Control in Micro Hybrid Electric Vehicles

Energy management in this book is inextricably associated with a hybrid (electric) vehicle. Nonetheless, a traditional vehicle with a conventional drivetrain and

[1] This section re-uses material presented in Kessels et al. (2007).

B. de Jager et al., *Optimal Control of Hybrid Vehicles*, Advances in Industrial Control,
DOI 10.1007/978-1-4471-5076-3_7, © Springer-Verlag London 2013

a belt-driven alternator also offers freedom for EMS. Conceptually, the topology of a parallel HEV looks similar to a traditional vehicle, although the power through the alternator is limited to one direction. Moreover, the power capabilities of the electric machine in an HEV are typically larger to be able to provide tractive force to the wheels. This initiated the question what an EMS can offer for a traditional vehicle, without the need for additional investments in vehicle hardware. With primarily changes in vehicle software, the return on investment is relative high. On the other hand, the absolute fuel profits will be limited, because the mechanical power demand is far more dominant than the electric power request in a traditional vehicle.

An EMS uses the storage capacity of the battery when the power from the alternator does not match with the power request of the electric loads. This concept has two disadvantages: first, temporarily storing energy always brings additional losses and second, the storage device wears out faster. To overcome both problems, we also consider electric loads with a flexible power demand. In this way, the power request from the loads can be adapted to the generated power. Loads with a flexible power demand are characterized by the fact that they accept, up to a certain level, more or less power, without significant performance degradation for the driver. Especially heating and cooling functions are suited for this purpose, as shown in Åsbogård et al. (2004).

With only minor changes to the vehicle, it is possible to implement an EMS that takes into account two degrees of freedom: the power produced by the alternator and the power supply to the electric loads. So indirectly the power to the battery is controlled. For convenience, the alternator power control problem will be called Power Supply Management (PSM), whereas PSM extended with additional freedom for the electric loads is captured by Power Distribution Management (PDM). Earlier publications on PSM and PDM appeared in Koot et al. (2005) and Kessels et al. (2005), respectively.

7.1.2 Drivetrain Model

The PSM and PDM strategy make use of a power-based model, see Fig. 7.1. In this model, the internal combustion engine (ICE) and the alternator rely on quasi-static maps. Because the EMS does not interfere with the vehicle dynamics, these models are sufficiently accurate. Compared to the models introduced in Chap. 2, advantage can be taken of the properties of a micro hybrid to simplify the models.

- The alternator can only generate electricity, it cannot be used as a motor, so $P_m \leq 0$ holds, and only one branch of (2.8) has to be used, avoiding the non-smoothness in the generator model.
- The maximum generating power, $\underline{P}_m$, is quite small related to the maximum power of the engine, $\overline{P}_p$, so it is profitable to consider local approximations for the static maps, which only have to represent the interval in which P_p, P_l and P_s can be varied given the desired P_r and small available range of P_m.

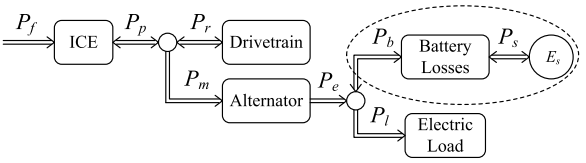

Fig. 7.1 Overview of power flow signals in the micro hybrid vehicle

The engine model is described by a nonlinear static map which specifies the relation between the fuel mass flow $\dot{m}$ or fuel power P_f, engine power P_p, and engine speed ω, similar to (2.7):

$$P_f = P_f(P_p, \omega), \quad \text{where } P_p = P_r - P_m. \tag{7.1}$$

Using a similar approach, the alternator model is captured by a nonlinear static map, expressing the mechanical power P_m as a function of the electric power P_e, similar to (2.8):

$$P_m = P_m(P_e, \omega), \quad \text{where } P_e = P_b - P_l. \tag{7.2}$$

For the battery a similar relation holds to represent the energy losses between the power P_b at the battery terminals and the net stored/retrieved power P_s, similar to (2.19):

$$P_b = P_b(P_s). \tag{7.3}$$

7.1.3 Problem Definition

In this case study, the control objective of the EMS is to improve the vehicle's fuel economy, although the reduction of particular tail-pipe emissions can be done in a similar way. The primary power converter in the vehicle is the ICE whereas the storage capacity of the battery offers freedom to schedule the driver's electric power request over time. Furthermore, the flexible electric loads offer additional freedom to maximize the fuel economy. For developing an EMS with optimal performance, the control problem is formulated as an optimization problem:

$$\min_u J(u) \quad \text{subject to} \quad h(u) \leq 0. \tag{7.4}$$

The cost function $J(u)$ is selected such that it represents the vehicle's fuel consumption over an arbitrary drive cycle with time length $t_f - t_0$:

$$J(P_s, P_l) = \int_{t_0}^{t_f} P_f(P_s, P_l, P_r, \omega)\, \mathrm{d}t, \tag{7.5}$$

where

$$P_f(P_s, P_l, P_r, \omega) = P_f\big(P_r - P_m(P_e, \omega), \omega\big), \tag{7.6}$$

and P_e defined in (7.2). Note that the decision variable u covers two variables: the internal battery power P_s and the power to the electric loads P_l. The corresponding control variable P_e is calculated afterward using (7.2) and (7.3).

The constraints are due to physical limitations of components as well as the requirement to have a charge sustaining vehicle. The operating range of the engine, the alternator, and the battery is limited in power, so input constraints are introduced on the minimum and maximum power flow through these components:

$$\underline{P}_p(t) \leq P_p(t) \leq \overline{P}_p(t) \tag{7.7}$$

$$\underline{P}_e(t) \leq P_e(t) \leq \overline{P}_e(t) \tag{7.8}$$

$$\underline{P}_b(t) \leq P_b(t) \leq \overline{P}_b(t) \quad \forall t \in [t_0, t_f]. \tag{7.9}$$

A charge sustaining strategy claims that the battery satisfies a minimum SOE level at the end of the drive cycle. This can be achieved by including an end-point constraint on the energy level of the battery:

$$E_s(t_f) = E_s(t_0) + \int_{t_0}^{t_f} -P_s(t)\,\mathrm{d}t \geq E_s^f, \tag{7.10}$$

where E_s^f is an arbitrarily selected reference value that should be satisfied at $t = t_f$, e.g., $E_s^f = E_s(t_0)$.

Finally, constraints on P_l are used to characterize the energy and power demand of the electric loads. It is assumed that all individual loads can be aggregated and this results in a separate power and energy constraint:

$$\underline{P}_l(t) \leq P_l(t) \leq \overline{P}_l(t) \quad \forall t \in [t_0, t_f] \tag{7.11}$$

$$\int_{t_0}^{t} P_l(\tau)\,\mathrm{d}\tau \geq \underline{E}_l(t) \quad \forall t \in [t_0, t_f]. \tag{7.12}$$

7.1.4 Quadratic Programming

Besides using Pontryagin's Minimum Principle, see Chap. 4, or Dynamic Programming, see Chap. 5, one can obtain an optimal control law using alternative optimization techniques such as Linear Programming (LP) and Quadratic Programming (QP). Here the work of Tate and Boyd (2000) is an excellent starting point and provides a well defined LP problem. Compared to DP, the LP and QP method avoid excessive memory usage or extreme calculation times while handling a multi-dimensional state-space. Furthermore, these methods are easily incorporated into a Model Predictive Control framework (Camacho and Bordons 2004). This way, the added value of additional prediction information can be analyzed using a prediction horizon with variable length.

Finding the optimal solution for the problem defined in the previous section is computationally demanding. To come to a solution close to the global optimal solution, the original problem is approximated with a Quadratic Programming (QP) problem. Such a QP-structure is characterized by a quadratic cost function, subject to linear constraints:

$$\min_u \frac{1}{2} u^\top H u + h^\top u \quad \text{subject to } Au \le b, \tag{7.13}$$

where H and A are matrices and h and b are (column) vectors of appropriate dimensions, as defined in the remainder of this section. The decision variable u is a column vector.

Model Reduction To derive a quadratic description for the cost function (7.5), the models of the individual components need to be reduced. For the engine map, a (piece-wise) linear approximation will be used:

$$P_f(P_p, \omega) \approx \gamma_{p,1} P_p + \gamma_{p,0}. \tag{7.14}$$

Here, $\gamma_{p,0}$ is not scaled by $\overline{P}_p$ as in (2.4). The parameters $\gamma_{p,1}$ and $\gamma_{p,0}$ are state dependent (P_r, ω) and are selected such that they represent a local fit of the fuel map in the range $P_p = [P_r, P_r - \underline{P}_m]$. In practical situations, the fuel map of an engine is obtained by measuring its fuel consumption at a finite number of grid points. These grid points cover the entire operating area of the engine. Compared to the power range of the alternator, this is a relatively coarse grid and therefore it is acceptable to approximate the fuel consumption by a local linear fit.

The losses in a conventional alternator change according to its operating point, vary widely and can be considerable. Similar to the ICE, these large variations are due to friction losses and they have a dominant effect when the alternator generates no electric power. Measurement data show that the mechanical input power increases almost proportionally with the output power. Only at higher power levels do these losses increase more than proportionally. For that reason, the alternator map is approximated by a quadratic fit similar to (2.8), but for the inverse relation:

$$P_m(P_e, \omega) \approx -\gamma_{m,2} P_e^2 + \gamma_{m,1} P_e - \gamma_{m,0}. \tag{7.15}$$

The parameters $\gamma_{m,2}$, $\gamma_{m,1}$ and $\gamma_{m,0}$ are speed dependent. They approximate the alternator map over its entire power range $P_e = [\underline{P}_e, \overline{P}_e]$ at a certain engine speed ω.

According to impedance spectra measurements of a lead-acid battery, see, e.g., Buller et al. (2003), it is known that the losses in the battery increase for higher power flows. Moreover, the impedance changes when charging or discharging the battery. Consequently, a battery model incorporating both linear and quadratic losses is used as in the polynomial battery model (2.21), but using a different parametrization:

$$P_b(P_s) \approx -\beta_2 P_s^2 + \min\left(\beta_1^- P_s, P_s/\beta_1^+\right). \tag{7.16}$$

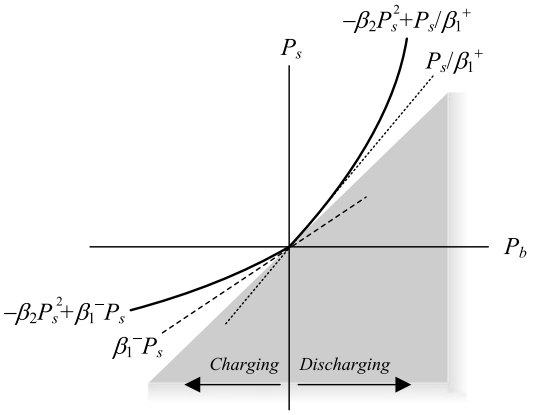

Fig. 7.2 Parameters in battery loss model showing concave relation between P_b and P_s, note that P_b is computed, given P_s

Note that the difference in behavior during charging and discharging is accounted for by β_1 and not by β_2. In Fig. 7.2 the contribution of each individual term is shown. The parameter $\beta_2 > 0$ represents the quadratic losses whereas β_1^+ and β_1^- indicate the piece-wise linear losses for charging and discharging, respectively. In this case study, these parameters are estimated from experimental data. However, they can also serve as a tuning parameter to limit the actual battery usage of the EMS. That is, incorporating more losses in the battery model than actually present in reality will discourage the EMS from using the battery as an energy storage buffer. Because battery usage is strongly related to battery wear, the parameters β_2, β_1^+, and β_1^- turn out to be a trade-off between battery wear versus fuel reduction performance.

QP Formulation The battery model described in (7.16) cannot be directly included in the QP-framework of (7.13). Fortunately, the restrictions on β_2, β_1^+, and β_1^- guarantee that (7.16) is always a concave function. As shown in De Jager (2003), it is possible to reformulate the expression $\min(\beta_1^- P_s, P_s/\beta_1^+)$ with an auxiliary variable P_a:

$$\min_{P_a} -P_a \quad \text{subject to} \quad \begin{cases} P_a \leq P_s \beta_1^-, \\ P_a \leq P_s/\beta_1^+. \end{cases} \tag{7.17}$$

Variable P_a becomes another decision variable. There is normally no need to add a term related to $-P_a$ to the objective, because reducing P_f has the same effect as increasing P_a. The constraints in (7.17) need to be added to the other ones, however. After replacing the second term in (7.16) with P_a, this new expression is substituted into (7.15) with $P_e = P_b - P_l$. The substitution of (7.15) into (7.14) then results in a relation between fuel consumption P_f and battery power P_s, load power P_l, and auxiliary power P_a which is of fourth order. Because a quadratic relation is needed for a QP-structure, a second order Taylor approximation has been applied, leaving out the higher order terms. To that end, the decision variable P_l has been changed into the zero-mean variable ΔP_l, representing the deviation from the average load

power $\tilde{P}_l$:

$$P_l := \tilde{P}_l + \Delta P_l. \tag{7.18}$$

The cost criterion in (7.5) is rewritten in discrete time with sampling interval ΔT over n_p periods:

$$J = \sum_{k=1}^{n_p} P_f\big(P_s(k), \Delta P_l(k), P_a(k)\big)\Delta T. \tag{7.19}$$

The decision variable $u = [P_s \ \Delta P_l \ P_a]^\top \in \mathbb{R}^{3n_p}$ covers all periods $k = 1, \ldots, n_p$ and yields the following description for H and h in (7.13):

$$H = \operatorname{diag}\big[H(1), \ldots, H(n_p)\big], \tag{7.20}$$

$$h = \big[h^\top(1), \ldots, h^\top(n_p)\big]^\top, \tag{7.21}$$

with

$$H(k) = \begin{bmatrix} 2\gamma_{p,1}\gamma_{m,1}\beta_2 + 4\gamma_{p,1}\gamma_{m,2}\beta_2\tilde{P}_l & 0 & 0 \\ 0 & 2\gamma_{p,1}\gamma_{m,2} & -2\gamma_{p,1}\gamma_{m,2} \\ 0 & -2\gamma_{p,1}\gamma_{m,2} & 2\gamma_{p,1}\gamma_{m,2} \end{bmatrix} \tag{7.22}$$

and

$$h(k) = \begin{bmatrix} 0 \\ \gamma_{p,1}\gamma_{m,1} + 2\gamma_{p,1}\gamma_{m,2}\tilde{P}_l \\ -\gamma_{p,1}\gamma_{m,1} - 2\gamma_{p,1}\gamma_{m,2}\tilde{P}_l \end{bmatrix}, \tag{7.23}$$

where all parameters are functions of k.

All constraints given in (7.7)–(7.12) have to be written as linear constraints on the decision variables. Due to the losses in the battery model, the relation between P_b and P_s is nonlinear, see (7.16). Therefore, one cannot use a linear combination of P_s and ΔP_l to replace the constraint on P_e. To circumvent this problem, the energy losses in the battery model are neglected during constraint handling, so P_b is assumed to be equal to P_s at this point. Now it is possible to write (7.7) as a linear constraint on P_s and ΔP_l by using the inverse of (7.15) and selecting the correct solution. Also (7.8) appears as a linear constraint, whereas the implementation of (7.9) is trivial. Note that these new constraints allow slightly more freedom than the original problem, but differences are very limited. Finally, the three constraints are aggregated into one constraint for each period $k = 1, \ldots, n_p$:

$$\underline{P}_e \le P_s - \tilde{P}_l - \Delta P_l \le \overline{P}_e. \tag{7.24}$$

The end-point constraint in (7.10) on the energy level in the battery becomes

$$E_s(t_0) - \sum_{k=1}^{n_p} P_s(k)\Delta T \ge E_s^f. \tag{7.25}$$

The requirements on the power and energy to the loads are written in terms of $\tilde{P}_l + \Delta P_l$. For the constraint in (7.11) this is rather straightforward and for each period $k = 1, \ldots, n_p$:

$$\underline{P}_l \leq \tilde{P}_l + \Delta P_l \leq \overline{P}_l. \tag{7.26}$$

The energy constraint from (7.12) needs to be evaluated in all periods $k = 1, \ldots, n_p$, resulting in n_p constraints:

$$\sum_{i=1}^{k} (\tilde{P}_l + \Delta P_l) \Delta T \geq \underline{E}_l(k), \quad k = 1, \ldots, n_p. \tag{7.27}$$

Altogether, a drive cycle with n_p periods leads to $3n_p$ decision variables and $6n_p + 1$ constraints in the QP-structure from (7.13).

Model Predictive Control The optimization problem formulated above requires the entire drive cycle to be known in advance. In real-world driving situations, this will be practically impossible. However, the idea that the vehicle speed can be predicted in the near future is certainly realistic. With only minor changes, it is possible to put the QP-problem into a Model Predictive Control (MPC) framework, see also Camacho and Bordons (2004), Back et al. (2002) and West et al. (2003). Instead of performing the optimization in (7.13) over the entire drive cycle, it will be limited to a prediction horizon of n_p periods. Only the first value of the resulting control sequence is implemented, whereas the calculations are repeated each instant with updated state and prediction information.

The implementation of this MPC strategy in a simulation environment shows that a reduced prediction horizon for (7.19) and (7.25) puts a serious limitation on its performance, see Sect. 7.1.7. Particularly, the end-point constraint (7.25) forces the strategy to keep the battery close to E_s^f such that it resembles the baseline situation. This end-point constraint is only a method to guarantee a charge sustaining solution. The next section presents an alternative solution by reformulating this constraint.

7.1.5 Online Strategy

This section presents a causal EMS, which is identical to the solution provided in Chap. 6, but repeated here to make the presentation self-contained. The strategy does not rely on prediction information through a relaxation of the end-point constraint from (7.25).

Strategy Analysis First, consider the problem definition from (7.4), without the inequality constraints $h(u) \leq 0$. In the situation of PSM, the electric load cycle is predefined and the optimization problem reduces to one decision variable P_s:

$$\min_{P_s} \int_{t_0}^{t_f} P_f(P_s, P_r, P_l, \omega)\, \mathrm{d}t. \tag{7.28}$$

Now assume that at the end of the trip the energy in the battery matches its initial starting value. This way, the end-point constraint changes into an equality constraint:

$$E_s(t_0) + \int_{t_0}^{t_f} -P_s(t)\,\mathrm{d}t = E_s(t_0) \quad \Rightarrow \quad \int_{t_0}^{t_f} P_s(t)\,\mathrm{d}t = 0. \tag{7.29}$$

A new problem definition is formulated for the minimization of (7.28) in combination with the equality constraint (7.29). For convenience, it is written in discrete time but the sampling interval ΔT has been omitted:

$$\begin{aligned} &\min_{P_s} \quad \sum_{k=1}^{n_p} P_f\big(P_s(k), P_r(k), P_l(k), \omega(k)\big), \\ &\text{subject to} \quad \sum_{k=1}^{n_p} P_s(k) = 0. \end{aligned} \tag{7.30}$$

A solution for this optimization problem can be found by incorporating the equality constraint into the Lagrangian function using a Lagrange multiplier, p. A similar approach can be found already in Van den Bosch and Lootsma (1987). The following Lagrangian L is defined:

$$L\big(P_s(1), \ldots, P_s(n_p), p\big) = \sum_{k=1}^{n_p} P_f\big(P_s(k), P_r(k), P_l(k), \omega(k)\big) + p \sum_{k=1}^{n_p} P_s(k). \tag{7.31}$$

Physically, this new objective function makes sense because it weighs the energy change of the battery with the actual fuel consumption of the engine. The quantity p represents the corresponding fuel cost when energy is stored or taken from the battery. It is clear that there exists a strong relation between this quantity and the definition of $\gamma_{p,1}$ as given in (7.14). Nevertheless, $\gamma_{p,1}$ only considers the fuel costs from the ICE, whereas the influence from the electric machine and the battery is not included there.

The minimum value for $L(P_s(1), \ldots, P_s(n_p), p)$ is found by putting the derivatives equal to zero:

$$\frac{\partial L(P_s(1), \ldots, P_s(n_p), p)}{\partial P_s(k)} = 0, \quad 1 \le k \le n_p, \tag{7.32}$$

$$\frac{\partial L(P_s(1), \ldots, P_s(n_p), p)}{\partial p} = 0. \tag{7.33}$$

In the case where $P_f(P_s, P_r, P_l, \omega)$ is a strictly convex function, there exists a unique solution $(P_s^*(1), \ldots, P_s^*(n_p), p^*)$ for this set of $n_p + 1$ equations. Typically, the solution of p^* is calculated with information about the entire drive cycle. However, if p^* is known, the sequence $P_s^*(k)$, $k = 1, \ldots, n_p$, can also be calculated by

an optimization at the present moment k:

$$P_s^*(k) = \arg\min_{P_s} \left\{ P_f(P_s, P_r, P_l, \omega) + p^* P_s \right\}. \tag{7.34}$$

So far, all calculations have been done with decision variable P_s, but the control variable is the alternator power P_e. This variable follows from the battery model (7.16), which delivers P_b, and the powernet split $P_b = P_e + P_l$.

Finally, the situation with PDM is considered, where the power to the electric load offers additional freedom. Similar to the required energy in the battery at the end of the drive cycle, the loads also require a certain amount of energy at the end of the trip. As such, the load power is calculated in a similar manner as

$$P_l^* = \arg\min_{P_l} \left\{ P_f\left(P_e^*, P_r, P_l, \omega\right) + p^* \beta_1^{-1}\left(P_e^* + P_l\right) \right\}. \tag{7.35}$$

The minimum and maximum power to the loads is restricted by (7.11). Incorporating these constraints leads to the following setpoint for P_l:

$$P_l = \max\left[\underline{P}_l, \min\left[P_l^*, \overline{P}_l\right]\right]. \tag{7.36}$$

Optimal Performance This online control strategy achieves the highest fuel economy benefits if p^* is calculated correctly. Moreover, each drive cycle requires a different p^* to obtain a preferred energy level E_s^f at the end of the drive cycle. A solution for p^* has to be found where the energy exchange with the battery is balanced and the SOE at the beginning and end of the drive cycle are equivalent.

Adaptive Strategy Instead of calculating p^* off-line in advance, one could make an online estimation, $\hat{p}$. The method that has been selected here results in an adaptive strategy with a PI controller as presented in Koot et al. (2005). Although different approaches are known from the literature (e.g., zone control, see West et al. 2003), this method enables the online EMS to achieve a performance close to the optimal MPC strategy, described in Sect. 7.1.4. The basic idea is that the SOE of the battery indicates whether $\hat{p}$ is estimated correctly or not. From a control point of view, this corresponds to a leveling control problem where the SOE should be kept near a nominal value SOE_r. A Proportional Integral (PI) controller with a rather small bandwidth fulfills this requirement. The block diagram is shown in Fig. 7.3, with $\hat{p}$ equal to

$$\hat{p}(t) = \hat{p}^0 + K_p\, e(t) + K_i \int_{t_0}^{t} e(\tau)\, \mathrm{d}\tau, \tag{7.37}$$

with $\hat{p}^0$ an initial guess.

7.1.6 Experimental Validation

Simulation Environment For analyzing the energy management strategies, a simulation environment has been developed that describes a light-duty vehicle. This

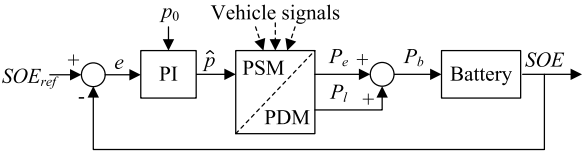

Fig. 7.3 Feedback diagram for estimating $\hat{p}$

is a midsize series-production vehicle with a 2.0ℓ gasoline engine and a 5-speed manual transmission. The simulation model is built around a dynamic forward-facing drivetrain model, including a dynamic model for the driver. The main components are listed as follows.

- *Driver*: To control the speed of the vehicle, a PI-controlled *driver model* is applied. The output signals are the three pedal positions: throttle, brake, and clutch. The initial parameter settings for the driver are taken from literature, see Allen et al. (1996).
- *Drivetrain*: The drivetrain model covers the longitudinal dynamics of the vehicle. It describes the relation from the engine to the wheels and consists of the clutch, transmission, final drive, and chassis. It is based on the ADVISOR model Wipke et al. (1999), but differs from it by being forward-facing. This means that it converts the input torque from the ICE into a rotational speed for the wheels using a dynamic drivetrain model.
- *Powernet*: The traditional SLI-battery (Start, Light, and Ignition) is replaced by a valve-regulated lead-acid (VRLA) battery, which can handle much more charge/discharge cycles before it wears out. The simulation model makes use of an impedance-based battery model as described by Buller et al. (2003). Furthermore, an advanced alternator (1.6 [kW], voltage controlled) replaces the standard alternator. This allows the EMS to control the power from the alternator. Finally, the electric loads that are present in the vehicle are represented as one lumped load in the simulation model.

Experimental results from a test vehicle on a roller–dynamometer are used to validate the drivetrain model and the exhaust gas emissions. In addition, separate tests are executed to validate the electric power net model. An extended overview of the simulation model and its validation procedure can be found in Kessels et al. (2004).

Vehicle Implementation The strategy has been implemented in the same vehicle as used in the simulations using dedicated control equipment. The alternator has been modified such that its output voltage is not fixed but follows a voltage setpoint. A VRLA battery with a capacity of 60 [Ah] replaces the original 12 [V] battery.

During the vehicle tests, special attention is given to the interaction between the Engine Control Module (ECM), i.e., the ECU controlling the engine, and the alternator. In the original vehicle configuration, the alternator sends a status-signal to the ECM about its present electric load. Given this information, the ECM adds a feedforward signal to the engine fueling system, such that it anticipates on quick changes in the alternator power. However, this feedforward compensation leads to extra fuel

injection during regenerative braking. Therefore, a by-pass of the alternator signal is done when the EMS is implemented in the vehicle.

It turns out that the original configuration also benefits from this alternator by-pass in terms of fuel economy. Unfortunately, the vehicle tests with the baseline configuration include this feedforward signal.

Evaluated Strategies The standard drive cycle for vehicle homologation in Europe is the New European Driving Cycle (NEDC), see Fig. 2.16. Based on this drive cycle, four different strategies are evaluated: BL (baseline), BL + 250W, PSM and PDM. The BL configuration refers to the original vehicle configuration with a fixed alternator voltage at 13.7 [V]. In line with the official NEDC regulations, configuration BL corresponds to the native engine load, which is approximately 220 [W]. Unfortunately, this load is always present, and to validate the concept of PDM, more flexibility in the power demand is desired. This is achieved with an external electric load connected to the *electric powernet*. For the configuration BL+250W, this extra load adds 250 [W] to the native engine load along the entire drive cycle. With PDM, this load follows the setpoints from the EMS, whereas the average load remains 250 [W] through adaptation of the restrictions on P_l in (7.11):

$$\underline{P}_l(t) = \begin{cases} 0 & \text{if } E_l(t) \geq 250t \\ 250 & \text{if } E_l(t) < 250t \end{cases} \quad \text{with } E_l(t) = \int_{t_0}^{t} P_l(\tau)\,\mathrm{d}\tau, \tag{7.38}$$

$$\overline{P}_l(t) = 500. \tag{7.39}$$

In the simulation environment, both the off-line and the online strategies are evaluated for PSM and PDM. The simulation with the off-line MPC strategy is done in two steps. First, the signals P_r and ω are recorded during a pilot simulation with configuration BL. Next, these signals are used as prediction information in a second simulation with the MPC strategy. It has been verified that differences between the first and second simulation for P_r and ω are sufficiently small. Otherwise, further iterations would be required. The real-world experiments are executed with the online strategy from Sect. 7.1.5 and these experiments are done with a cold and hot engine start. In the simulation environment this is not possible because the engine model is only valid for a hot engine.

Table 7.1 provides a brief overview of all strategies that will be considered. The MPC strategy calculates its control law by solving (7.13) with the cost criterion (7.19) and constraints (7.24)–(7.27). The control law for the online PSM strategy is given in (7.34), and the online PDM strategy applies additionally (7.35). Note that for PSM the value of P_l is predefined by the drive cycle and is not calculated by the EMS.

7.1.7 Strategy Results

Influence of Prediction Horizon The influence of the prediction horizon is evaluated with the QP method from Sect. 7.1.4 in an MPC-framework. Figure 7.4(a)

Table 7.1 Overview of evaluated strategies

Simulation environment (hot engine)		
BL	$\Longleftrightarrow$	PSM MPC PSM Online
BL + 250 W	$\Longleftrightarrow$	PDM MPC PDM Online
Roller–dynamometer experiments		
BL (cold)	$\Longleftrightarrow$	PSM Online (cold)
BL (hot)	$\Longleftrightarrow$	PSM Online (hot)
BL + 250W (hot)	$\Longleftrightarrow$	PDM Online (hot)

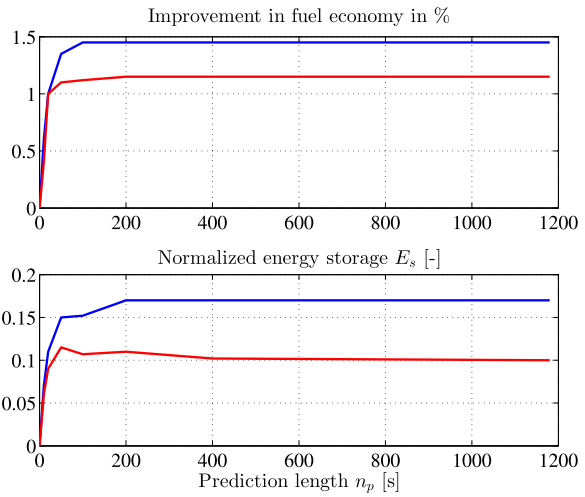

Fig. 7.4 Influence of prediction horizon on (**a**) fuel use and (**b**) battery use. The PSM strategy is in *blue* and the PDM strategy in *red*

shows the reduction in fuel consumption whereas Fig. 7.4(b) illustrates the total amount of energy stored in the battery. Both the PSM and PDM strategy are simulated for receding horizons of increasing lengths, $n_p = 1, \ldots, 1180$ and $\Delta T = 1$ [s]. When the prediction horizon reaches the end of the drive cycle, the control law is no longer updated and all remaining control actions are taken directly from that instant. The results for battery wear in Fig. 7.4(b) are normalized with respect to the battery capacity E_c:

$$\mathsf{E}_{\text{stored}} = \frac{-\int_{t_0}^{t_f} \min(P_b(t), 0)\, \mathrm{d}t}{E_c} \quad [-]. \tag{7.40}$$

The first observation from Fig. 7.4(a) is that the achieved fuel reduction with PSM and PDM is ultimately bounded. Moreover, the fuel economy benefits increase

Table 7.2 Overview of simulation results (hot-engine start)

Strategy	SOE_0 %	P_l [W]	Fuel mass [g/km]	SOE_f %	Fuel eco %
BL	100	245	59.61	100.0	–
PSM MPC	75	195	58.70	74.6	1.5
PSM Online	75	195	58.73	75.1	1.5
BL + 250 W	100	475	61.09	100.0	–
PDM MPC	75	465	60.42	75.0	1.1
PDM Online	75	465	60.42	75.1	1.1

rapidly until $n_p = 100$ and remain almost constant for a higher prediction length. This behavior can be explained as follows. The end-point constraint in (7.25) becomes very dominant for short predictions. That is, the EMS acts conservative when n_p is small, because it has to guarantee the preferred energy level E_s^f in the battery at the end of the prediction horizon. Moreover, the vehicle speed determines the operating point of the ICE and consequently the equivalent fuel cost $\gamma_{p,1}$ as defined in (7.14). As shown in De Jager (2004), the frequency spectrum of $\frac{\partial P_f}{\partial P_s}$ gives insight into the minimum length of the prediction horizon, so the speed profile of the NEDC is closely related to the required prediction length.

To obtain a performance close to the optimal situation, an accurate speed prediction of at least $n_p \Delta T = 100$ [s] is required, but due to uncertainties these predictions are not readily available. As a result, a different approach is preferred that does not rely on lengthy predictions, but still achieves a similar performance. This is achieved with the online strategy, by relaxing the end-point constraint.

Finally, one can extend the information in Fig. 7.4 with an extra parameter for the losses in the battery model (7.3). By including extra losses in the battery model, the EMS tends to follow the baseline strategy and, hence, $\mathsf{E}_{\text{stored}}$ decreases. Given the cycle life of the battery, it is up to the designer to optimize the trade-off between fuel economy benefits and battery wear.

Results from Experimental Validation An overview of the simulation results and the results from the roller–dynamometer experiments is given in Tables 7.2 and 7.3, respectively. Each strategy has been tested at least two times on the roller–dynamometer, and Table 7.3 presents average results. The columns in these tables cover the following information.

- SOE_0: Initial SOE of the battery. Each baseline strategy starts with a completely charged battery, so $\text{SOE}_0 = 100$ %. The PSM and PDM strategies start at $\text{SOE}_0 = \text{SOE}_r = 75$ %.
- P_l: This column expresses the average measured electric load profile along the NEDC. The electric load request from the vehicle experiments has also been used in the simulation environment.
- *Fuel mass and* CO_2: Knowledge about the vehicle's fuel economy is shown in these columns. The engine map in the simulation environment denotes the actual

Table 7.3 Overview of roller–dynamometer experiments

Strategy	SOE_0 %	P_l [W]	CO_2 [g/km]	SOE_f %	Fuel eco %
BL hot	100	242.7	183.6	100.0	–
PSM hot	75	192.7	179.2	74.7	2.4
BL + 250 W hot	100	472.7	188.0	100.0	–
PDM hot	75	465.8	185.4	75.2	1.4
BL cold	100	232.8	201.0	100.0	–
PSM cold	75	205.1	195.8	74.7	2.6

fuel mass flow of the engine, so the simulation model directly provides the fuel consumption along the drive cycle. This is different with the vehicle experiments, where the tail-pipe emissions are measured instead of the injected fuel mass flow. A good representation for the vehicle's fuel consumption is the tail-pipe carbon dioxide (CO_2) emission. The measured CO_2 emissions are shown in grams per kilometer and the relative reduction in CO_2 emissions will be used to calculate the benefits in fuel economy, see the last column.

- SOE_f: The final SOE level reached at the end of the drive cycle is indicated in this column.
- *Fuel eco*: The improvement in fuel economy for a particular strategy is calculated here. The values are calculated without taking differences between SOE_0 and SOE_f into account.

The signals of interest from one vehicle measurement (using the PSM strategy) are shown in Fig. 7.5 over the last 600 [s] of the NEDC drive cycle. In this figure, the following information is shown: the speed of the vehicle, the position of the accelerator pedal, the alternator power and the SOE of the battery. This figure also includes the corresponding signals from the simulation model. The accelerator pedal reveals that the human driver spends considerable more effort to follow the desired speed profile than the simulation model. The EMS makes use of the pedal positions to estimate the engine's operating point. This explains why fluctuations in the accelerator pedal show up as variations in the alternator power setpoint during the vehicle measurements. Although the switching profile of the alternator power is much richer in the vehicle tests, its average behavior is similar to the simulation model. This follows from the SOC curves which remain close to each other.

7.1.8 Evaluation & Discussion

The results in Tables 7.2 and 7.3 provide, among other things, insight in the improvement in fuel economy. All strategies achieve an improvement between 1.1 % and 2.6 %, whereas SOE_f is close to SOE_0. The following three observations are contrary to the expectations and will be clarified in this section. First, the vehicle

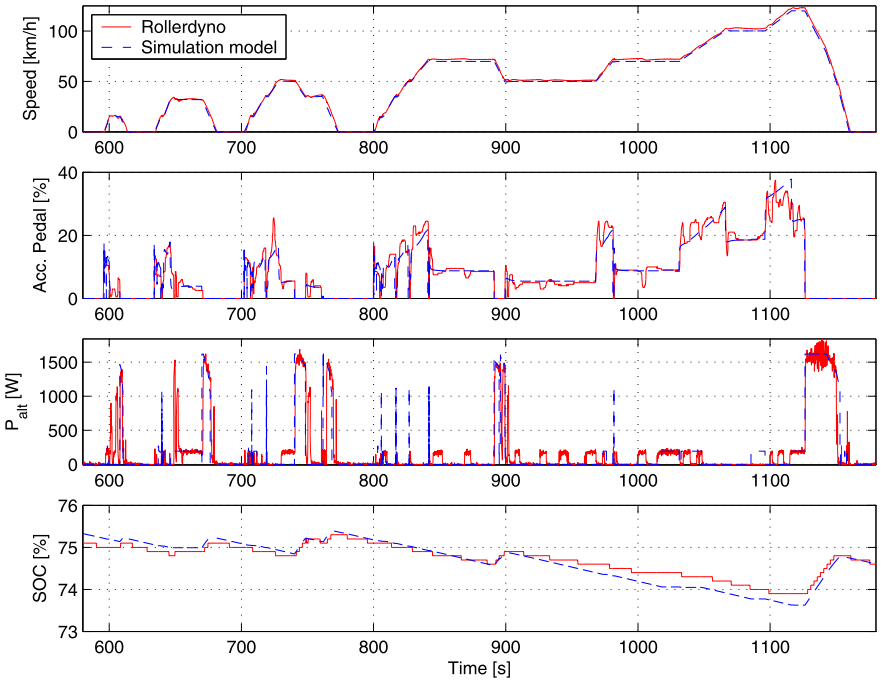

Fig. 7.5 Control actions with PSM strategy (hot-engine start) for the second half of the NEDC. Energy recovery is readily visible

experiments achieve a better performance than expected from simulations. In simulations, PSM and PDM achieve a fuel reduction of 1.5 % and 1.1 %, respectively. This is significantly lower than in the vehicle experiments where the profits for PSM vary between 2.6 % and 2.4 % (cold and hot engine) and PDM achieves a fuel reduction of 1.4 %. Second, the simulation results reveal that the off-line and online strategies achieve equal performance, although no predictions are used for the online strategy. Finally, the last observation is that the profits with PDM are lower than with PSM, whereas higher profits are logically expected.

Differences Between Simulations and Experiments It turns out that the simulation environment suffers from three dominant model inaccuracies: (a) the PI-controlled driver model has a limited complexity, compared to a human driver; (b) the alternator status-signal is not present in the simulation environment and (c) the engine speed is not compensated for alternator power changes. As will be shown next, these elements prevent the simulation environment from achieving results similar to the vehicle experiments.

1. The PI-controlled driver model follows the desired speed profile perfectly and the accelerator pedal changes smoothly, see Fig. 7.5. Because the accelerator pedal is related to the engine operating point by means of the ECM, less variation is also

Table 7.4 Model uncertainties and influence on fuel economy

Model property	Fuel eco %
PI-controlled driver	0.1
Alternator feedforward signal	0.5–1.0
Reduced engine speed	0.3

recognized in the operation point of the engine. These variations are a necessity for energy management and hence, the simulation model offers less opportunities for the EMS. For validation, different parameter values are assigned to the driver model to emulate the overshoot from a human driver. Depending on the tuning-parameters of the PI-controlled driver, the cumulative fuel consumption changes around $\approx$0.1 %. Although this effect is relatively small, it confirms that there is a correlation.

2. As discussed in Sect. 7.1.6, the feedforward signal from the alternator to the ECM is not present in the simulation environment. Only the vehicle tests with the baseline strategy use this signal. Additional simulations have been done with a baseline strategy that includes a tentative feedforward signal. Depending on the bandwidth of the PI-controlled driver, additional fuel consumption is seen. An accurate driver with a high bandwidth experiences only minor influence from the feedforward signal and the fuel consumption of the baseline strategy increases around 0.5 %. On the other hand, a driver with a low bandwidth is not able to counteract the feedforward signal at undesired moments (e.g., during vehicle deceleration). Here, the baseline strategy requires additional fuel up to 1.0 %. In general, one can draw the conclusion that ignoring the alternator feedforward signal during deceleration phases is not only profitable for the EMS, but also for the baseline strategy as well.
3. Another side effect of increasing the alternator power when there is no feedforward signal present, is that the vehicle decelerates. This can be compensated by the human driver, but especially during braking phases, this extra braking force is often preferred. The vehicle experiments point out that a vehicle with the EMS travels at a lower engine speed during the deceleration phases. Although the differences are rather small, the average engine speed over the entire drive cycle reduces approximately 6 [rpm]. Simulations with this reduced engine speed indicate an extra fuel economy benefit of 0.3 %.

An overview of the model uncertainties that limit the profits in fuel economy of the simulation results is shown in Table 7.4. The cumulative uncertainty is of similar size as the improvement in fuel economy shown by PSM or PDM in the simulation environment. Adding the model uncertainties to the simulation results is sufficient to close the gap with the roller–dynamometer experiments. Nevertheless, this large uncertainty indicates that the model for the driver and the ECM have limited validity. Due to accuracy limitations of the roller–dynamometer, more accurate measurement data are not available.

Similar Performance with Off-line and Online Strategies Theoretically, the MPC strategy achieves a better fuel economy than the online strategy because it relies on exact prediction information from the future drive cycle, whereas the online strategy does not use this a priori knowledge. In practical situations, however, the computational power is limited and the off-line strategy uses a discrete sampling period of $\Delta T = 1$ [s]. On the other hand, the online strategy has a low computational demand and its sampling interval has been selected equal to $\Delta T = 0.01$ [s]. In this way, the online strategy is able to anticipate quick events and achieves a performance close to the MPC strategy. Note that the extra fuel benefits will be small in the simulation environment due to the moderate driver behavior. However, during vehicle experiments, this higher sampling frequency becomes relevant because of more intensive driver behavior.

Lower Profits with PDM than with PSM Conceptually, PDM offers more freedom for energy management than PSM, because PDM controls two design variables (the alternator power and the electric load demand) whereas PSM is restricted to only one variable (the alternator power). Therefore, it is expected that PDM achieves better fuel economy. However, the increased electric load demand that has been selected for PDM dominates the results of the experiments. Due to the extra load of 250 W, the alternator reaches its power limitations more often, leading to less freedom for the PDM strategy. Furthermore, the baseline strategy also recovers a fraction of the free kinetic energy during vehicle deceleration and this fraction becomes larger when the electric load increases. This observation is extensively discussed in Koot et al. (2006) and points out that the advantage of PDM with respect to the baseline becomes less visible if the electric load increases.

Discussion Although the online strategies do not enforce a fixed energy level E_s^f for the battery at the end of the drive cycle, they are able to finish the NEDC drive cycle close to E_s^f, by means of the PI-controller. From other simulations it is known that the differences between SOE_0 and SOE_f as indicated in Table 7.3 have less than 0.1 % effect on the fuel economy. As a result, no correction methods are used when calculating the absolute benefit in fuel economy.

So far, no attention has been paid to the vehicle experiments with a cold engine start. Before testing the EMS, vehicles experiments are done with the baseline strategy and a cold engine start. According to the measured relation between fuel use and engine coolant temperature, the assumption was made that temperature only influences the fuel offset $\gamma_{p,0}$, rather than the slope $\gamma_{p,1}$ of the fuel curves. However, $\gamma_{p,0}$ does not appear in the quadratic cost criterion. Hence, the EMS requires no modifications for a cold engine start and the PSM and PDM algorithms do not take the temperature of the ICE into account.

Remarkably, the results from Table 7.3 show that driving the NEDC with a cold engine start offers more potential for energy management than starting this trip with a hot engine. This means that the influence of the ICE temperature is not well understood.

7.1.9 Conclusions

Energy management strategies are developed for the electric powernet in a conventional vehicle. As a benchmark, an off-line strategy has been defined that solves a QP optimization problem in an MPC framework. In addition, a causal online strategy has been developed that does not rely on prediction information. Additional freedom for EMS is obtained by introducing electric loads with a flexible power demand. Furthermore, all strategies have the opportunity to include extra losses in the battery model. This allows the designer to make a trade-off between battery wear and fuel economy.

To obtain performance that is close to the optimal solution, the off-line MPC strategy requires a prediction horizon of more than 100 [s] for a typical drive cycle. On the other hand, the online causal strategy achieves a similar performance without using any prediction information. This strategy is directly suitable for implementation in a vehicle.

The causal EMS has been implemented in the vehicle. A roller–dynamometer test-bench has been used to validate the control actions of the strategy. The tail-pipe emissions are measured to obtain insight into the achieved profits in fuel economy. From the vehicle experiments it can be concluded that the EMS has a positive effect on the vehicle's fuel economy up to 2.6 %. This result is better than expected from simulations. In particular the behavior of the human driver as well as the communication between the alternator and the ECM are not well modeled in the simulation environment and explain the deficiencies seen in fuel economy.

7.2 Optimal Control of a Hybrid Electric Truck

This section[2] presents a case study that demonstrates the real-time implementable powersplit strategy based on optimal control with experimental results obtained with a hybrid electric truck on a chassis dynamometer. First, the experimental set-up is introduced. Second, tuning rules for the feedback algorithm (6.4), for estimation of the costate variable, are presented. Third, the performance of the optimal control-based powersplit with (i) a constant state-of-energy setpoint, and with (ii) an adaptive state-of-energy setpoint is evaluated, using a non-hybrid baseline and a heuristic powersplit algorithm as references.

7.2.1 Experimental Set-up

The experiments are carried out on the Eindhoven University of Technology heavy-duty chassis dynamometer, with a parallel hybrid electric truck. A schematic

[2]This section re-uses material from Van Keulen et al. (2012).

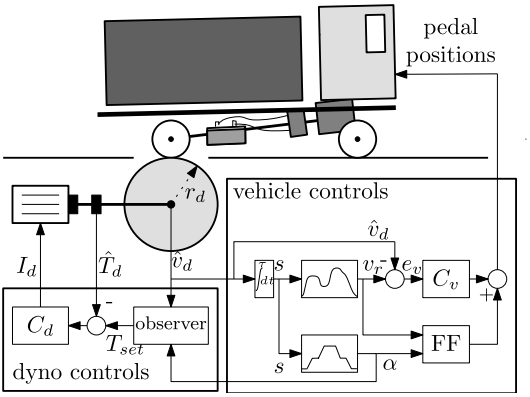

Fig. 7.6 Schematic overview of the test set-up with a hybrid truck on the dynamometer

overview of the set-up is depicted in Fig. 7.6. Advantage of such a set-up, compared to measurements on the road, is the good reproducibility of the road load forces, the forces a vehicle normally experiences on the road. The influence of the driver, traffic, and weather conditions is excluded. The road load forces can be described with the following function:

$$F_w = m_e \frac{\mathrm{d}v}{\mathrm{d}t} + mg_a \sin\alpha + c_0 mg_a \cos\alpha + c_1 v + c_2 v^2, \tag{7.41}$$

where m_e is the effective vehicle inertia, including rotating parts of the vehicle, m the vehicle mass, α the road slope, c_0 the coefficient for rolling resistance, c_1 the resistance proportional to the vehicle velocity v and c_2 the aerodynamic coefficient.

In the dynamo test set-up, the wheels of the driven axle are placed on drums. The driver is replaced by the *vehicle controls* where the covered distance s is calculated by integration of the measured velocity $\hat{v}_d$ of the drums. Predefined distance-velocity and distance-elevation trajectories, stored in the control system, provide the velocity error signal and send it to the velocity controller C_v, which essentially is a PID controller with anti-windup. A feedforward controller FF is added to reduce the tracking error. Output of the velocity controller is an accelerator and brake pedal position. The accelerator pedal input is an analog signal replacing the potentiometer of the pedal. Since the braking system is not controlled *by-wire*, the brake pedal is actuated mechanically with an electric piston, see Fig. 7.7.

The drums are connected to a 220 [kW] electric machine which simulates the road load forces F_w of the truck. The *dyno controls* observer generates a torque setpoint:

$$T_{\text{set}} = F_w(\alpha, v) r_d + T_c, \tag{7.42}$$

using the measured velocity of the drums $\hat{v}_d$, estimating $\frac{\mathrm{d}\hat{v}_d}{\mathrm{d}t}$ with a nonlinear (Luenberger) observer, and using the road grade α provided by the corresponding distance-elevation profile. Here, r_d is the drum radius, and T_c compensates for the

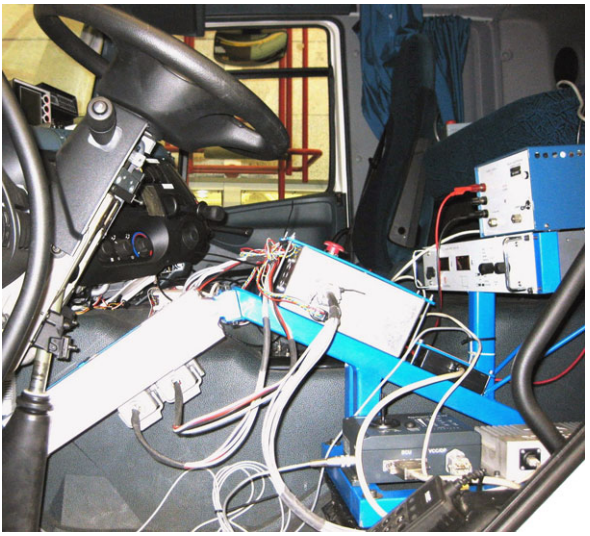

Fig. 7.7 Brake pedal actuator replacing the driver seat

drum dynamics. A feedback algorithm C_d, using the measured torque $\hat{T}_d$, controls the dynamo electric machine output power with control signal I_d.

The engine cooling water is cooled with an external heat exchanger. The air temperature, pressure and humidity of the test set-up room is not controlled. All measurements where carried out in summer, where the ambient temperature was between 20 and 30 [°C]. Before every measurement sequence, a warm-up procedure was carried out while between two velocity trajectories the set-up was cooled. The temperature of engine cooling water, hybrid system cooling water, final drive oil, and gearbox oil was hereby used as an indicator.

Several signals are measured. A torque flange measures T_d, the circumferential velocity of the drums, v_d, is measured with an encoder. The fuel consumption is measured using a dedicated fuel flow meter. The battery voltage, U_{oc}, electric machine input current, I_s, and rotational velocity of electric machine and engine, ω_m and ω_p, are obtained using the standard vehicle sensors via the CAN bus interface, as well as the signals $\hat{p}$, T_r, SOE, SOE_r and T_{m_r}. Note that ω_m and ω_p are different in case the clutch is opened.

7.2.2 Implemented Controls

An overview of the optimal control-based powersplit control is shown in Fig. 7.8. The gas pedal position ϑ determines the torque (power) request T_r. The brake pedal operates the service brakes only. Implementation of brake blending, between service brakes and electric machine, could enhance comfort, however, this is considered to be outside the scope of this book. The percentage gas pedal position is scaled, between rotational velocity dependent bounds to obtain $\underline{T}_m(\omega_m)$ for $\vartheta = 0$ and

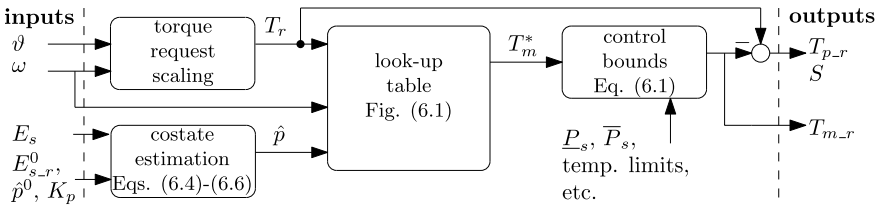

Fig. 7.8 Overview of implemented powersplit controls

$\overline{T}_p(\omega_m)$ for $\vartheta = 100\ \%$. So, the maximum power output is equal to the maximum power output of the engine and electric boost is not implemented.

The optimal electric machine torque T_m^* results from the look-up table, see Fig. 6.1. Control T_m^* is corrected afterwards to protect the battery from over- or undercharging with

$$T_{m\_r} = \min\left(\max\left[T_m^*, \frac{1}{\omega_m} P_m(\underline{P}_s)\right], \frac{1}{\omega_m} P_m(\overline{P}_s)\right), \tag{7.43}$$

where T_{m_r} is the resulting electric machine torque request which is communicated to the lower level controller operating on the same ECU, $P_m(P_s)$ the functional inverse of (2.3) and Fig. 2.7, and the control bounds are given by

$$\underline{P}_s = \frac{\underline{U}_R(E_s)}{R} U_{\mathrm{oc}}, \tag{7.44}$$

and

$$\overline{P}_s = \frac{\overline{U}_R(E_s)}{R} U_{\mathrm{oc}}, \tag{7.45}$$

in which $\underline{U}_R$ is the state-of-energy dependent allowable charge over-potential which becomes zero at $\overline{E}_s$, $\overline{U}_R$ the state-of-energy dependent allowable discharge over-potential which becomes zero at $\underline{E}_s$. So, the electric machine power is gradually reduced if a state-of-energy bound is reached. For simplicity temperature related bounds are not discussed here. The torque request to the engine becomes

$$T_{p\_r} = T_r - T_{m\_r}, \tag{7.46}$$

where T_{p_r} is the resulting torque request for the engine which is communicated via the CAN bus to another ECU governing the engine power. If $T_{p\_r} = 0$ the clutch command $S = 0$ is communicated to the engine ECU, otherwise $S = 1$.

7.2.3 Tuning of the Costate Variable Estimation

In this section, the implemented optimal control-based powersplit control is evaluated with experiments. To generalize the results of the tuning of the costate, it is

convenient to use the state-of-energy as the actually stored energy normalized for the total storage capacity, recall from Chap. 2:

$$\mathrm{SOE} = \frac{E_s}{E_c}, \tag{7.47}$$

where E_c is the assumed battery energy capacity. The battery limitations $\underline{\mathrm{SOE}} > 0$ and $\overline{\mathrm{SOE}} < 1$ are used.

The implemented strategy estimates the costate p with proportional feedback on the state-of-energy as in (6.4). This results in tuning parameters $\hat{p}^0$, K_p, and SOE_r^0, which were added to the vehicle CAN bus such that they are real-time adjustable. The implemented strategy is evaluated with a constant state-of-energy reference $\mathrm{SOE}_r^0 = 0.5$, as well as an adaptive $\mathrm{SOE}_r(t)$ using (6.5). The resulting powersplit control strategy has two tuning parameters, see (6.4):

- proportional feedback gain K_p,
- initial costate guess $\hat{p}^0$.

The evaluation of K_p and $\hat{p}^0$ is performed on the basis of dynamometer tests with the medium-duty truck. The Urban Dynamometer Driving Schedule (UDDS), see also Fig. 2.19, is used as reference velocity trajectory for the velocity controller.

The main aim of the evaluation is to compare the relative fuel consumption of different powersplit control strategies and tuning parameters, therefore, reproducibility of the measurements is of primary interest, while the exact tracking of the velocity setpoint is of secondary importance. The dynamo mechanical energy consumption trajectory $E_d(t) = \int \frac{\hat{T}_d \hat{v}_d}{r_d} \mathrm{d}\tau$ is used to indicate the reproducibility of the velocity tracking and road load simulation.

The feedback gain K_p is varied between 1 and 3 while initial guess $\hat{p}^0$ is varied between 2.5 and 3.0. The experimental results for the UDDS velocity trajectory are depicted in Fig. 7.9. The measurements are repeated three times for each setting. In the top row of Fig. 7.9, it can be seen that the reproducibility of the velocity and dynamometer control is good. The standard deviation of $E_d(t_f)$, for the 18 different control settings, is 0.017 [MJ], which is a standard deviation of 0.1 %. To evaluate the reproducibility of fuel consumption, six measurements with one control setting were carried out. The standard deviation in fuel consumption was less than 1.0 %.

The resulting state-of-energy trajectories are depicted on the second row of Fig. 7.9. All measurements are started with an initial battery SOE_0 of approximately 0.5. An estimation of the *state-of-charge* is provided by the battery management system. The exact algorithm for state-of-charge estimation is unknown, but relies mainly on Coulomb counting. The open-circuit voltage of Fig. 2.10 is used to compute the state-of-energy.

As expected the battery is depleted for costate values, $\hat{p}^0$, that are estimated too small, and charged for multiplier values that are estimated too large. For a small feedback gain, $K_p = 1$, the state-of-energy bounds are reached for $\hat{p}^0 = 2.5$, and $\hat{p}^0 = 3.0$. The bandwidth of the (linear) feedback is a trade-off between avoiding under- or overcharging and minimizing the control actions on short term state-of-energy fluctuations. It can be seen for $K_p = 2$ that the feedback allows enough

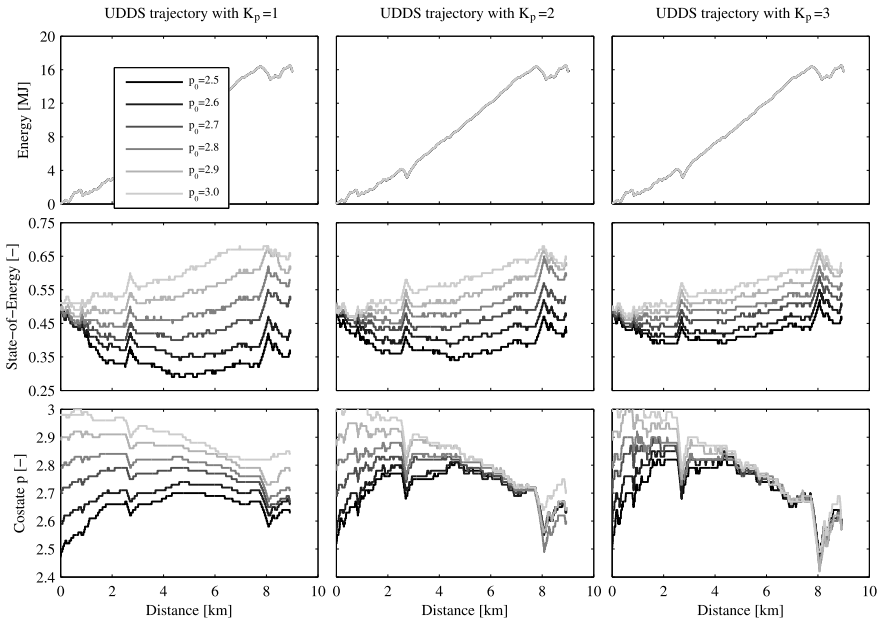

Fig. 7.9 Influence of tuning variables $\hat{p}^0$ and K_p on the UDDS velocity trajectory. The figure displays nine *subfigures*, where the first row depicts the energy consumption trajectories $E_d(t)$, the *second row* depicts the state-of-energy trajectories SOE(t), and the *third row* depicts the estimated costate trajectories $\hat{p}$. The *three columns* indicate the three different settings of K_p. Each *subfigure* shows the results of six different settings of $\hat{p}^0$

"freedom" for fluctuations without reaching the battery bounds for a large range of $\hat{p}^0$.

The bottom row of Fig. 7.9 depicts the estimated costate. With sufficient feedback, the estimated costate variable converges to the same trajectory. A steady-state difference in state-of-energy is a consequence. An integral term can remove this steady-state error, however, this also leads to unnecessary control actions in case the state-of-energy bounds are not reached anyway.

The measurements for each setting on the UDDS cycle were repeated three times, the avarage value of the fuel consumption is depicted in Fig. 7.10. The figure indicates the percentage increase in equivalent fuel consumption, the fuel consumption corrected for state-of-energy deviations, as a function of tuning parameters $\hat{p}^0$ and K_p. The lowest fuel consumption is used as reference fuel consumption.

A minimum fuel consumption is found with $\hat{p}^0 = 2.8$ and $K_p = 1$. At low feedback gain the fuel consumption increases with several percents for increasing or decreasing $\hat{p}^0$. For larger feedback gains this increase in fuel consumption is smaller and remains within 1.5 % of the minimum.

Open loop measurements ($K_p = 0$) where also performed, providing a near charge-sustaining trajectory with $\hat{p}^0 = 2.75$. According to the PMP this provides the global optimal solution (assuming that the non-convexity, associated with the clutch

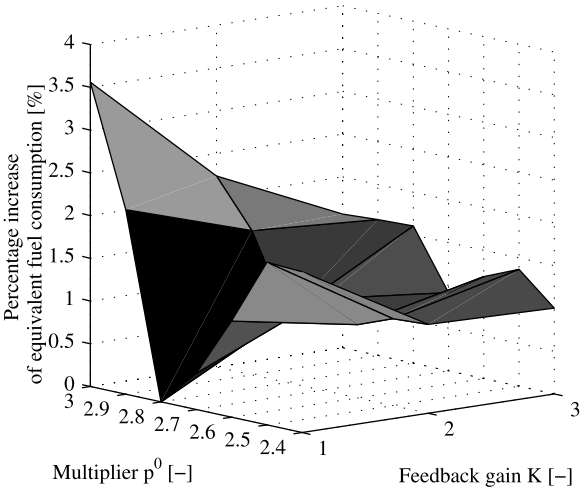

Fig. 7.10 Percentage increase of equivalent fuel consumption corrected for state-of-energy deviation, as a function of tuning parameters K_p and $\hat{p}^0$

opening, does not alter optimality and battery state-of-energy dependent losses can be ignored). The value $\hat{p}^0 = 2.75$ is also used for the calculation of the equivalence factor for fuel consumption correction

$$E_{eq}(t) = E_f(t) + \hat{p}^0\big(E_s(t) - E_s(t_0)\big). \tag{7.48}$$

The avarage fuel consumption of three repeated open loop measurements with $\hat{p}^0 = 2.75$ is 0.65 % higher than the minimum in Fig. 7.10. This difference is not significant relative to the measurement accuracy.

Based upon the experimental results it is concluded that:

- tuning parameter $\hat{p}^0$ is relatively easy to tune, although $\hat{p}^0$ depends on the characteristics of the components, since the influence of different settings on the fuel consumption is small as long as $K_p > 1$,
- the parameter setting $K_p = 2$ and $\hat{p}^0 = 2.7$ provides good performance (the settings are chosen after evaluating also the FTP-75 velocity trajectory depicted in Fig. 2.21 and, therefore, differ from the optimum found in Fig. 7.10),
- fuel consumption results within 1.5 % of the global optimum can be expected on routes where the state-of-energy bounds are not reached. The optimum is established with open loop charge sustaining measurements using a constant multiplier which, according to optimal control theory, leads to the global optimum.

7.2.4 Strategy Comparison

In Sect. 7.2.3, it is shown that fuel consumption results close to optimal can be achieved for power request trajectories at which the state-of-energy bounds are not reached. A bigger challenge, for the real-time powersplit control, is to obtain good

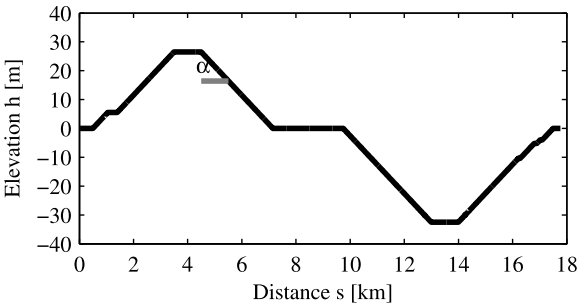

Fig. 7.11 Elevation-distance trajectory h for $\alpha = 0.01$ [rad]. There a two descents seperated by a short distance and there is no net elevation change over the route

performance on routes where the state-of-energy bounds are reached. In general, this happens on routes with considerable elevation differences, where the recoverable potential energy is large compared to the capacity of the storage device. Four different powersplit control strategies are evaluated:

- the optimal control algorithm, with the settings $K_p = 2$, $\hat{p}^0 = 2.7$, using $\text{SOE}_r = 0.5$,
- the optimal control algorithm, with the settings $K_p = 2$, $\hat{p}^0 = 2.7$, using an adaptive SOE_r, using (6.5), with $K_E = K_h = 0.2$, and $\text{SOE}_r^0 = 0.5$,
- a heuristic algorithm, tuned by the manufacturer of the hybrid system hardware,
- a non-hybrid baseline strategy, using the same test vehicle in engine-only mode.

To evaluate the performance of the three powersplit algorithms in situations where the state-of-energy bounds are reached, a road grade trajectory, see Fig. 7.11, complements the FTP-75 velocity trajectory depicted in Fig. 2.21. The road grade is scaled so α varies between 0 and 0.05 [rad], in steps of 0.005 [rad]. This leads to 11 different velocity–power trajectories which where used to evaluate the four strategies.

The results are depicted in Fig. 7.12, where three columns display three of the 11 evaluated road grades. The cumulative energy produced by the dynamometer E_d is used to indicate a fair comparison between the strategies. Notice that E_d of the baseline strategy, on all trajectories, is lower than the other strategies. This is caused by an increase in gearshift time since in the hybrid strategies the electric machine is also used to alter the rotational velocity of the gearbox primary spindle during shifting improving drivability. The increased gearshift time decreased the average velocity and, thus, the magnitude of the simulated road load losses. Also the other strategies have some deviations, therefore, the fuel consumption results are corrected for deviations of $E_d(t)$ for each α with the average $\bar{E}_d(t)$ of the three hybrid strategies.

At routes with $\alpha \leq 0.02$ [rad] recovery of the potential energy is not possible unless the vehicle is braking. At routes with $\alpha \geq 0.025$ [rad], recovery of the potential energy becomes significant. Note also that the cumulative energy delivered by the dynamometer decreases for routes with increasing grades. During the uphill trajectories the maximum power of the engine is reached, such that the average velocity of the cycle is reduced, and the road load decreases due to lower aerodynamic losses.

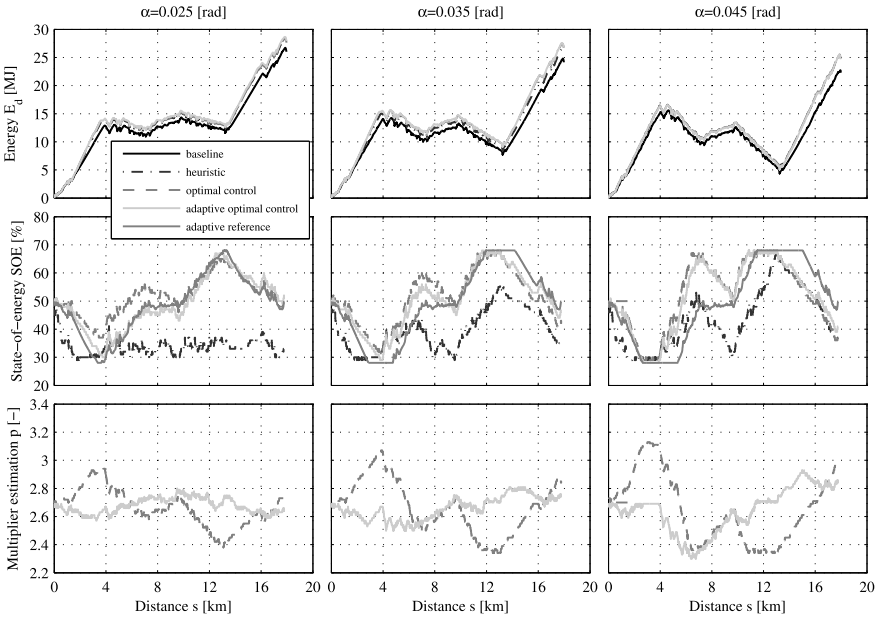

Fig. 7.12 Test results on the FTP-75 velocity trajectory with elevations. The *first row* depicts the cumulative energy produced by the dynamometer E_d. The *second row* depicts the state-of-energy trajectories of the three hybrid strategies and the reference trajectory of the adaptive strategy. The optimal control is depicted in *gray*, and the adaptive optimal control in *light gray*. The *third row* shows the estimated costate variable

The heuristic strategy is to deplete the battery right from the start of the trajectory. For routes with mild grades, the state-of-energy remains on the lower boundary of the battery. This is suboptimal as shown by the fuel consumption results discussed below. However, on routes with a large recovery potential, the heuristic strategy is performing well. Since the time between the two descents is relatively small, immediate depletion is successful here.

In routes with low recovery potential the optimal control strategies are both charge sustaining. In routes with high recovery potential ($\alpha > 0.035$ [rad]) the upper bound of the storage device is reached by the optimal control with constant setpoint. The optimal control with adaptive reference is more successful in discharging the battery in between the two descents. Note that an integration term in the feedback algorithm for the multiplier estimation (6.4) would be undesirable here, since this limits freedom in deviation from SOE_r even further.

Recall from Sect. 5.3.1 that the optimal costate trajectory, in situations where the state-of-energy boundaries are not reached, and neglecting the state-of-energy dependent battery losses, is described with a constant. The costate estimation, based upon the reference state-of-energy adaptive for kinetic and potential energy, shows a smaller variation, than the constant state-of-energy reference, indicating that the costate estimation is improved.

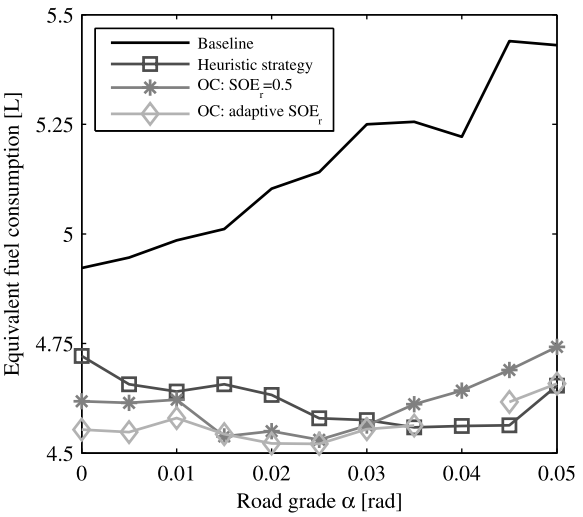

Fig. 7.13 Fuel consumption results of various strategies on the FTP-75 velocity trajectory with elevations. Unfortunately, the results of the adaptive strategy at $\alpha = 0.04$ [rad] were corrupted and are omitted

The fuel consumption results, as a function of road grades α, of the four strategies, are depicted in Fig. 7.13. The fuel consumption of the baseline vehicle, corrected for the smaller dynamo energy input for each α, is increasing for routes with larger grades. The optimal control strategies achieve a better fuel consumption, up to 4 %, than the heuristic controller on trajectories where recoverable energy is smaller than the battery capacity. In fact, the fuel consumption of the optimal control with adaptive reference is lower than the heuristic strategy at all trajectories, except at $\alpha = 0.045$ [rad].

From the evaluation of four strategies the following can be concluded:

- the optimal control with adaptive state-of-energy reference leads to a good estimation of the multiplier function, is superior to the other strategies, and is a useful extension on the optimal control algorithm using feedback on the state-of-energy with a constant reference,
- the measured fuel consumption reduction potential of hybridizing a medium-duty truck on the FTP velocity trajectory, with a vehicle mass of 9 ton and component size and characteristics as presented in Table 2.1, ranged from 7 % on velocity and power trajectories with low recovery potential (shallow slopes) up to 16 % on velocity and power trajectories with high recovery potential (steep slopes),
- the adaptive optimal control strategy achieves a fuel consumption which is up to 3 % lower, with respect to the baseline vehicle, than the heuristic controller.

7.2.5 Conclusions

In this case study, the implementation and evaluation of optimal powersplit control in hybrid vehicles is discussed.

A real-time strategy is implemented in a hybrid truck using proportional feedback on the state-of-energy to estimate the optimal costate function. The optimal value of the Hamiltonian is derived off-line and stored in a look-up table for a range of operating points and costate values. The storage capacity and computational power, of standard Electronic Control Units, form no obstacle for the implementation of optimal control-based powersplit strategies.

The proposed strategy is evaluated with chassis dynamo measurements on 12 different velocity and grade trajectories. The results indicate that linear feedback on the state-of-energy is a useful strategy for multiplier estimation and is easy to tune. Fuel consumption results within 1.5 % of the global optimum can be expected in velocity and grade trajectories where the capacity bounds of the battery are not reached.

The performance can be enhanced, by using a state-of-energy reference trajectory, adaptive for kinetic and potential energy of the vehicle, which still requires only information of the actual vehicle status. Compared to the non-hybrid baseline strategy, the optimal powersplit obtained fuel consumption reductions between 7 % and 16 %. The optimal controller achieved a fuel consumption up to 3 % lower than the heuristic controller tuned by the manufacturer.

A powersplit control design for hybrid electric vehicles, based on optimal control and requiring only information available in the vehicle, is easy to tune, can be implemented on standard hardware, and offers a fuel consumption very close to the optimal one for a wide variety of operating conditions. Therefore, predictive information, for example coming from a navigation system, can offer only marginal fuel consumption benefits in charge sustaining hybrid vehicles.

References

Allen RW, Rosenthal TJ, Hogue JR (1996) Modeling and simulation of driver/vehicle interaction. In: SAE internat. congress & exposition, Detroit, MI, USA. SAE paper 960177

Åsbogård M, Edström F, Bringhed J, Larsson M, Hellgren J (2004) Evaluating potential of vehicle auxiliary system coordination using optimal control. In: Proc internat symp advanced veh control, Arnhem, The Netherlands

Back M, Simons M, Kirschaum F, Krebs V (2002) Predictive control of drivetrains. In: Proc 15th IFAC World Congress, Barcelona, Spain

Van den Bosch PPJ, Lootsma FA (1987) Scheduling of power generation via large-scale nonlinear optimization. J Optim Theory Appl 55:313–326

Buller S, Thele M, Karden E, de Doncker RW (2003) Impedance-based non-linear dynamic battery modeling for automotive applications. J Power Sources 113(2):422–430

Camacho EF, Bordons C (2004) Model predictive control, 2nd edn. Springer, London

De Jager B (2003) Predictive storage control for a class of power conversion systems. In: Proc European control conf, Cambridge, UK, pp 1–6

De Jager B (2004) The horizon in predictive energy storage control. In: Proc American control conf, Boston, MA, USA, pp 186–187

Kessels J, Koot M, Hendrix W, Ellenbroek R, Heemels M, Pesgens M, Steinbuch M, Van den Bosch P (2004) Vehicle modeling for energy management strategies. In: Proc internat symp advanced veh control, Arnhem, The Netherlands

Kessels JTBA, Koot M, De Jager B, Van den Bosch PPJ (2005) Energy management for vehicle power net with flexible electric load demand. In: Proc IEEE conf control appl. IEEE, Toronto, pp 1504–1509

Kessels JTBA, Koot M, De Jager B, Van den Bosch PPJ, Aneke NEPI, Kok DB (2007) Energy management for the electrical powernet in vehicles with a conventional drivetrain. IEEE Trans Control Syst Technol 15(3):494–505

Van Keulen T, De Jager B, Kessels JTBA, Steinbuch M (2012) Design, implementation, and evaluation of optimal power split control in hybrid vehicles. Control Eng Pract 20:547–558

Koot M, Kessels JTBA, De Jager B, Heemels WPMH, Van den Bosch PPJ, Steinbuch M (2005) Energy management strategies for vehicular electric power systems. IEEE Trans Veh Technol 54(3):771–782

Koot M, Kessels J, De Jager B, Van den Bosch P (2006) Fuel reduction potential of energy management for vehicular electric power systems. Int J Alternative Prop 1(1):112–131

Tate ED, Boyd SP (2000) Finding ultimate limits of performance for hybrid electric vehicles. In: Hybrid electric vehicles (SP-1560), Costa Mesa, CA, SAE paper 2000-01-3099

West MJ, Bingham CM, Schofield N (2003) Predictive control for energy management in all/more electric vehicles with multiple energy storage units. In: Proc IEEE internat electric machines and drives conf, vol 1. IEEE, New York, pp 222–228

Wipke KB, Cuddy MR, Burch SD (1999) ADVISOR 2.1: a user-friendly advanced powertrain simulation using a combined backward/forward approach. IEEE Trans Veh Technol 48(6):1751–1761

Index

B. de Jager et al., *Optimal Control of Hybrid Vehicles*, Advances in Industrial Control,
DOI 10.1007/978-1-4471-5076-3, © Springer-Verlag London 2013